
Unraveling surface enabled phenomena in low-dimensional molecular systems

Inauguraldissertation

zur

Erlangung der Würde eines Doktors der Philosophie

vorgelegt der

Philosophisch-Naturwissenschaftlichen Fakultät

der Universität Basel

von

Milos Baljozovic

aus Leskovac (Serbien)

Zürich, 2018

Original document stored on the publication server of the University of Basel <http://edoc.unibas.ch/>



This work is licensed under a Creative Commons Attribution-NonCommercial-ShareAlike 4.0 International License. The complete text may be viewed here: <http://creativecommons.org/licenses/by-nc-sa/4.0/>

Genehmigt von der Philosophisch-Naturwissenschaftlichen Fakultät

auf Antrag von:

Prof. Dr. Thomas Jung

Prof. Dr. Ernst Meyer

Basel, 19.09.2017

Prof. Dr. Martin Spiess

Dekan

THE HISTORY OF SCIENCE SHOWS THAT THEORIES ARE PERISHABLE. WITH EVERY NEW TRUTH THAT IS REVEALED WE GET A BETTER UNDERSTANDING OF NATURE AND OUR CONCEPTIONS AND VIEWS ARE MODIFIED.

NIKOLA TESLA

ABSTRACT

This thesis focuses on the investigation of on-surface molecular architectures which exhibit extraordinary magnetic and quantum properties originating from the reduced dimensionality at surfaces. Many different combinations of spin-bearing square planar molecules and substrates were used and probed by local techniques as well as by spatial averaging techniques. Probing low-dimensional molecular magnetism by combination of several complementary techniques provides a more complete insight into the subtle interplay of the interactions involved at the surfaces.

The comprehensive study of magnetism of Cr-phthalocyanine molecules supported on several different ferromagnetic and non-magnetic substrates demonstrated how the spin state of such molecules depends on the interaction with the substrate. Also in my work I have shown that the relative orientation of the molecule's and the substrate's easy magnetization axes is of great importance, even for molecules which are paramagnetic in the bulk. This is further supported by the example of interactions of Cr-based adsorbates with the Au(111) substrate where, for example, a very strong anisotropy of the Cr magnetic moment is observed. At the same time, the exchange coupling interactions with bare ferromagnetic substrates, Co and Ni are different in both the intensity and sign. These observations indicate that a refinement of the current models describing interface magnetism is needed to understand the peculiar magnetic coupling in these systems. Study of various phthalocyanine molecules on Pb(111) demonstrate the importance of employment of X-ray based techniques to complement the local probe investigations of these spin systems coupled to a superconductor. Although such experiments can drive a system out of the superconductive phase by the presence of a magnetic field, it was shown that some magnetic properties of these molecules won't depend greatly on whether the system is or is not in the superconducting state. This fact is making X-ray based investigations even more important.

The emergence of interesting magnetic phenomena through intra- and inter-molecular interactions was addressed next. Pilot experiments performed on triply-fused bisporphyrin molecules opened up the field for a new class of molecules containing two spin centers that can be exchanged providing a plethora of possibilities for tuning the molecule's magnetic properties. Following up on our recent observation of long range 2D ferrimagnetic ordering in heteromolecular checkerboard assemblies of Fe and Mn phthalocyanine molecules supported on Au(111), we performed the experiments with similar binary 2D systems to further glimpse into the role of 3d orbitals, their symmetries and filling in maintaining long range ordering. It was shown that depending on the configuration and filling of their 3d orbitals the metallo-phthalocyanine molecules will interact by the RKKY interaction or not. In addition, I reported on a significant asymmetry in the mixing of hetero molecular layers that is occurring due to the pinning of one of the molecular types to the surface. Surprisingly this process modifies the layer structure of multilayers and therefore needs to be taken into account for on-surface metalation reactions or for the design of spintronic devices.

Further on, different ways of modification of magnetic properties have been investigated. We reported on how spin states of various phthalocyanine molecules can be altered upon exposure to molecular and atomic hydrogen. In the former case, this process is completely reversible, while in the latter case it leads to irreversible changes of both the spin state of the metal center and of the molecule. Also, the ability to induce a Co surface functionalization with both N and Cl adlayers is demonstrated. Here, X-ray Photoelectron Diffraction has been employed to precisely determine interatomic distances in the created functionalized surfaces.

In the last part the importance of development of new preparation/characterization techniques is demonstrated. It is shown how we successfully implemented the technique of deposition of large non-sublimable molecules into the UHV directly from solution, and how we have adapted a detector that is commonly used in time-of-flight mass spectrometry for acquiring fast, time-resolved XAS signal at SIM beamline of the SLS.

In short, this thesis represents a collection of several pieces of a larger scientific puzzle grazing through several aspects of molecular magnetism.

TABLE OF CONTENTS

Abstract	iv
List of abbreviations.....	i
Introduction.....	1
1.1 MOTIVATION AND OUTLINE	1
1.2 MAGNETISM IN A NUTSHELL	4
1.3 MAGNETIC INTERACTIONS AT THE NANOSCALE	5
1.4 MOLECULAR MAGNETISM.....	7
Methods and experimental techniques.....	11
2.1 ULTRA-HIGH VACUUM	11
2.2 SYNCHROTRON RADIATION	13
2.3 PHOTOEMISSION TECHNIQUES/SPECTROSCOPY	14
2.4 ABSORPTION TECHNIQUES	17
2.5 LOW ENERGY ELECTRON DIFFRACTION.....	21
2.6 SCANNING TUNNELING MICROSCOPY/SPECTROSCOPY.....	22
2.7 SAMPLE PREPARATION	24
Results	26
3.1 NOVEL SPIN ARCHITECTURES	26
3.1.1 ASSEMBLIES AND MAGNETIC PROPERTIES OF CHROMIUM(II)-PHthalOCYANINE MOLECULES	26
3.1.2 INTERACTIONS OF VARIOUS PHthalOCYANINE MOLECULES WITH Pb(111) SUPPORT	43
3.2 INTRA- AND INTER-MOLECULAR INTERACTIONS.....	52
3.2.1 MAGNETIC PROPERTIES OF HOMO- AND HETERO-METALLIC TRIPLY-FUSED PORPHYRINS	52
3.2.2 SELF-ASSEMBLY AND MAGNETIC ORDER OF 2D SPIN LATTICES ON SURFACES	61
3.2.3 VERTICAL REORGANIZATION OF MOLECULAR BI- AND MULTI-LAYERS DUE TO MOLECULE-SUBSTRATE INTERACTIONS	66
3.3 TUNING OF THE MAGNETIC INTERACTIONS.....	71
3.3.1 SPIN MANIPULATIONS OF METAL-CONTAINING PHthalOCYANINE MOLECULES BY H₂/H* LIGATION	71
3.3.2 SURFACE MODIFICATION OF CO FERROMAGNETIC FILMS FOR TUNING EXCHANGE INTERACTIONS OF ADSORBED MOLECULES.....	85
3.4 NOVEL EXPERIMENTAL SETUPS.....	98
3.4.1 EXPERIMENTAL SETUP FOR TIME-RESOLVED XAS AT SIM BEAMLINE OF SLS.....	98
3.4.2 PULSE-VALVE MOLECULAR DEPOSITION FROM SOLUTIONS.....	102
Conclusions and prospects	106
Bibliography.....	111
Acknowledgments	120
List of publications	122
Curriculum Vitae	123

LIST OF ABBREVIATIONS

General acronyms

2D	2-Dimensional
3D	3-Dimensional
BE	Binding Energy
B_J	Brillouin function
Cl/Co	c(2x2)-Cl superstructure on Co(001)
E_{ex}	Magnetic exchange energy
K	Magnetic anisotropy energy
k_B	Boltzmann constant
L	Langmuir, unit of exposure to a surface in UHV; 1L is equal to exposure of 10^{-6} torr for 1 second
M	Magnetization
m	Magnetic moment
MAE	Magnetic anisotropy energy
μ_B	Bohr Magnetron; the spin magnetic moment of an electron is approximately equal to $1 \mu_B$
MCP	Multichannel plate
MOF	Metal-Organic Framework
N/Co	c(2x2)-N superstructure on Co(001)
O/Co	c(2x2)-O superstructure on Co(001)
O/Ni	c(2x2)-O superstructure on Ni(001)
PEY	Partial Electron Yield

QCMB	Quartz Crystal Micro-Balance
T	Temperature or Tesla (unit of B)
TEY	Total Electron Yield
UHV	Ultra-High Vacuum

Methods

ARPES	Angle Resolved Photoelectron Spectroscopy
DFT	Density Functional Theory
EDAC	Electron Diffraction in Atomic Clusters
LD	Linear Dichroism
LEED	Low-Energy Electron Diffraction
PMSCO	PEARL multiple-scattering cluster calculations and structural optimization
STM	Scanning Tunneling Microscopy
STS	Scanning Tunneling Spectroscopy
UPS	Ultraviolet Photoelectron Spectroscopy
UV-VIS	Ultraviolet-Visible Spectroscopy
XAS	X-ray Absorption Spectroscopy
XMCD	X-ray Magnetic Circular Dichroism
XPS	X-ray Photoelectron Spectroscopy
XPD	X-ray Photoelectron Diffraction

Chemical compounds

DCM	dichloromethane
-----	-----------------

DE	diethyl-ether
H2TPP	5,10,15,20-tetraphenyl-porphyrin
H ₂ Pc	29H,31H-Phthalocyanine
H ₂	molecular hydrogen
H*	atomic hydrogen
M	Metal
Mn(OAc) ₂	Manganese(II)-acetate
MOEPCI	M-2,3,7,8,12,13,17,18-octaethyl-porphyrin chloride
MTPPCI	M-5,10,15,20-tetraphenyl-porphyrin chloride
MTTBPPCI	M-tetrakis(3,5-di-tert-butylphenyl)-porphyrin chloride
MTBE	Methyl tert-butyl ether
MPc	M-phthalocyanine
MFPC	M-1,2,3,4,8,9,10,11,15,16,17,18,22,23,24,25-hexadecafluoro-Pc
tbut-tf-MMCl ₂ -P	triply fused (β-β, meso-meso, β'-β')-MM-tetrakis(3,5-di-tert-butylphenyl)-bisporphyrin chloride
tf-M ₁ M ₂ Br ₂ -P	triply fused (β-β, meso-meso, β'-β')-M ₁ M ₂ -bisporphyrin bromide
TM	Transition Metal

Chapter 1

INTRODUCTION

1.1 MOTIVATION AND OUTLINE

For scientists, it is always difficult to answer the question what the ramification of their work is as it takes a lot of courage and vision to seek for possible use of what at that moment seems so far in the future. When Hertz finally managed to demonstrate existence of electro-magnetic waves in order to prove his mentor Maxwell was correct in joining theories of magnetism, electricity and optics into what will become foundation of modern theory of electro-magnetism, they asked him what the ramification of his work is. He simply answered, “Nothing, I guess”^{1,2}. I would dare to say he was wrong.

In today’s world, EM waves are part of our everyday life that it is difficult to even start naming all the consequences of his discovery. From the moment we switch on the TV, send a message or picture from some remote place, or when we charge our phones and other electronic devices, when we look at the interactions of EM radiation with matter, in medicine, when we take a flight to our favorite holiday resort, warm-up our food in a microwave, check when is the next train/bus departing from the station, pay our bills, communicate at the speed of light, we all rely on the EM waves. We can easily say that

today's world is world of EM waves. But all of it comes at a certain price – we consume a lot of energy and need more powerful and efficient computers to process all these requests, we produce terabytes of data that need to be stored somewhere, but we are also getting more and more vulnerable to threats in the virtual world. So far science and technology were keeping the pace; reducing the sizes of devices on computer chip for processing, or bits in memory devices for storing the information was giving success. Every 2 years, these numbers were doubled, as represented by the Moore's law, bringing us to the point where we are today. In the current world of knowledge, however, this "law" (better say trend) is reaching its limit³. Reducing size is bringing us to the utmost limit of matter before the quantization effects take place.

Rather than scaling down device sizes, several groups took the so-called bottom-up approach, where the idea is to learn and engineer novel devices from the smaller fragments, for example single atoms or molecules. This goes along with visionary of future devices based on quantum technology, as it gives the opportunity to learn about basic interactions on the level of single atoms and molecules. Detailed understanding of the interactions in such low-dimensional world is a prerequisite for use of these devices in envisaged quantum computers that are often considered the holy grail of modern computing.

In that light, this thesis focuses on unraveling the interactions in low-dimensional surface supported molecular systems, with a focus on magnetism. It looks into substrate-molecule interactions and how they lead to specific properties of the spins present in the molecules. It represents a humble contribution to the field of molecular magnetism with perspectives of data storage and quantum computing.

In what turned out to be emerging field of spintronics, different groups were putting their efforts on different spin active systems, but also on different methods for their investigations. Some were focused on local probing techniques and probing of individual entities, while other rather worked with ensembles of them probing their magnetic properties by space averaging techniques. However, they all had something very important in common - pursuit for novel systems that inevitably helped to get better understanding of the nano and spin world. In view of that pursuit, **Section 3.1** of this thesis focuses on several

novel spin systems that will be introduced and their magnetic properties discussed in light of the interplay of the interactions with underlying substrates.

The more we learn about interactions of molecules with substrates, we realize that not all of their properties are governed by the interactions with the substrate but also can be of other origin. In some cases, they are of intrinsic origin, for example magnetism of SMMs and SIMs or strong anisotropies that are reported for some classes of molecules. In the other cases, contrasting to the intrinsic ones, these can be of collective origin and consequence of the interactions of big numbers of molecules. **Section 3.2** focuses on few cases where these intra- and inter-molecular interactions were manifested through some interesting magnetic phenomena.

The next level of understanding the principles of low-dimensional magnetism is reached once we start mastering and tuning properties of such systems. This is usually achieved either by addressing aforementioned intrinsic properties, or by addressing interactions with surface supports and among themselves. Therefore, a few examples of how we could predictably tune magnetic properties of molecular systems will be addressed in the **Section 3.3**.

Last, the creation of novel systems to be investigated is often preceded with the invention of novel preparation techniques. And in the opposite, new systems often require novel characterization techniques and models for being able to fully embrace their novelty. In the last **Section 3.4** of this thesis, new techniques for sample preparation but also characterizations will be introduced for the sake of expansion of our possibilities to investigate low-dimensional systems.

1.2 MAGNETISM IN A NUTSHELL

Magnetism is one of the topics that is not so easy to explain and has been tackling scientist's minds for a long time. The first mentioning of this phenomenon dates back to 6th century BC when Thales of Miletus described how iron is attracted to "lodestone". Since then, it has been covered by many authors spanning from scientists and philosophers but also medicasters who believed in its "magical" properties. In the early times, although not much was known about it, due to its practical properties it has been used in navigation and medicine. With the development of science and technology, understanding of magnetic phenomena was also evolving leading to even broader use due to the ability to engineer materials at the atomic scale. This was, however, followed by discoveries of novel phenomena that were not fitting into the current frameworks and led to further developments of both theoretical and experimental treatments.

Today, term magnetism covers very broad field of science where behavior of various materials or their magnetic moments to be more precise, is investigated upon exposure to the magnetic field. Depending on the response to the exposure, materials are divided into three main groups: diamagnetic, paramagnetic and magnetically ordered materials. We need to thank Oersted, Ampere, Biot, Savart, Faraday and Gauss on performing extensive studies and connecting electricity and magnetism. Later on, Maxwell went even further in conjuncting electricity, magnetism and optics into what is known to be unified theory of electromagnetism described with 4 simple equations. Introduction of quantization by Einstein gave rise to new field where Pauli, Dirac, Heisenberg, Hund and Schrödinger started explaining magnetic properties with electron spin, its quantum numbers and quantum mechanics. This was crowned by Richard Feynman, Julian Schwinger and Sin-itero Tomonaga creating the self-consistent framework of Quantum Electrodynamics, a very powerful tool used to explain interactions of light and matter in modern science. Although today we know and can explain way more about magnetism than just a century ago, this doesn't mean the game is over – on the contrary, the spinning spiral is every day getting a new momentum.

1.3 MAGNETIC INTERACTIONS AT THE NANOSCALE

In the urge of getting smaller and faster in today's technology world, reducing size of the materials to the nanoscale is bringing us to the utmost limit of looking at single or finite numbers of atoms, where the quantization effects are taking place. Here, several ways of magnetic moments interacting with each other are to be considered⁴:

First among them to mention is the dipole-dipole interaction of the two magnetic moments separated in space. If the magnetic moments are represented as dipoles, having origin and end of the magnetic field at the two poles, they can be approximated as vectors interacting with each other. The strength of such interaction is proportional to the magnitudes of the interacting moments but inversely proportion to the cubic of their distance, making it very weak. Nevertheless, this concept of interpretation of magnetic interactions and moments is well spread due to simplicity in representing moments originating from current loops, or the intrinsic magnetic moments related to "spinning" or "orbiting" electrons. The spin (s or S^1) and orbital (l or L) angular momentums can then interact and give rise to spin-orbit interaction/coupling (SOI or SOC) and form total angular momentum (j or J). This effect is very important and gives rise to magnetocrystalline anisotropy, splitting of certain sublevels in atoms or Rashba splitting of the surface states that are all very important for the stability of the magnetic moments, especially when supported on surfaces.

Way stronger interactions are the exchange interactions of the magnetic moments. As the name suggests, there must be exchange of the indistinguishable particles, in particular electrons with their spins involved. When individual atoms are brought together, there is an overlap between atomic orbitals (AO) that due to Pauli Exclusion Principle leads to antisymmetric overall wave function when two electrons are exchanged. This interaction can

¹ small letters represent individual spin, orbital and total angular momentums, while the capitals are sums of all individual ones. In case of lighter atoms, the spin-orbit interaction is weaker than spin or orbital interactions, so we can look at the sums of spins and orbital moments interacting; on the contrary, in case of heavier ones, we need to look at interactions of individual moments and then sum them up.

lead to parallel or antiparallel orientation of involved spins depending on the relative signs and magnitudes of the involved Coulomb, overlap and exchange integrals that are used to describe it. It is usually occurring at short distances, at the orbitals of the same atom, or the two neighboring atoms (direct exchange) but also via intermediary atoms (indirect or superexchange) or on the longer distances via delocalized surface electrons (Ruderman–Kittel–Kasuya–Yosida, RKKY or Dzyaloshinskii-Moriya, DM interactions). Another interaction highly related to the interactions with delocalized electrons is the Kondo effect, that on the contrary to RKKY and DM interactions that are promoting ordering of magnetic moments tends to screen them. Exchange interactions are mostly discussed in the framework of Heitler-London or valence bond (VB) theory of chemical bonding where electrons are considered localized at certain orbitals and explained by Heisenberg model/Hamiltonian.

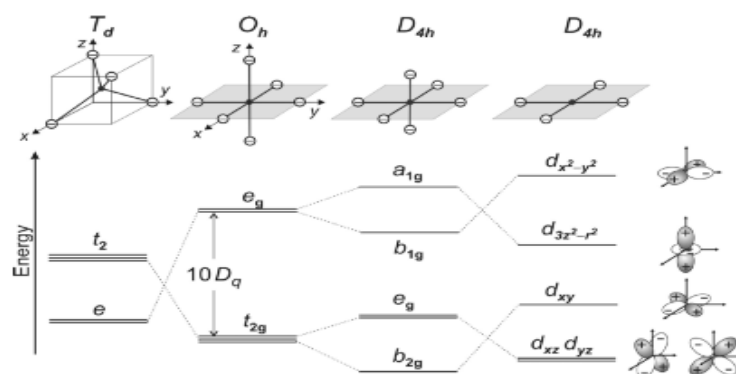


Figure 1.1. *d-orbitals splitting under the influence of point charges distributed in tetrahedral, octahedral, tetragonally distorted and square planar manner around the atom⁴*

The exchange interactions, combined with the spin-orbit coupling were used by Hund to spell out the famous empirical Hund's rules of the energy level ordering and filling with electrons for a given number of electrons/electronic

configuration. At this moment, we have to also introduce a model of crystal/ligand field² splitting that would highly influence the energy level ordering, especially when talking about 3d metals that are of interest in this thesis. Namely, if the isotropic atom is put in a non-symmetric electric field, either by deposition on surface or with incorporation in molecule/complex, its orbitals will not experience homogeneous electric fields and this

² in crystal field theory (CFT), electric field is approximated by point charges on main axes of the coordinate system, and it treats orbitals as atomic orbitals rather than molecular one, neglecting the possible charge reorganizations. Although ligand field theory (LFT) expands this and includes possibilities of charge transfers, the approach of CFT is readily used to explain many physical effects due to its simplicity

would lead to their reorganization in energy. Figure 1.1. demonstrates splitting of the d-orbitals under the influence of octahedral, tetragonally distorted and square-planar ligand fields that will be of interest for this thesis.

Lastly, if an atom with unpaired electrons and thus magnetic moment is placed in the magnetic field, additional interaction named Zeeman interaction appears. Although it puzzled scientists at the time it was discovered, mostly due to absence of knowledge of both electron and spin existence, nowadays it is one of the most straightforward to use by applying Lande's formula and formalism. The consequences of this interaction are manifold. First to mention would definitively be the lifting of degeneracy of the electronic states that lead to its discovery. Next, in certain temperature ranges, this interaction is responsible for the stabilization of magnetic moments and our ability to magnetize materials, effect that is vastly exploited in current memory devices and in investigations of novel magnetic materials.

1.4 MOLECULAR MAGNETISM

Although way larger in size than just single atoms, molecules are taking a special place in investigations of low-dimensional magnetism. Since magnetic and chemical properties are highly related in that both are originating from valence electrons, this opens up vast field of possibilities for influencing magnetic properties of spins enclosed in molecules by chemical modifications. In addition, when supported on surfaces, they tend to arrange in specific and sometimes tunable ways, bringing additional level of freedom that can be manipulated with.

Part of the investigations in the field of molecular magnetism focused on probing Single molecular magnets (SMMs). The active spin center(s) here were investigated by protecting/embedding them in an organic medium to reduce interaction with the environment and thus increase their relaxation times upon magnetization. First such studies focused on bulk investigations of polymetallic complexes where moments were stabilized by exchange interactions⁵⁻⁷. Later on, they were investigated on surfaces as well⁸⁻¹¹. The investigations of their relaxation times on surfaces provide very important characteristics of

the systems as they are providing insight into the effects and importance of molecule–substrate interactions but also photon flux on the SMMs magnetic properties necessary for their application in, e.g. molecule-inorganic hybrid devices^{9,12}. Difficulties and limitations in preparing single and/or ordered layered samples of such robust molecules spurred the use of Single Ion Magnets (SIMs), a subgroup of SMMs containing only one metal center. Several examples of lanthanide based SIMs deposited on surfaces again demonstrated the role of substrate interactions in obtaining longer relaxation times and sizable anisotropies^{13–15}.

Others, on the other hand focused on investigations of paramagnetic molecules whose moments could be stabilized either by supporting them on ferromagnetic substrates or in high magnetic fields (at low enough temperatures, of course). Shortly after the capability of the XMCD technique to probe magnetic properties of single atoms adsorbed on surfaces had been demonstrated¹⁶, it was used to show that the magnetic moments of paramagnetic molecules such as MnTPP(Cl) can be stabilized at the room temperature and beyond when adsorbed on ferromagnetic Co substrates due to ferromagnetic exchange coupling to the underlying substrate¹⁷. The importance of STM experiments was here also highlighted as they served as a proof for the stability of the molecules during their deposition by thermal sublimation process. Soon after, other metallo-porphyrin and -phthalocyanine molecules containing 3d metal centers such as Fe and Co showed similar behavior and were ferromagnetically coupled to the FM substrate. Different coupling mechanisms, in particular direct and indirect exchange coupling were used to describe such behavior^{18–21}. Interestingly, molecular metal center moments followed the substrate magnetization direction and could be aligned either in plane or out of plane¹⁹. Introduction of a spacer O layer between molecules and the underlying ferromagnetic substrates weakened their interactions and allowed molecules to self-assemble in large molecular islands; this was a consequence of different interaction pathways - the superexchange interaction via the oxygen atoms that also lead to antiferromagnetic ordering of their moments^{22,23}. A similar effect was observed in the case of graphene used as a spacer layer between molecules and the substrate²⁴. Further investigations on coupling of chromium-tetraphenylporphyrine(chloride) (CrTPP(Cl))²⁵ and vanadyl-phthalocyanine (VOPc)²⁶ showed

that their specific electronic configurations, in particular filling of the d-shell would lead to antiferromagnetic coupling to bare ferromagnetic substrates. The investigations then shifted to probing such spin-bearing molecules upon their adsorption on non-magnetic substrates by STM/S and XMCD. The investigations on Au(111) and Au(110) substrates demonstrated that strong interaction with the substrate can cause partial (in case of FePc molecules) or complete (in case of CoPc molecules) quenching of molecular magnetic moments^{27,28}. In the case of FePc molecules the phenomenon was attributed to the Kondo effect^{28,29} evidenced by STM/S experiments that provided insight into this interaction. In the case of CoPc molecules the quenching was attributed to a valence fluctuation due to a charge transfer from the substrate and was causing complete disappearance of both XMCD and Kondo signatures^{27,30,31}. Further investigations indicated the role of conduction electrons and the surface states for the presence of the Kondo effect and its characteristic imprint on this system^{30,32–35}. At this point, it became clear that magnetic interactions and properties of species on surfaces depend on several parameters – the distance to and the electronic structure of the spin-bearing centers, the pathway of interaction as well as the presence of mediators of interactions. This level of understanding allowed numerous ways of tuning magnetic properties and interactions of molecules on surfaces. This was achieved by use of external chemical stimuli^{21,36–44}, by molecular packing³⁵ or in the STM manipulation by creating artificial molecular structures by dehydrogenation of phthalocyanine molecules directly on the surface using the STM tip^{31,45}. It was soon showed that the formation of ordered layers of molecules⁴⁶ happens also on Pb(111) surfaces and are accompanied by signatures of the Kondo effect⁴⁷. Additionally, when deposited on EuO substrates extremely strong antiferromagnetic interactions were observed⁴⁸. By combining such molecular systems with superconducting Pb(111) and probing with a superconducting STM tip, it was shown that excited spin states of Fe-octaethylporphyrinchloride (FeOEPCI) molecules can be protected by a superconducting energy gap⁴⁹. In the case of MnPc molecules that due to their shape interact strongly with the substrate, this creates a magnetic scattering potential for the quasi-particles of the superconductor and gives rise to so-called Yu–Shiba–Rusinov (Shiba) states, especially interesting in light of Majorana physics⁵⁰. Another extraordinary

example of an unexpected low-dimensional magnetic structure was observed in XMCD and STS/M experiments where long range 2D-ferrimagnetic ordering had been observed and is attributed to the simultaneous presence of Kondo and RKKY type interactions mediated by the surface state electrons of the substrate in a supramolecular 2D Kondo lattice on Au(111)⁵¹. Although the simultaneous presence of Kondo and RKKY type interactions was suggested to be possible in an earlier STM study of FePc molecules supported on Au(111)⁵², only these XMCD experiments on engineered molecular structures provided an unambiguous proof of RKKY ordering. These latter examples do not only point out the advancement in mastering of complex on-surface architectures and the possibility to use such architectures in probing the low-dimensional magnetic systems and interactions therein but also the importance in multi-technique investigations for obtaining more elusive details in such systems.

Chapter 2

METHODS AND EXPERIMENTAL TECHNIQUES

2.1 ULTRA-HIGH VACUUM

In order to prepare and maintain well defined interfaces with molecules adsorbed, Ultra-High Vacuum (UHV) conditions are required. According to the kinetic theory of gases, the flux I [$m^{-2}s^{-1}$] of impinging molecules of gas towards the surface is given by the impinging equation:

$$I = \frac{p}{\sqrt{2\pi mk_B T}} \quad (1)$$

where p [Pa] is pressure in the chamber, m [kg] is mass of the molecules, $k_B = 1.38 \times 10^{-23} \text{ kgm}^2\text{s}^{-2}\text{K}^{-1}$ is the Boltzmann's constant and T [K] is temperature of the sample.

In the normal conditions ($p=10^5 \text{ Pa}$, $T=300 \text{ K}$, $m_{\text{air}}=4.83 \times 10^{-26} \text{ kg}$), that would mean that sample of 1cm^2 size (with 10^{15} adsorption sites) will be covered with air (assuming that every molecule that hits sample stays adsorbed) within a picosecond. If the pressure is in 10^{-6} mbar range³, sample will be covered within seconds, and if the pressure is in UHV conditions ($<10^{-10} \text{ mbar}$) it takes hours before sample is covered in the pessimistic scenario of all molecules

³ 1 mbar = 100 Pa. Although mbar is not a SI unit, it is well used in the field of surface science as a standard unit for pressure description

sticking to the surface. Therefore, in order to prolong the time samples can be stored and used, it is beneficial to keep it under UHV conditions. Beside the need of UHV conditions in order to reduce possible contaminations of the sample of interest, UHV conditions are also required for several analytical techniques, e.g. UPS/XPS, LEED, XAS where we want to minimize scattering of electrons or X-ray absorption on surrounding gas molecules. All the experiments that will be presented in this thesis were performed in UHV conditions that are reached by utilization of different pumps involving rough pumps, turbomolecular pumps, ion-getter pumps and titanium sublimation pumps according to the information from the following sources^{53,54}. Part of the experiments were performed at Surface Science Lab at PSI east, a multi-chamber UHV system (Figure 2.1a) while other part was performed at the beamlines of the Swiss Light Source (SLS) synchrotron located at the PSI west. The samples were transported between the Lab and beamlines without breaking the vacuum in the so-called vacuum suitcase (Figure 2.1b).

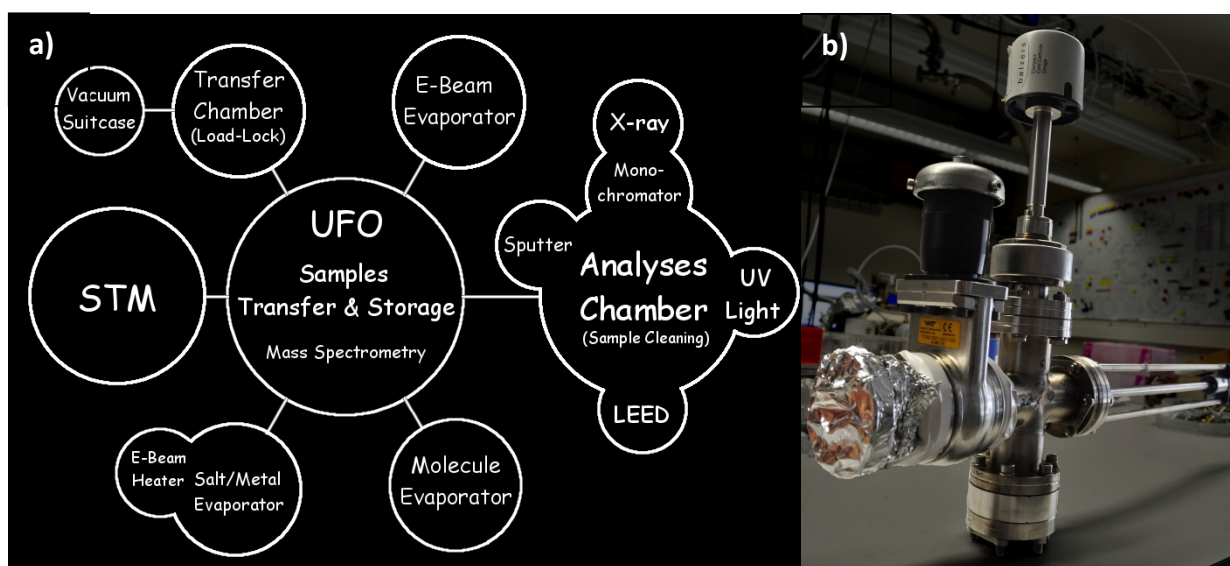


Figure 2.1. Schematic representation of the Surface Science Lab located at PSI east (a) and photo of the vacuum suitcase used for sample transport between the lab and beamlines at the SLS (b). Images from ⁵⁵

2.2 SYNCHROTRON RADIATION

Synchrotron radiation stands for the electromagnetic radiation that is emitted from relativistic charged particles that are forced to move along curved trajectories by applying magnetic field. Most commonly used are circular accelerators where electrons move at the speed close to the speed of light with energy in the range of GeV leading to the compression of the radiation pattern into narrow cone in the direction of motion resulting to the emission tangential to the particle orbit (Figure 2.2a). In the third generation synchrotron sources that SLS belongs to, timed laser pulses are used to create separated electron bunches that are at first accelerated in linear accelerator (LINAC) to energies of MeV and later on in a booster ring to energies of GeV before transfer to the storage rings (Figure 2.2b). Storage rings

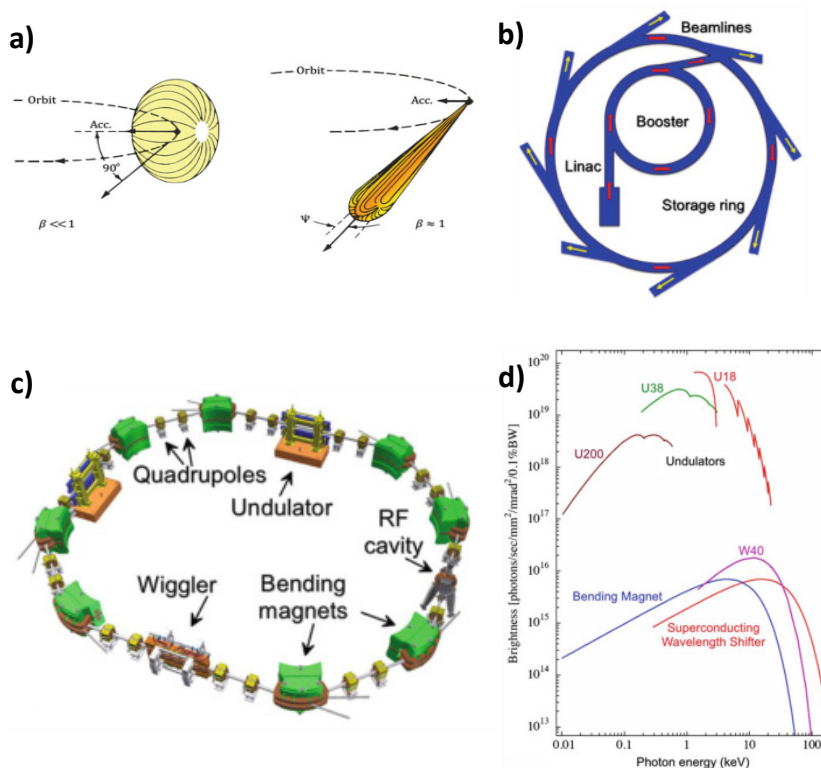


Figure 2.2. Angular distribution of the emitted light depending on the speed of electrons (a), layout of the synchrotron radiation facility (b), illustration of the storage ring and its components (c) and calculated brightness of radiation produced by three different undulators, bending magnet and a wiggler of the SLS (d). Images taken from ⁵⁶

consist of combination of bending magnets, wigglers and undulators where the radiation is produced, quadrupole magnets used for focusing/defocusing of the electron beam and Radio-Frequency (RF) cavity where electrons are compensated for the energy lost in the form of radiation (Figure 2.2c). Bending magnets, represented

by the simple dipole magnets, produce light that is of a very broad spectrum. Similar to them, wigglers, consisting of multiple fixed dipole magnets are producing comparable spectrum of the radiation, but with significant increase in intensity due to multiple deflection of the electron beam that is mostly traveling straight, except near the deflection points. Most powerful are for sure the undulators, also consisting of multiple dipole magnets in periodic arrangement, but deflecting beam sinusoidally thus allowing radiation cones to interfere constructively or destructively, leading to narrow bandwidth with significant increase in intensity (at the constructive interference peaks) (Figure 2.2d). Another big advantage of undulators is tunability of both energy (position) of interference maxima and the polarization of light (both linearly and circularly polarized light can be produced), which will come handy for investigations of magnetic properties in the parts to follow⁵⁶.

2.3 PHOTOEMISSION TECHNIQUES/SPECTROSCOPY

Discovery of photoelectric effect by Hertz and even more Einstein's explanation of it in the light of energy quantization gave birth to a scaffold of photoemission techniques that modern science rely on. Here, the sample is irradiated by light of certain wavelength/energy ($h\nu$), leading to photoemission of electrons that are put thorough hemispherical analyzer and differentiated by their kinetic energies E_k (Figure 2.3a). In this process, excited/charged atoms are created and the sample needs to be conductive to compensate for the lost electrons. Alternatively a low-energy electron gun is used for this purpose in case sample is insulating⁵⁴. If the core electrons were emitted, the excited state will be of way higher energy than the ground state and atoms can relax by emitting fluorescent X-ray photon, or less-desirable for photoelectron analysis, another electron through the Auger emission process. Thanks to the energy conservation principle, easy accessible kinetic energy of emitted electrons can be converted to structural information containing binding energy (E_b) by a simple relation:

$$h\nu = E_b + E_k + \Phi \quad (2)$$

where $h\nu$ [eV] is the excitation energy of the photons, E_b [eV] and E_k [eV] are binding and kinetic energies of the electrons, respectively and Φ [eV] is the workfunction of the spectrometer and relates to the energy required for electrons from highest occupied level to hop into vacuum.

As mentioned, the binding energy is very important for photoemission spectroscopies as it carries information about the investigated system. At the first glance, one can approximate it to a binding energy electrons have in initial states of emitting atoms, originating from the coulomb interactions with nucleus and other electrons. This energy will thus depend on the atomic number of element of interest and position of the electron-to-be-emitted on the defined atomic levels. As a consequence, it allows identification of different elements and defines ranges where the specific photoelectron lines will appear. Further on, upon emission of the electron, remaining electrons tend to rearrange and try to screen missing electron (so-called final state effect); this will highly depend on both properties of the emitting atom, but also on its environment in light of the electron density modifications due to bonding to other atoms. Both initial and final state effects of photoemission will induce specific chemical shifts of the detected photoelectron peaks allowing also investigation of chemical environment of the atoms of interest. Since only electrons emitted from the certain depth, usually a couple of nm only, will manage to escape from the sample, photoelectron spectroscopy is a highly surface sensitive technique suitable for investigations of interfaces. This sensitivity can be tuned by modification of kinetic energy of electrons (for an atom in certain chemical environment, E_b is constant so if the excitation energy is modified, by for example use of synchrotron light as an excitation source, kinetic energy is modified) as the mean free path of electrons is modified following so-called Universal curve (Figure 2.3b) or by modification of the path electron need to travel through sample before escaping it by simple sample rotation. The latter is sometimes also used for determining the thickness of certain materials by comparison of measurements at several different emission angles^{57–59}.

Depending on the energy of the photons used to induce photoemission, the photoemission techniques are usually divided into UV and X-ray techniques. In the first case, we are talking about Ultraviolet Photoelectron Spectroscopy (UPS), where mostly loosely

bound (valent) electrons are emitted and can give us information about electron distribution around Fermi level and their interaction with adsorbates^{60,61}. In addition, due to the conservation of angular momentum, the parallel momentum of these electrons is conserved upon photoemission, and is easily related to the emission angle in the Angle-Resolved Photoelectron Spectroscopy (ARPES) that is vastly used in mapping the band structure of materials⁶². If the X-rays are used, we are talking about X-ray Photoelectron Spectroscopy (XPS), where mostly core electrons are probed, carrying the information about chemical environment of the emitting atoms. This method represents, as its old name Electron Spectroscopy for Chemical Analysis (ESCA) suggests, very powerful tool for chemical analysis, both qualitatively and quantitatively⁴ when the relative intensities of the peaks are

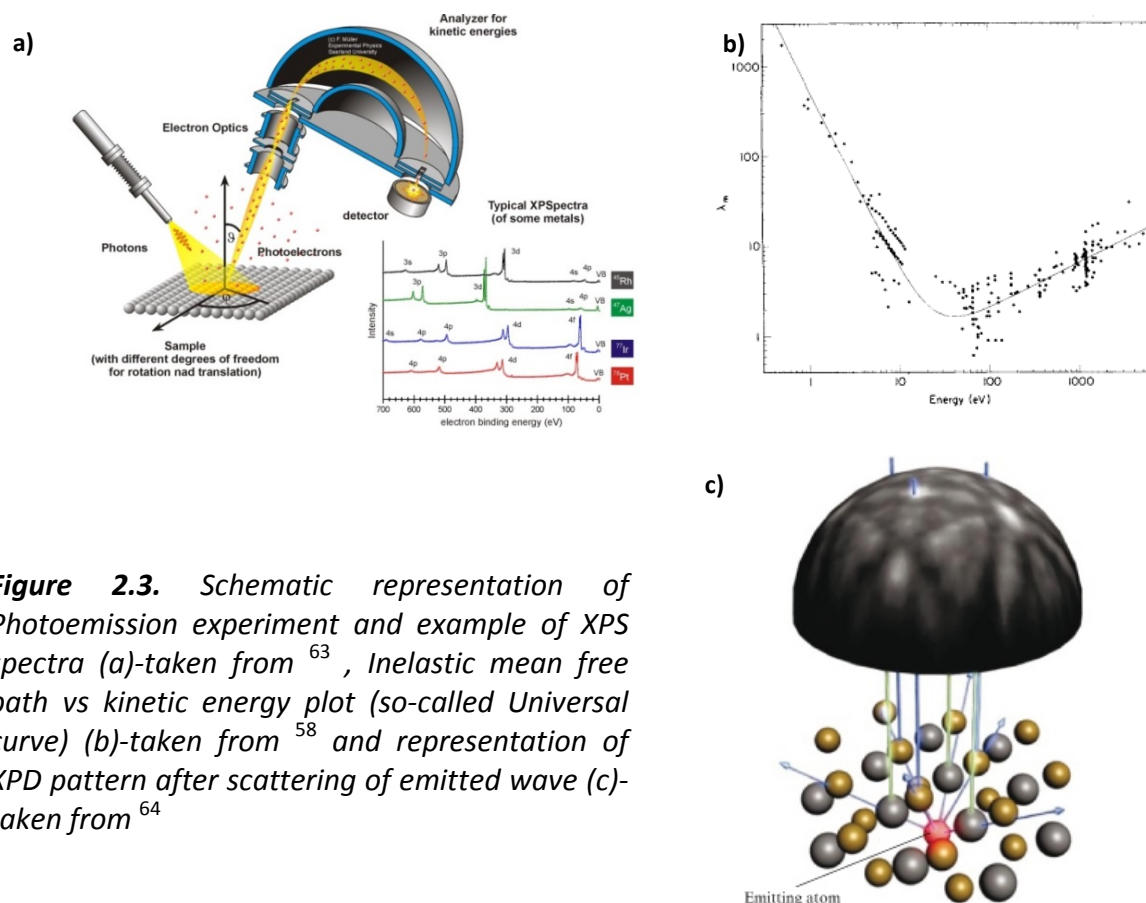


Figure 2.3. Schematic representation of Photoemission experiment and example of XPS spectra (a)-taken from ⁶³, Inelastic mean free path vs kinetic energy plot (so-called Universal curve) (b)-taken from ⁵⁸ and representation of XPD pattern after scattering of emitted wave (c)-taken from ⁶⁴

⁴ XPS is usually referred to as a semi-quantitative method due to difficulties in the data interpretation, but with the proper use of standards and certain sensitivity factors it can easily be considered a quantitative method

considered^{54,57}. If we look at the emitted electrons not as at the particles but rather as at the EM waves, these waves can scatter on surrounding atoms (Figure 2.3c) and produce certain diffraction pattern, especially if the kinetic energy of the emitted electrons is low. The analysis of such patterns is main focus of X-ray Photoelectron Diffraction (XPD) that is more and more used for direct determination of interatomic distances^{64–66}.

2.4 ABSORPTION TECHNIQUES

When light of initial intensity I_0 is transmitted through the material of the thickness d [m], according to the Lambert-Beer law, it is attenuated by:

$$I = I_0 e^{-\mu(E) d} \quad (3)$$

where $\mu(E)$ [m^{-1}] represent attenuation coefficient that includes both elastic and inelastic scattering and absorption contributions, but is in the range of interest (UV-Visible and soft X-ray regime) dominated by photoabsorption part. As it is implicitly mentioned, it is dependent

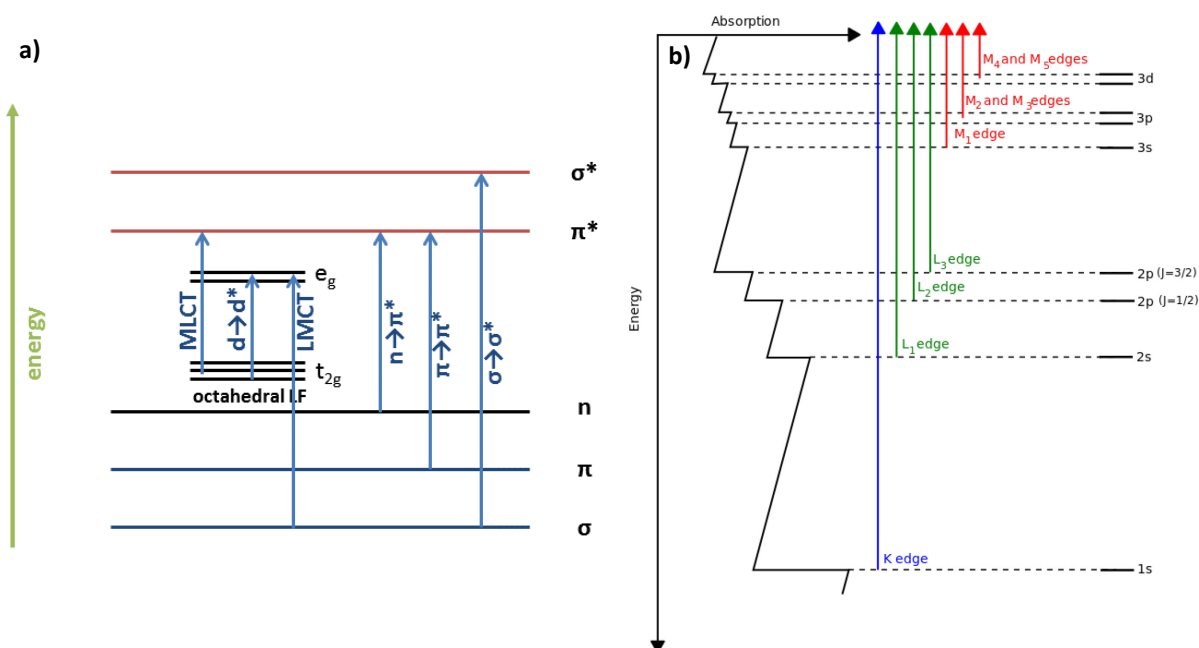


Figure 2.4. Schematic representations of possible electronic transitions in UV-VIS (a) and soft X-ray (b) photon energy range.

on the energy/wavelength of the transmitted light. If the energy is varied, at the certain values labeled as resonant ones, where the amount of energy matches energy difference between two energy levels it abruptly increases leading to the absorption⁵. In the UV and visible range, this energy matches $\pi \rightarrow \pi^*$, $n \rightarrow \pi^*$, $n \rightarrow \sigma^*$, $d \rightarrow d$ or even charge transfer (metal to ligand - MLCT or ligand to metal - LMCT) transitions (Figure 2.4a) taking place in molecular systems and in 3d-metal complexes. It is often referred to as UV-VIS spectrometry and is most commonly performed in transmission on solutions (but also on solid or gaseous probes). It is mostly used to identify different compounds and their concentrations, to monitor reactions or investigate their stability. The excited moiety can relax back to the ground state either by emitting photons (fluorescence and phosphorescence) or via a thermal relaxation process where the energy is transferred to the environment through vibrational relaxation.

In the X-ray regime, this energy is sufficient to promote core electrons above the Fermi level into empty bands/orbitals. Depending on the level/orbital these electrons originate from, in X-ray Absorption Spectroscopy (XAS) they are denoted as K – 1s, L₁ – 2s, L₂ – 2p_{1/2}, L₃ – 2p_{3/2}, M₁ – 3s etc. (Figure 2.4b). Both the initial state and excited state orbitals can further undergo splitting leading to fine structure of the XAS spectra. In addition, initial and final states can interact via multiplet effects, giving rise to multiplet structure of the XAS spectra⁶⁷. The excited atoms can relax back to the ground state by emitting photon (X-ray fluorescence) but it can also lead to emission of Auger and secondary electrons due to high energy. One way of detection of X-ray absorption can be via photon flux change in transmission if the sample is transparent enough for X-rays or in reflectance if it is not. Another option, more commonly used if interfaces are investigated is total (TEY) and partial (PEY) electron yield modes. In the TEY mode, all emitted electrons, regardless of being photo-, Auger or secondary electrons are indirectly detected by measuring current flowing to sample to compensate for their emergence. In the PEY mode, only a fraction of these electrons is detected, either in a selected energy or angular range. In both cases, since the

⁵ In modern theories of interaction of light and matter this is explained with the probabilities of the transition calculated using the famous Fermi golden rule

photoelectrons have to escape from the sample surface, it brings surface sensitivity to the XAS technique, which is of high importance for the study of interfaces or surface supported molecular architectures.

If linearly polarized X-rays are used in XAS, the relative orientation of the electric field vector and interacting orbitals play a big role in determining the intensity of transition/absorption. This effect is called “search light effect” (Figure 2.5a) and is readily used in the XAS variation named Near Edge X-ray Absorption Fine Structure (NEXAFS) spectroscopy, where looking at the intensity variation upon changes of angle between electric vector of the linearly polarized light and sample gives information about how atomic orbitals are oriented in space. This can give important information about adsorption geometries of molecules or atoms^{4,68}.

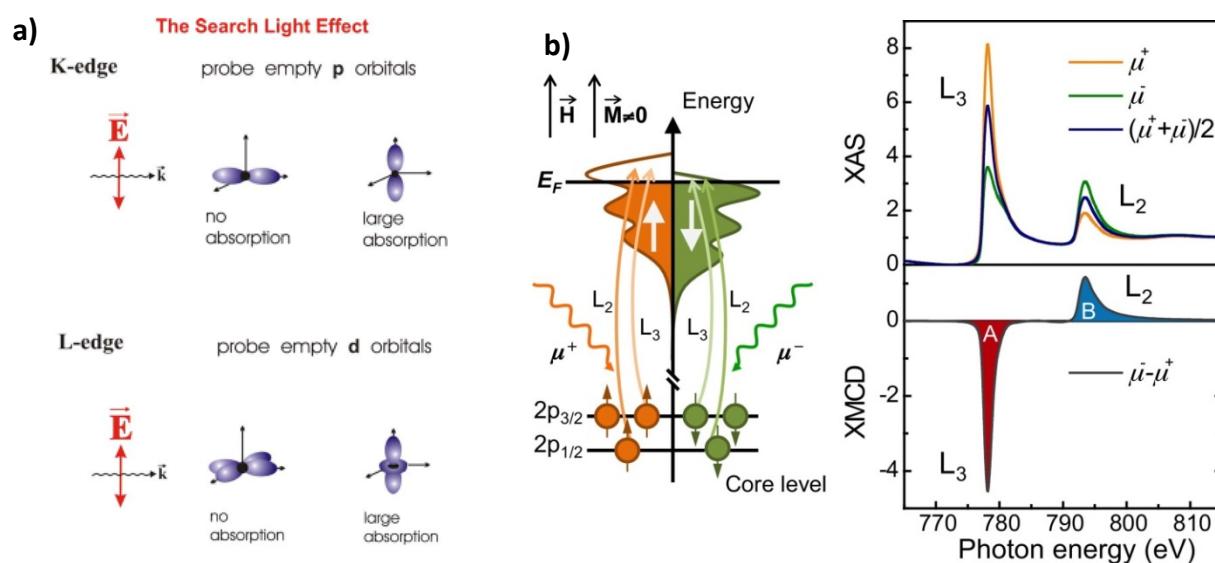


Figure 2.5. Demonstration of the search light effect of angle dependent linearly polarized X-ray absorption (a)⁶⁹ and demonstration of XMCD effect with an example spectra of Co (b)⁷⁰

Another variation of XAS is provided in case circularly polarized light is used; namely, circularly polarized photons possess angular momentum, $+\hbar$ (circ +) and $-\hbar$ (circ -) and will consequently interact differently with core electrons due to the additional dipole selection rule. This will, if spin polarization of the valence electrons exists affect the intensities of XAS spectra acquired with circ + and circ - polarized light, and the difference of two represents

X-ray Magnetic Circular Dichroism (XMCD) spectra (Figure 2.5b). Applying a mathematical calculus formulated in form of the XMCD Sum rules, we can extract both spin and orbital magnetic moments of the element of interest. Due to the geometrical constraints, the determined moments will represent effective magnetic moments that can, especially in case of spin moment, be different from the real one and theoretical calculations are required for their correction^{4,70,71}. This is especially important for Cr and Mn where the line overlap (L_2 and L_3) and multiplet effects are very large. In certain cases, it has been shown that XMCD can be used for the determination of exchange interaction strength or assessment of the anisotropy of the magnetic systems^{4,16,22,41,70,72}. This is achieved by varying the measurement temperature and/or magnetic field strength, and by looking into the interplay of exchange and Zeeman interactions and thermal relaxation processes. All of it makes XMCD spectroscopy a unique technique not only for obtaining element specific magnetic moments but also for probing magnetic exchange and anisotropy of the investigated magnetic system.

2.5 LOW ENERGY ELECTRON DIFFRACTION

Another complementary technique for surface characterization is represented by Low Energy Electron Diffraction (LEED). As the name suggests, low energy electrons are directed towards the sample and due to their dual nature they can scatter on surface atoms and create LEED pattern, a Fourier transformed image in reciprocal space. They can be described as waves of the wavelength:

$$\lambda = \frac{h}{\sqrt{2mE}} \quad (4)$$

where $h = 6.626 \times 10^{-34} \text{ m}^2 \text{ kg s}^{-1}$ is Planck constant, $m = 9.109 \times 10^{-31} \text{ kg}$ is mass of the electron and $E [\text{eV}]$ is its kinetic energy that can be tuned by set of the EM lenses. This for typically used values ($E < 200 \text{ eV}$) renders wavelengths that are in the order of magnitude of interatomic distances. In addition, due to their low energy, such electrons have a very low mean free path and are thus highly surface sensitive. LEED is commonly used for the identification of the atomic arrangement of the few topmost surface layers e.g. in 2D crystals or surface reconstructions (Figure 2.6)⁵⁴.

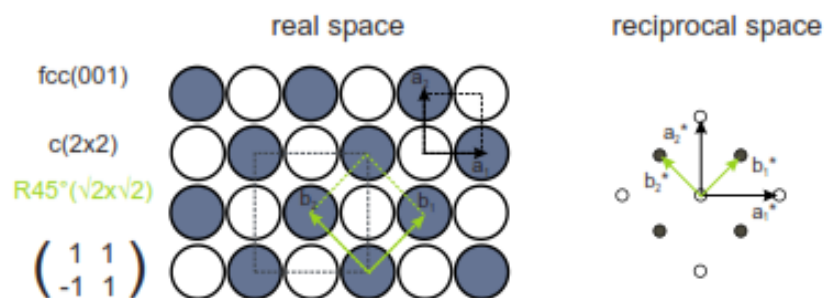


Figure 2.6. Illustration of a real and reciprocal space relations of fcc(001) surface with an overlayer superstructure. Black arrows represent substrate lattice vectors, while green ones belong to the superstructure.

2.6 SCANNING TUNNELING MICROSCOPY/SPECTROSCOPY

In the quantum world and under certain conditions, relatively small particles can pass through the energy barrier although their energy will be way smaller than the barrier. This effect carries the name quantum tunneling and is a consequence of uncertainty principle giving non-zero probability of finding particle on the other side of the barrier. In the simple example of a rectangular barrier, one can analytically solve the associated Schrödinger equation and demonstrate that tunneling is dependent on height, but more importantly on the width of the barrier – the probability decreases exponentially with increasing width. This was the principle Binnig and Rohrer used for creating the very first STM in an image where the distance between apex of a sharp metallic tip (ideally a single atom) and a sample d [m] represent the tunneling barrier for the electrons (Figure 2.7). When a small bias U [V] between them is applied⁶, certain electrons around the Fermi level E_f (within the $e \cdot U$ energy range, $e = 1.602 \times 10^{-19}$ C) are excited and can tunnel through the barrier, given that there is a level of the adequate (similar) energy on the other side of the barrier. The tunneling current I_t [A], regardless of its direction is given by:

$$I_t \propto \sum_{E_f - eU}^{E_f} |\psi_n(0)|^2 e^{-2kd} \quad (5)$$

where $\psi_n(0)$ are eigenvalues of the 1-D electron wave functions and k [nm^{-1}] is decaying constant that relates to the relative workfunctions of sample and tip.

As a consequence, the tunneling current is highly localized between the last atom in the tip apex and the sample and serves as a probe of Local Density of States of the sample under the assumption that the tip has a constant density of states. The experiment is conducted such that the tip is moved (scanned) over the sample with computer controlled

⁶ Depending on the technical realization of the bias, either sample or tip are kept at ground potential and depending on whether tip or sample is used to apply bias there are tip and sample biased machines. Since different machines are used in this thesis, the color of the scale bars at the images will be used to mark whether tip (white scale bar) or sample (black scale bar) bias is used

positioning via piezoelectric motors while the current is measured, allowing for the probing of the topography of the sample. It can be performed either in the constant current mode, when while scanning the distance is adjusted to keep current constant or in the constant height mode where the height is kept constant. Both these modes have their advantages and disadvantages^{73,74}. STM proved to be a very powerful technique for studying or manipulating on surface systems, especially when they lack periodicity and diffraction methods cannot be used.

Several extensions of STM exist today; first among them to mention would be the Scanning Tunneling Spectroscopy, where the tip is positioned above an object of interest and the bias is swept in a certain range while the tunneling current is recorded.

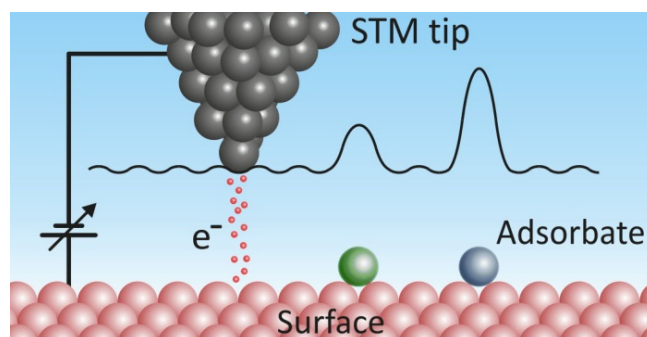


Figure 2.7. Illustration of the STM principle⁷⁵

By use of a lock-in amplifier, dI/dV

derivative which provides information about the LDOS as a function of electron energies is obtained. It is vastly used for probing interactions of spin bearing impurities on conducting surfaces in light of revived Kondo physics⁷⁶ or on superconducting ones in light of Majorana physics⁷⁷ but also other quantum effects on surfaces⁷⁸. The second derivative can be used for looking into the vibrations of the adsorbate or also spin-excitations in what is usually referred to as Inelastic Electron Tunneling Spectroscopy (STM-IETS)⁷⁹. Another important variation includes the use of magnetic tips for probing magnetic structures^{80,81}, superconducting tips for improving the resolution^{50,82} and most recently reading and writing to magnetic atoms in a STM-enabled single-atom electron spin resonance (ESR)⁸³. All of the recent (and probably future to come) developments of STM render it a very important tool for investigations of on surface systems, including the here investigated molecular architectures.

2.7 SAMPLE PREPARATION

Preparation of well defined, layered surface supported molecular architectures is only possible thanks to the aforementioned powerful and highly sensitive analytical tools. The sample preparation of the systems investigated throughout this thesis took place in the Surface Science Lab (Figure 2.1a). In general, the preparation process can be divided in two steps: 1) the preparation of atomically clean and smooth substrate, 2) the subsequent growth/deposition of metallic and/or organic films. In both processes quality and completeness of the produced layers is tracked by combining spectroscopy and microscopy techniques – XPS, LEED and STM.

Preparation of atomically clean and smooth substrates is accomplished by repetitive Ar^+ ion sputtering and annealing processes. During the sputtering, Ar gas is ionized and Ar^+ ions are accelerated by high voltage (1-2 kV) towards the sample under certain incidence angles (most efficient at 45 degrees), where during impact due to their high kinetic energy ions eject materials from the surface. Consequently the surface roughness is increased and annealing is necessary to recover the smooth surface. The quality of the surface is controlled by XPS used for detecting possible contaminants, but also by LEED and STM^{53,54}.

Once the surface is prepared, metallic films of around 20 ML are deposited on in a two-step process (2 x 10 ML), with a short break in between. During the break and the second deposition the sample is slightly heated. The deposition rate is measured by Quartz Crystal Micro Balance (QCMB) and tuned to allow surface diffusion of deposited material for creating smooth films. This is achieved by heating up the metals to their sublimation point in an e-beam evaporator where thermo-emitted electrons are accelerated towards the metal rod by the potential difference between them and the rod; upon collision, their kinetic energy is transferred into heat that is via geometrical constrictions localized on the tip of the metallic rod. For the creation of oxygen terminated films, the sample was exposed to 20 Langmuirs (L) of O_2 gas between two metal deposition cycles. Upon further metal deposition the O will float to the surface and form a $c(2 \times 2)$ superstructure. For this purpose, Cu(001) crystals are used for growth of both bare and oxidized Co and Ni films. Co and Ni films are

growing epitaxially (layer-by-layer) on these substrates, at least up to a certain thickness^{23,84–86}. Such prepared Co films exhibit an easy axis of their magnetization along the [110] direction (in-plane), while for Ni the easy axis points into the [001] directions (out-of-plane). It is also possible to manipulate the Ni anisotropy if the thin Ni film (up to 5 ML) is deposited on Co (7-10 ML), rendering the so-called in-plane Ni substrate.

Regardless of whether just a clean crystal or one with the ferromagnetic film is used for the experiment, the next step in sample preparation is molecular deposition. For this purpose, molecules are placed in a self-made heating pocket, crucible (similar to a Knudsen cell), and the temperature in this crucible is tuned to their sublimation point. Here, however there is no need for use of e-beam heater but rather normal heating element, due to way lower sublimation temperatures of molecules compared to the ones of metals. The sublimation rate is also followed by QCM and single or multilayers of molecules can be deposited by exploiting Physical Vapor Deposition so sometimes this process is also called Molecular Beam Epitaxy. The sample is kept at room temperature during the deposition, unless otherwise specified differently.

If the molecules are exhibiting a low vapor pressure and/or are thermally instable, thermal sublimation as previously described is not an option. Therefore, a significant effort has been put into establishing and improving a pulse-valve deposition method, where the desired molecules are injected into vacuum and onto the sample directly from solution through a small, needle-controlled orifice. The injection process is followed by annealing of the sample to remove the solvent, leaving the sample covered with molecules in a monolayer regime. More details about the method and optimization will be given in 102 of the thesis.

Chapter 3

RESULTS

3.1 NOVEL SPIN ARCHITECTURES

Investigations of various molecule-based spin architectures have so far been very fruitful leading to a number of observed effects and phenomena. Ordering in paramagnetic molecules on ferromagnetic or even diamagnetic substrates, realizations of SMMs and SIMs, varying the anisotropy of molecular spin-centers and formation of bound states are some among them. These discoveries are spurring further investigations on novel spin systems.

3.1.1 ASSEMBLIES AND MAGNETIC PROPERTIES OF CHROMIUM(II)- PHTHALOCYANINE MOLECULES

Following the seminal work of Scheybal et al.¹⁷ where he demonstrated that the spin of paramagnetic molecules adsorbed on ferromagnetic support, in this case MnTPPCL, can be stabilized at room temperature owing to its exchange interaction with underlying surface, many different spin-bearing metallo-porphyrins and phthalocyanines have been investigated upon adsorption on bare^{18–21,25,26} and functionalized^{22–24} ferromagnetic supports. In all the cases, the magnetic moments from molecular metal centers were following the magnetization direction of the substrate. Further on, it was found that, if their d-orbitals are more than half filled, they would couple ferromagnetically (FM) to bare substrates via direct or 90-degrees indirect exchange coupling, while on functionalized substrates, they would

couple antiferromagnetically (AFM) due to the 180-degrees superexchange mechanism. In some isolated cases, it was demonstrated that if the d-shell is less-than-half-filled, the interaction with ferromagnetic substrates can reverse the sign and the molecules couple AFM, however this is neither completely understood nor systematically investigated. In one of the mentioned cases of CrTPPCL molecules adsorbed on bare Co film, this is explained in the framework of the phenomenological Goodenough-Kanamori-Anderson (GKA) rules. In the following part, a systematic study of Cr(II)-phthalocyanine (CrPc) molecules on several ferromagnetic and non-magnetic supports will be presented. This investigation aims to first compare the interaction of CrPc and CrTPPCL molecules on Co substrates, but then also to test the integrity of the proposed deterministic coupling model.

The molecules were synthesized by our collaborating group of organic chemists from University of Bern, Prof. Dr. Silvio Decurtins and Dr. Shi-Xia Liu and characterized by means of mass spectrometry. Although ^1H NMR is a common technique for characterization in synthesis, this is not possible in case of molecules containing spin-active centers like the Cr^{2+}

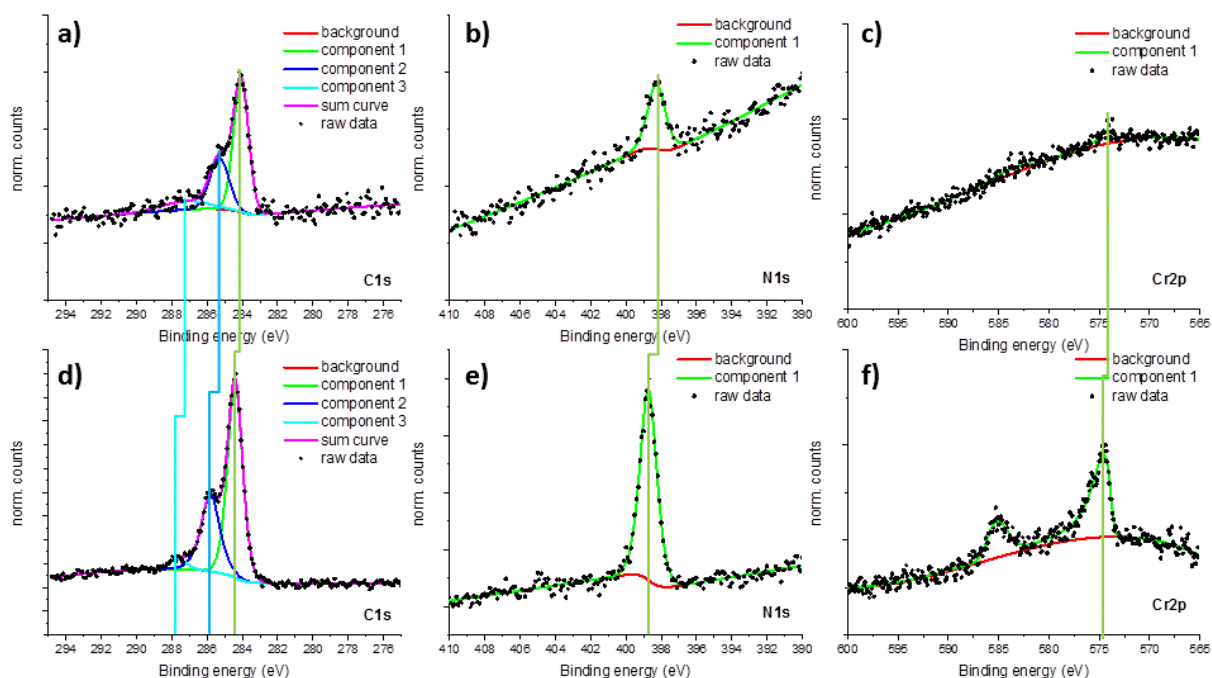


Figure 3.1 Deconvoluted C1s (a,d), N1s (b,e) and Cr2p (d,f) XPS spectra of ~1ML CrPc (a-c) and multilayer CrPc (d-f) on Au(111) substrate

ion as it leads to very high chemical shifts. The first steps before the investigation of their magnetic properties involved their characterization by means of XPS/UPS and STM to confirm their composition and stability upon thermal evaporation. The Cr atom in the molecule is in 2+ oxidation state with 4 electrons in the d-shell (d^4 configuration), but can easily exist in an energetically favorable 1+ state, where 5 electrons make the d shell half-full. Therefore we want to check its oxidation state upon adsorption on electron rich, Au(111) substrates. Once the sublimation parameters were obtained, monolayer first, and later multilayer (~ 10 layers) of CrPc molecules supported on Au(111) were probed by XPS. Figure 3.1 shows deconvoluted C1s, N1s and Cr2p XPS spectra of the mentioned monolayer and multilayer samples. The area of the peaks, with taking into account sensitivity factors for involved photoelectron peaks, gives the relative (atomic) ratios of elements Cr:N:C of 1:8.5:41 for monolayer sample and of 1:9:41 for multilayer sample, both of them being really close to stoichiometric ratio of 1:8:32 rendering that their composition is good upon sublimation. In addition, all the peaks for a monolayer sample have 0.3 eV lower binding energy than in multilayer sample (except Au4f that was used for referencing), most probably due to the interaction with substrate. The Cr2p peak is positioned at 574.6 eV in a multilayer sample, which corresponds to the binding energy found in the literature for

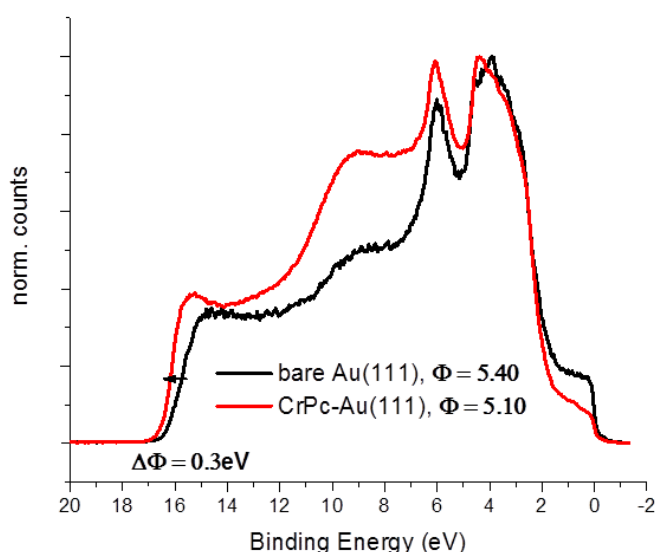


Figure 3.2 UPS spectra of bare (black line) and CrPc covered (red line) Au(111) surface

Cr^{2+} oxidation state^{25,87,88}, while in a monolayer one it is at 574.3 eV which is further down towards the 574.0 where neutral Cr^0 is reported⁸⁷, so it is possible that in that case Cr is in Cr^{1+} oxidation state. In order to glimpse into the substrate-molecule interactions, also UPS was employed and UPS spectra of clean Au(111) and 1ML CrPc/Au(111) are shown in Figure 3.2. In the region next to the

Fermi edge ($E_b=0$ eV), we can clearly see the strong decrease of intensity of low lying bands upon molecule deposition, most probably due to their strong interaction with the substrate. Further on the spectra show characteristic metallic features visible between 2 and 8 eV while in case of CrPc covered Au(111) also some molecular features are visible at higher energies up to 12 eV. At the higher end, cutoff of secondary electrons is visible. The workfunction of clean Au(111) is determined to be 5.4 eV and corresponds well to literature values^{89,90}, while it decreases by 0.3 eV upon CrPc molecules deposition. Both workfunction decrease and decrease in intensity of states close to Fermi edge are both clear indications of the interaction of the molecules and the substrate^{60,61}.

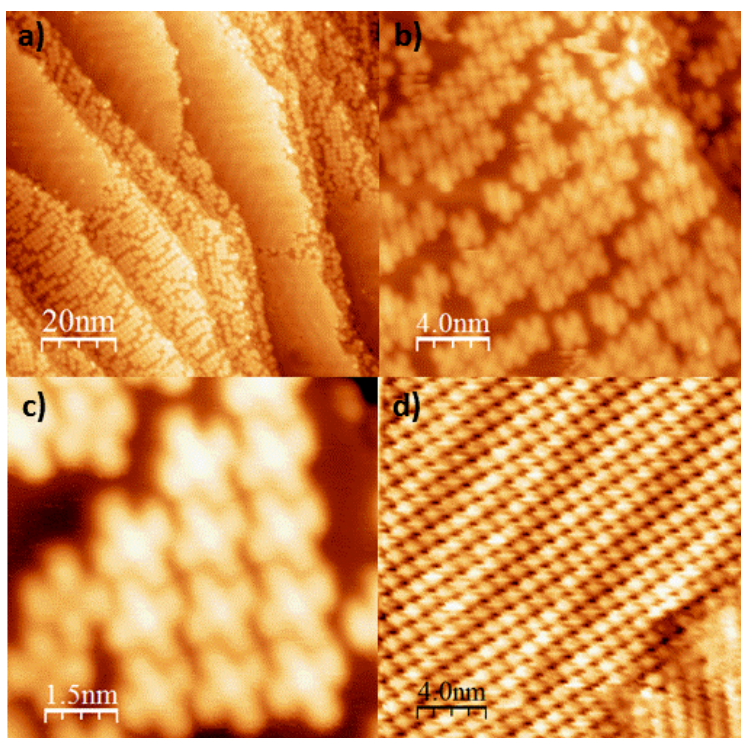


Figure 3.3 STM images of CrPc molecules on Au(111) surface demonstrating their self-assembly. Images (a-c) were recorded at $T=4.2$ K with $I_t=5$ pA and $U_{bias}=0.8$ V, while (d) was acquired at $T=100$ K with $I_t=10$ pA and $U_{bias}=-1.2$ V

The appearance and assembly of CrPc molecules on Au(111) was also investigated by STM. In Figure 3.3, STM images of several Au(111) samples having close to a full monolayer coverage of CrPc molecules are showed. Images are acquired at low temperatures to reduce the mobility of the molecules and improve resolution. The molecules, similar to most phthalocyanines, appear with characteristic 4-lobes and consequently 4-fold symmetric shape with additional protrusion in the center of the molecules.

At the coverage close to a monolayer, molecules are self-assembling into large islands while at a lower coverage coexistence of compressed assembly (big, smooth surfaces) and smaller assemblies (ensembles of several molecules) are present. Unfortunately, at the moment

when images were recorded, due to technical difficulties we couldn't perform STS measurements that could give us some information about molecule-substrate interactions, especially about the Kondo effect, but such measurements are planned in the near future. This system was nevertheless subject of XMCD investigations.

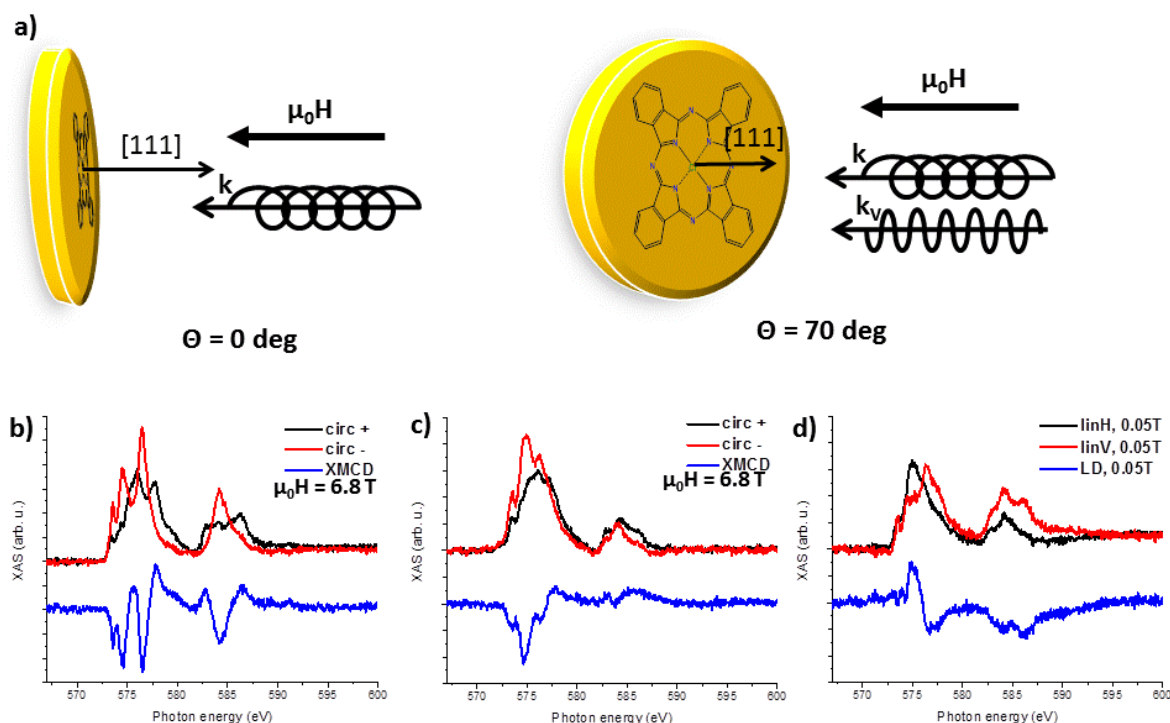


Figure 3.4 Illustration of the XMCD experiment and different sample geometries (a) with the XAS/XMCD spectra acquired at the magnetic field of 6.8 T and temperature of 2.5 K in normal (b) and grazing (c) incidence and XAS/LD spectra acquired in grazing incidence at the same temperature and magnetic field of 0.05 T (d)

First, CrPc molecules supported on Au(111) substrates were probed by means of XMCD spectroscopy at X-Treme beamline of the SLS, where investigations at very high magnetic field (up to 7 T) and very low temperatures (down to ~ 2.5 K) are possible. Samples were prepared and characterized in the Surface Science lab and transferred to the beamline, as it has been previously described. At the beamline, upon cooling down to the lowest possible temperature (~ 2.5 K), samples were probed by both linearly and circularly polarized X-rays in two sample geometries; normal X-rays incidence, with angle $\theta = 0$ between X-rays and sample normal and grazing X-rays incidence, with angle $\theta = 70$ between X-rays and sample

normal. The X-rays propagation vector and magnetic field vector are in both cases collinear, as indicated in the schematic representation of the experiment (Figure 3.4a). The results of this experiment are shown in the Figure 3.4b)-d) where the Cr XAS spectra with subtracted background and dichroic spectra are shown. The spectra acquired with linearly polarized light serve as a probe of molecule orientation on surface and dichroic signal visible in Figure 3.4d confirms planar adsorption on Au(111) substrate, as previously showed in STM experiments.

The shape and the position of XAS spectra also carry information about oxidation state and ligand field of the Cr atom. The Cr L_3 edge of XAS/XMCD spectra showed in the Figure 3.4 are showing 4 distinct features at 573.5, 574.6, 576.4 and 577.7 eV in normal and at 573.5, 574.9, 576.2 and 577.3 eV in grazing incidence with the lowest one lying far below 575.0 that is commonly reported for the Cr^{2+} XAS^{25,91,92}. A similar multiplet structure is reported for the Mn^{2+} ion from MnPc in d^5 electron configuration, with extremely high ligand field parameters^{51,93}. Both observations, together with previously mentioned XPS results hint towards the Cr ion being in Cr^{1+} oxidation state when adsorbed on Au(111). From the fully aligned spin state at the field of 6.8 T, we can extract magnetic moments of Cr by applying XMCD sum rules^{94,95} for orbital:

$$\mathbf{m}_L[\mu_B] = -\frac{4}{3} \frac{\int_{L_3+L_2} (C^+ - C^-) dE}{\int_{L_3+L_2} (C^+ + C^-) dE} \langle N_h \rangle \quad (6)$$

and the effective spin magnetic moment:

$$\mathbf{m}_{SE}[\mu_B] = m_S + 7m_T = -2 \frac{\int_{L_3} (C^+ - C^-) dE - 2 \int_{L_2} (C^+ - C^-) dE}{\int_{L_3+L_2} (C^+ + C^-) dE} \langle N_h \rangle, \quad (7)$$

where the integration of the circularly polarized XA spectra (C^+ , C^-) is over the energy range defined by the respective L_3 and L_2 edges and is calculated after a step function background has been deducted, $\langle N_h \rangle$ stands for average number of holes at a metal ion ($\langle N_h \rangle = 5$ for Cr^{1+} oxidation state). The term m_S stands for the spin magnetic moment and m_T is the intra-

atomic dipolar moment resulting from the spin-quadrupole coupling⁷¹. Table 3.1 contains values of magnetic moments obtain using (6) and (7) and taking into account spin moment correction factor of 2 for the overlap of L_3 and L_2 edges of Cr that is found to be independent on the Cr oxidation state⁹⁶.

Table 3.1 Obtained orbital and effective spin magnetic moments of CrPc/Au(111)

	normal	grazing
$m_{se} [\mu_B]$	1.5 ± 0.2	4.5 ± 0.7
$m_L [\mu_B]$	-0.02 ± 0.01	0.20 ± 0.03

The obtained magnetic moments show very strong angular dependence, with both spin and orbital moments increasing with increasing incidence angle, demonstrating clear in-plane anisotropy similar to the case of FePc molecules^{27,97,98}. In order to quantify the observed anisotropy by means of Magnetic Anisotropy Energy (MAE), magnetization curves are recorded and later fitted. Recording of the curves is done by sweeping the magnetic field up and down between -6.8 T and 6.8 T while acquiring signal at both XMCD peak (signal) and pre-edge (background for signal normalisation). In particular, we used the pronounced features from XMCD spectra at 574.6 eV as a signal and at 572.0 eV as a background for both normal and grazing incidence. The obtained curves were then scaled to match the obtained magnetic moments at 6.8 T and were fitted simultaneously using a Jiles-Atherton model for anhysteretic magnetization described by Gambardella et al.⁹⁹, after slight modifications. It is a classical model that does not take magnetic moment quantization into account, but was shown to give good results for systems where strong interaction/hybridization with support is present⁹⁹. In the used procedure the magnetization M was calculated as:

$$M = m \frac{\int_0^{2\pi} d\phi \int_0^\pi d\theta \sin\theta \cos\theta e^{-E(\theta_0, \theta, \phi)/k_B T}}{\int_0^{2\pi} d\phi \int_0^\pi d\theta \sin\theta e^{-E(\theta_0, \theta, \phi)/k_B T}} \quad (8)$$

where m is the magnetic moment of a single atom, θ_0 [°] defines the easy axis of magnetization, θ [°] is the polar and ϕ is the azimuthal coordinate of the measured magnetic moment while $E(\theta_0, \theta, \phi)$ is the magnetic energy function given by:

$$E = -\mathbf{m}\mathbf{B}\cos\theta - K(\sin\theta_0\sin\theta\cos\phi + \cos\theta_0\cos\theta)^2 \quad (9)$$

where K [meV] is the magnetic anisotropy energy of a single atom and \mathbf{B} [T] is the magnetic field. According to this, the curves were fitted with three free parameters: magnetic moment \mathbf{m} , magnetic anisotropy energy K and temperature T . Reaching the lowest possible temperature ($T \sim 2.5$ K) at X-Treme beamline depends on use of Mo/Ta paddle for crystal mounting and good contact of the crystal with it – sometimes if the contact is bad, temperature at the crystal surface can be different from the nominal temperature, so if fitting was performed with temperature taken as an open parameter it allowed for better result in fitting. The magnetization curves, together with the fit curves are shown in the Figure 3.5.

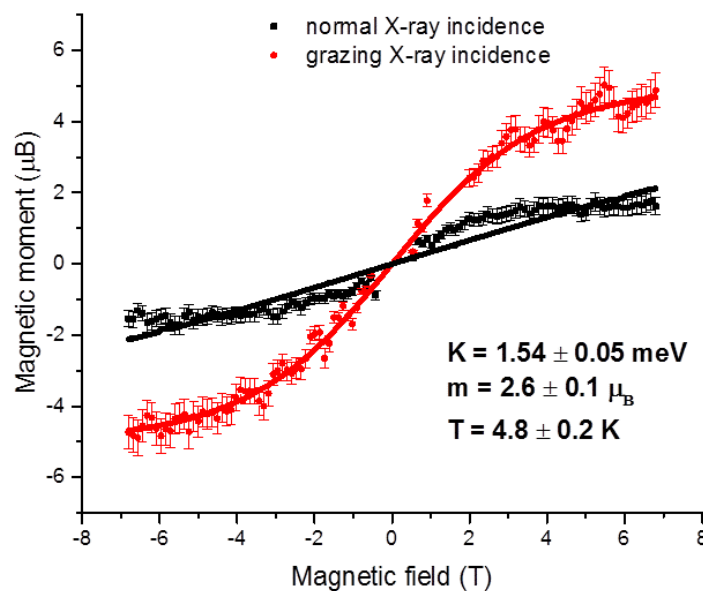


Figure 3.5 Fitted magnetization curves in two geometries, normal and grazing incidence of X-rays towards sample.

The best fit reveals in-plane magnetic anisotropy with $K = 1.54 \pm 0.05$ meV/molecule MAE, magnetic moment of $m = 2.6 \pm 0.1 \mu_B$ and temperature of $T = 4.8 \pm 0.2$ K. The value of the obtained MAE is 50% higher compared to the calculated values for in-plane systems like FePc/Cu(110)⁹⁸ but way lower than FeTPyP on Au(111)¹⁰⁰. The fit of the magnetization curve

in grazing incidence fits nicely to the data throughout whole range of magnetic field, however in the curve acquired in normal incidence that is not the case. The reason for this discrepancy might lie in possible magnetic interactions of Cr with and via the substrate that are not included in the fitting model or due to changes in magnetic moments due to anisotropic exchange interactions of orbital moments that can lead to different effective fields visible by magnetic moments^{101–104}.

Once the molecules and their magnetic properties were extensively characterized on non-magnetic support, in particular Au(111), the next step involved investigations of CrPc molecules on ferromagnetic supports. For this purpose, several supports with in-plane and out-of-plane easy magnetization axes were prepared according to procedures described in Section 2.7 and monolayers of CrPc deposited on them. In total five different systems were prepared, denoted as CrPc/Co, CrPc/O/Co, CrPc/Ni, CrPc/O/Ni and CrPc/Ni/Co. After characterization in the lab where the coverage and stoichiometry was checked by XPS, samples were transferred to SIM beamline of the SLS for XMCD investigations. Samples were after initial magnetization along the easy magnetization direction probed in remanence along the same direction, at several different temperatures.

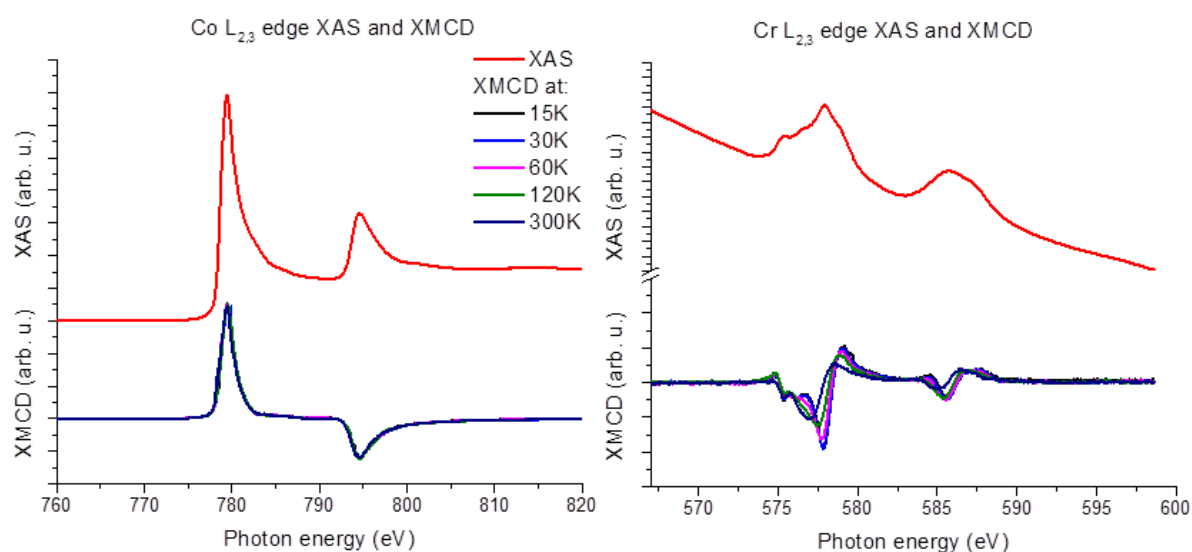


Figure 3.6 Temperature dependent XAS and XMCD measurements of Co and Cr in CrPc/Co measured in grazing X-ray incidence in remanence after initial magnetization

First among them was CrPc/Co that was probed in grazing incidence due to the in-plane orientation of the easy axis of the Co film. Summaries of the measurements of both Cr and underlying Co are presented in the Figure 3.6. For the temperature range used, there is no observable difference of the substrate magnetization, while clear temperature dependence is visible in case of Cr. The Cr peak, and main XMCD feature are positioned around 577.8 eV indicating Cr^{3+} oxidation state^{25,91,92}. The Cr magnetic moment is antiferromagnetically coupled to the underlying Co film, as evidenced by the opposite directions of the XMCD peaks which is in line with previous observation of AFM coupling of CrTPPCL molecules to same substrate²⁵. At the spectra acquired at the lowest temperature used in the experiments ($T = 15$ K), where the XMCD signal is the strongest, the sum rules were applied upon background subtraction to extract the magnetic moments of Cr using equations (6) and (7). This, with use of $\langle N_h \rangle = 7$ and application of correction factor yields $m_L = 0.01 \pm 0.01 \mu_B$ and $m_{SE} = 0.7 \pm 0.1 \mu_B$ for orbital and effective spin moments, respectively, indicative of low spin state $S = \frac{1}{2}$.

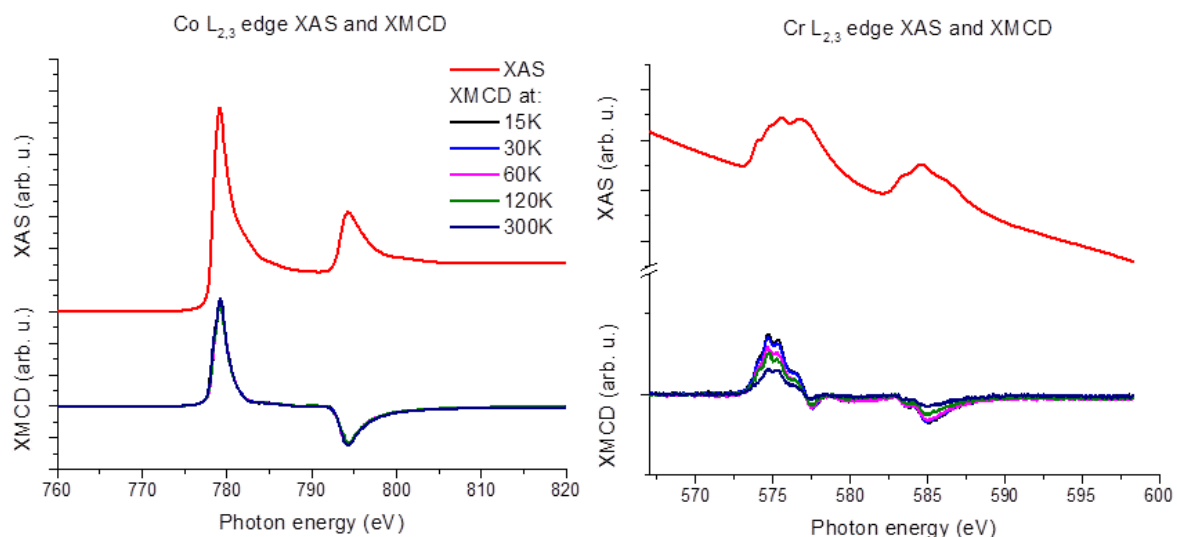


Figure 3.7 Temperature dependent XAS and XMCD measurements of Co and Cr in CrPc/O/Co measured in grazing X-ray incidence in remanence after initial magnetization

Next, CrPc/O/Co was probed also in grazing incidence. Similar to the measurements on bare Co, there is no change of XMCD of Co within the temperature range used (15-300 K), while Cr shows a temperature dependence as evidenced in the Figure 3.7. The Cr XAS shape

changed completely compared to the case of CrPc adsorbed on bare Co in that it got way broader, spanning on the lower end to 573.0 eV thus making oxidation state identification very difficult. It is known that phthalocyanine and porphyrin molecules adsorb above O atoms^{19,23}, and this could be origin of the XAS shape. The changes are also visible in XMCD - although a small feature was still observable at around 577.5 eV, most of the absorption line shifted to 574.7 eV, and more interestingly it evidenced FM alignment to the substrate magnetization. The oxygen functionalization is known to revert the interaction from FM to AFM due to superexchange coupling mechanism^{19,23}, however the inverse case was so far not observed. Since the position of main XMCD peak corresponds to the one on Au(111) (Cr¹⁺ oxidation state), we used $\langle N_h \rangle = 5$ to apply the sum rules that resulted in $m_L = 0.06 \pm 0.01 \mu_B$ and $m_{SE} = 1.9 \pm 0.3 \mu_B$ for orbital and effective spin moments. This would suggest spin state $S = 1$, however it is slightly contradicting to the presence of 5 electrons in the d-shell as there is no possible pairing that could leave 2 unpaired electrons. Using $\langle N_h \rangle = 6$ (Cr²⁺) for the sum rule analysis gives as a result $m_L = 0.07 \pm 0.01 \mu_B$ and $m_{SE} = 2.3 \pm 0.3 \mu_B$ and $S = 1$ is viable option. This would also possibly explain FM coupling via oxygen in a slightly modified GKA coupling mechanism. Nevertheless, since applying the sum rules to Cr is expected to result in large errors, both due to the overlap of L₂ and L₃ edges but also due to multiplet effects, DFT+U, as well as multiplet calculations are required towards a better understanding.

Further on, investigations were performed on molecules supported on Ni, known to be out-of-plane magnetized (easy axis perpendicular to the surface) and are showed in Figure 3.8. As expected, the substrate magnetization didn't vary significantly between the different temperatures. Cr XAS looks very much alike the data taken on Co and is positioned at 577.0 eV, just slightly lower than on Co. The XMCD on the other hand has completely different shape than on Co and exhibits 4 pronounced peaks at 577.6, 576.6, 574.9 and 573.8 eV, similar to the case of CrPc molecules on Au(111). Although Cr XMCD is extremely weak, it is FM aligned to the one of Ni, which is at first a bit surprising having in mind the AFM coupling to bare Co but can be expected if Cr is in Cr¹⁺ oxidation state with d⁵ configuration. This would however be slightly in conflict with GKA coupling scheme as described for the high

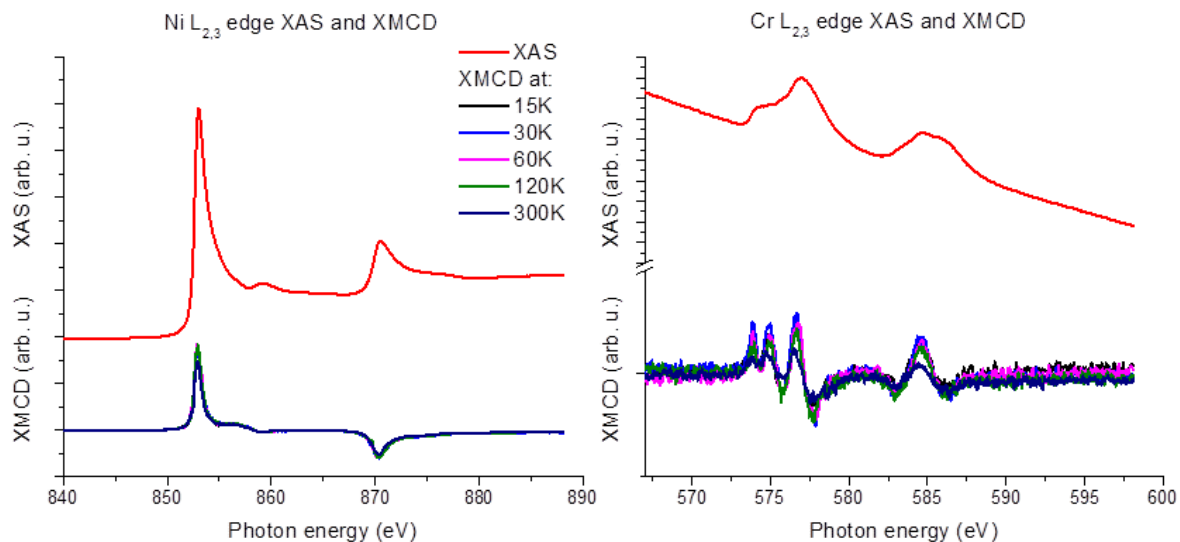


Figure 3.8 Temperature dependent XAS and XMCD measurements of Ni and Cr in CrPc/Ni measured in normal X-ray incidence in remanence after initial magnetization

spin Mn d^5 configuration in 25 as here the Cr is in low spin state. Sum rules analysis shows $m_L = 0.01 \pm 0.01 \mu_B$ and $m_{SE} = 0.2 \pm 0.2 \mu_B$, both within the error margin around 0. It is however unclear whether the weak XMCD is a consequence of the different magnetization direction, some intrinsic property or possibly a consequence of different sample temperatures.

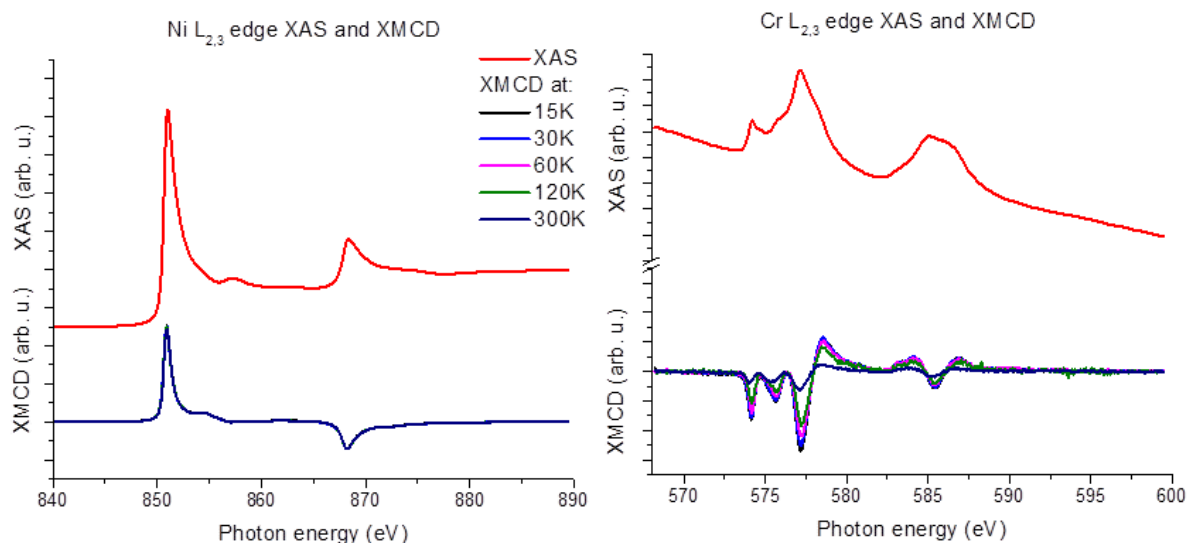


Figure 3.9 Temperature dependent XAS and XMCD measurements of Ni and Cr in CrPc/O/Ni measured in normal X-ray incidence in remanence after initial magnetization

CrPc molecules on oxygen terminated Ni substrate on the contrary to bare Ni exhibit very strong dichroic signals, as evidenced in Figure 3.9. The Cr XMCD signal reduces 3 times going from 15 to 300 K, while the Ni XMCD signal doesn't show changes in this range. Cr XAS is very similar to the one when molecules are adsorbed on bare Ni but is on slightly higher energy – 577.2 eV⁷. The XMCD also looks identical to the one of Cr on Ni, but is reversed and AFM coupled to the one of Ni. Here again, coupling could be understood if the d^5 electron configuration of Cr is assumed. The O adlayer would flip the orientation of the detected Cr XMCD. It is though surprising that no changes in XAS are observed. Sum rules revealed sizable magnetic moments, namely $m_L = 0.21 \pm 0.04 \mu_B$ and $m_{SE} = 2.5 \pm 0.4 \mu_B$, with possible spin state $S = 1$ or $3/2$. This also demonstrates that it is not the magnetization direction that causes low moments in case of bare Ni.

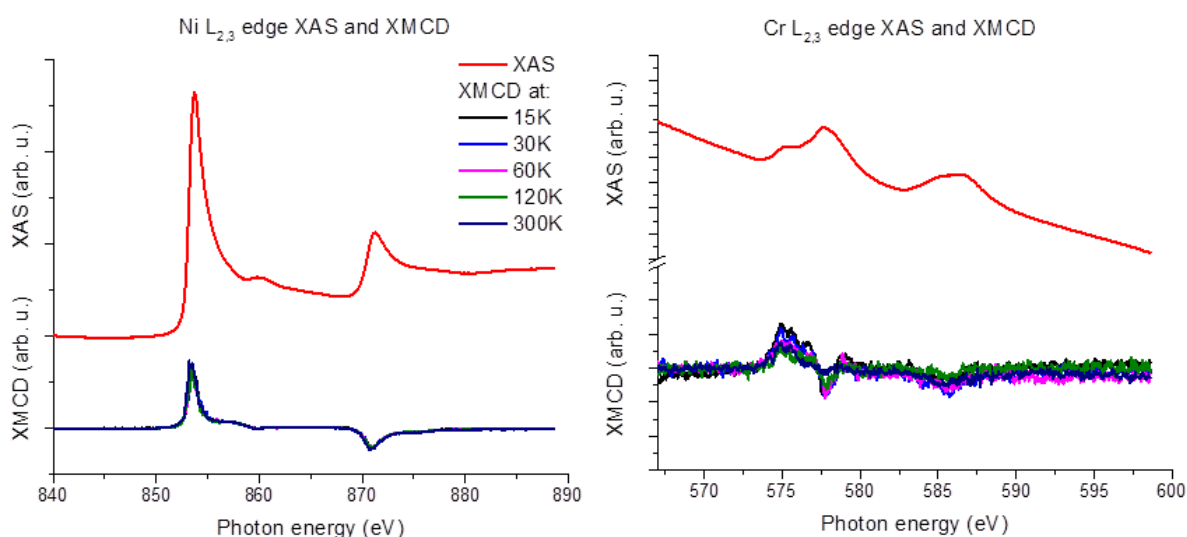


Figure 3.10 Temperature dependent XAS and XMCD measurements of Ni and Cr in CrPc/Ni/Co measured in grazing X-ray incidence in remanence after initial magnetization

Last from the series was the CrPc on thin Ni film grown on Co that induces in-plane magnetization, so probing was again in grazing incidence. The idea for this system was to probe the interactions of Cr without changing the chemical environment while changing the

⁷ Some of the experiments were performed at different beamlines of SLS and slight energy deviations can originate from discrepancy in monochromator calibrations

magnetization direction. Ni and Cr XAS and XMCD spectra are showed in Figure 3.10. Cr XAS looks similar to ones on Ni and O/Ni, but also like one on Co, positioned at 577.8 eV. The XMCD shows two features, one at the same energy and pointing to the opposite direction with respect to Ni XMCD but very weak, and a stronger one pointing to the same direction as Ni at 575.0 eV so overall coupling seems to be FM. Magnetic moments obtained from sum rules are $m_L = 0.06 \pm 0.02 \mu_B$ and $m_{SE} = 0.5 \pm 0.3 \mu_B$ similar to the case of bare Ni, giving the impression that interaction with Ni, although inducing same oxidation state with and without oxygen adlayer is very weak in case of bare Ni and enhanced when mediated by oxygen due to change of coupling mechanism and orbitals involved in interaction. Additionally, it was reported for the FePc molecules that when adsorbed on O functionalized surfaces, charge transfer and symmetry reduction enhance the magnetic moment of Fe and change the anisotropy to out-of-plane^{98,105}. It can be that similar mechanism takes place in the case of CrPc molecules.

The last part of characterization of CrPc molecules interactions with ferromagnetic supports was determination of energies of exchange interactions. Several authors showed that the magnetic coupling of molecules to substrates can be approximated within the mean field model as an interaction with an effective field of the substrate. The coupling strength is then quantified by modelling the relative molecular magnetization's temperature dependence^{41,106}:

$$M_{mol}(T) = M_{sub}(T) \cdot B_J \left(\frac{E_{ex}}{k_B T} \right) \quad (10)$$

by use of the Brillouin function $B_J(x)$

$$B_J(x) = \frac{2 \cdot J + 1}{2 \cdot J} \coth \left(\frac{2 \cdot J + 1}{2 \cdot J} \cdot x \right) - \frac{1}{2 \cdot J} \coth \left(\frac{1}{2 \cdot J} \cdot x \right) \quad (11)$$

where J is the total magnetic moment of a molecule (integer or half integer) M_{mol} and M_{sub} are the magnetizations of the molecule and the substrate, respectively, k_B is the Boltzmann constant and T is the temperature. Due to a very high Curie temperatures of the used films (700 - 1000 K), M_{sub} is nearly independent on the temperature in the range of 15 – 300 K (change of less than 5%) and was therefore considered constant during fitting procedure.

For all the Cr XAS/XMCD spectra showed in Figures 3.6-3.10, the XMCD to XAS ratio was calculated for each temperature at the certain photon energy as determined by the most pronounced XMCD feature. The ratios are presented in absolute scale, disregarding their relative orientation to substrate magnetization. Such obtained ratios were then fitted by equation (10), calculating J ($J = L + S$) values using the sum rules obtained S and L values. It is worth mentioning that these were at the same time best fits looking at χ^2 values and associated errors. The results are shown in Figure 3.11. The strongest interaction, although also with large error, is obtained for CrPc molecules on bare Co (21 ± 7 meV), followed by the one on O/Co (19 ± 3 meV). Although barely any Cr moment was obtained from the sum rules for Ni and Ni/Co substrates, the exchange energies amount to 12 ± 2 and 10 ± 3 meV respectively. The value for the exchange energy on O/Ni is found to be 14 ± 2 meV, which is higher than on bare Ni. This is at first unexpected, but the combination of anisotropy and J change due to the interaction with O seem to enhance the exchange coupling strength. The values are slightly lower than what is obtained for similar molecules supported on ferromagnetic substrates, however this goes in line with low obtained moments and strong anisotropic effects associated with CrPc on all substrates.

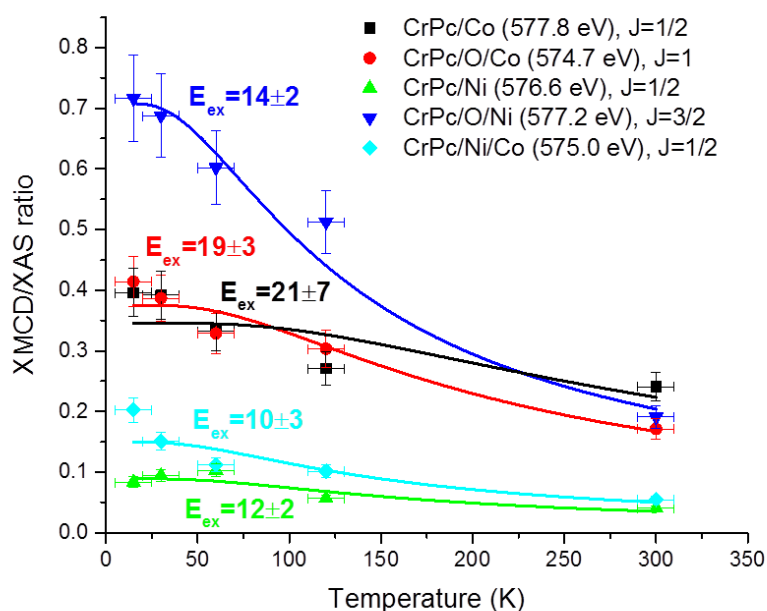


Figure 3.11 Fitted temperature dependence of XMCD/XAS ratios at fixed photon energy (given in parenthesis) for determination of exchange energies (showed in meV) of CrPc molecules interactions with various ferromagnetic substrates with J values as determined by sum rules

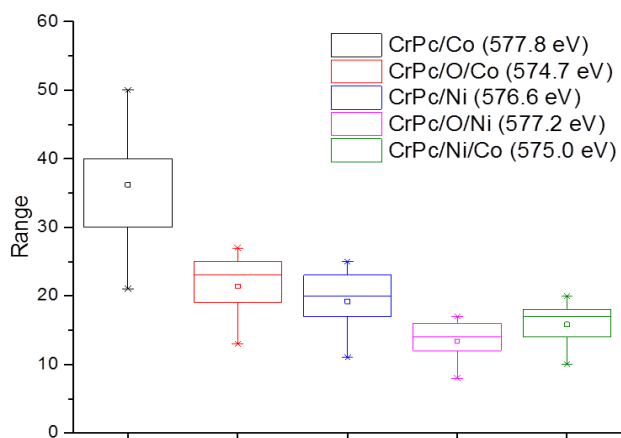


Figure 3.12 Graphical representation of the obtained exchange energies (in meV) of the interaction of CrPc molecules with different ferromagnetic supports by fitting with different J . Values in bracket represent photon energy at which the ratios were calculated

In addition, to test the sensitivity of the determined exchange energies on the total magnetic moment, the fitting was performed also for other J values between $1/2$ and $5/2$ and the results have been summarized in Table 3.2 but also graphically in Figure 3.12. It is visible that the values, but also trends can be significantly influenced if an improper J value is used for the fit. This is especially important if, there are big fluctuations of magnetic moment as it is the case for Cr.

Table 3.2 Exchange energies (in meV) of the interaction of CrPc molecules with different ferromagnetic supports obtained by fitting with different J . Highlighted in red are the values with experimentally determined J values

	$J=1/2$	$J=1$	$J=3/2$	$J=2$	$J=5/2$
CrPc/Co	21 ± 7	30 ± 10	40 ± 20	40 ± 20	50 ± 20
CrPc/O/Co	13 ± 2	19 ± 3	23 ± 3	25 ± 3	27 ± 3
CrPc/Ni	12 ± 2	17 ± 5	20 ± 6	23 ± 6	25 ± 7
CrPc/O/Ni	8 ± 1	12 ± 2	14 ± 2	16 ± 2	17 ± 3
CrPc/Ni/Co	10 ± 3	14 ± 4	17 ± 5	18 ± 5	20 ± 6

The comprehensive study of interactions of CrPc molecules with various substrates demonstrate how the spin state of such molecules may depend crucially on the interaction with the substrate on which they are adsorbed. The interactions on Au(111) demonstrate very strong anisotropy of the Cr magnetic moment that might bring also an anisotropic coupling of orbital moments into play. The coupling with bare ferromagnetic substrates, Co and Ni (also Ni/Co) are different in both intensity and sign, showing that the relative

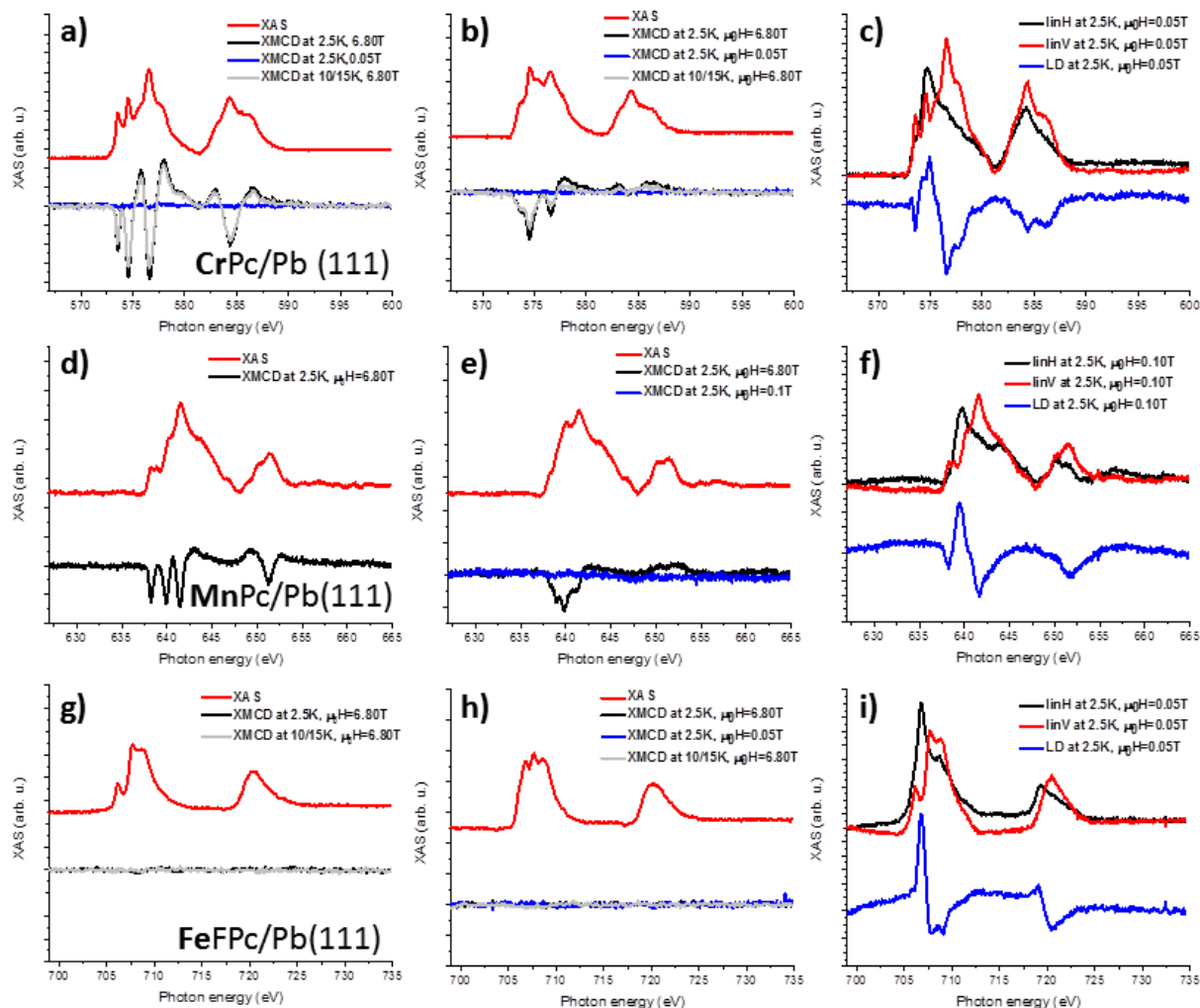
orientation of the molecule's and the substrate's easy magnetization axes can also be important for paramagnetic molecules, not only for the SMMs/SIMs. It also hints that the treatment beyond the GKA model is needed for the coupling interpretation. Introduction of an O adlayer changes the symmetry of adsorption sites and the ligand field, causes reorganization of the orbitals as visible in spin state change and in the change of anisotropy of molecules. Although in both cases the spin state increased, it leads to a reduction of the exchange energy in the case of Co, and to an increase of the same in case of the Ni. Further theoretical investigations, namely DFT+U and multiplet calculations are expected to give deeper insight into involved interactions that for sure need to be treated beyond classical Heisenberg model to include interactions of orbital magnetic moments.

3.1.2 INTERACTIONS OF VARIOUS PHTHALOCYANINE MOLECULES WITH Pb(111) SUPPORT

One of the main prerequisites for the application of atoms or spin-bearing molecules in a spintronic device is to have a sufficiently long magnetization relaxation time. This can be achieved in systems with strong Magnetic Anisotropy (MA), low Quantum Tunneling of Magnetization (QTM) and low scattering of electrons and phonons from the substrate. In case of molecules, the active spin center(s) were investigated by protecting/embedding them in an organic medium to reduce interactions with the environment and use ligand field to induce anisotropy. This led to realization of surface-adsorbed organometallic complexes with MA in the order of several meV. Alternatively, the molecules were adsorbed on the superconductor, this lead to the largest magnetic anisotropy energy of about 10 meV achieved, since the magnetic moment is stabilized by the superconducting gap^{49,107}. In other investigations on Pb(111) surfaces the formation of ordered layers of molecules⁴⁶ with the signatures of the Kondo effect⁴⁷ were demonstrated. In the case of MnPc molecules that are strongly interacting with the substrate, this creates a magnetic scattering potential for the quasi-particles of the superconductor and gives rise to so-called Yu–Shiba–Rusinov (Shiba) states, especially interesting in light of heavy fermion, i.e. Majorana physics⁵⁰.

Most of the mentioned research focused on local-probe techniques for investigations of the interplay of magnetic and superconducting properties of on-surface molecular architectures. This can sometimes provide obstacles as there can be significant interactions between the tip and the system, thus causing big perturbations. Therefore we wanted to focus our investigations on spectroscopic investigations of the phthalocyanine assemblies on Pb(111) substrates by means of XAS/XMCD spectroscopy. For a better understanding, these systems were investigated at temperatures below and above bulk superconducting critical temperature of $T_c = 7.2 \text{ K}$ ^{108,109}, in particular at $T = 2.5 \text{ K}$ (nominal) and $T = 10$ (in some case 15) K. In addition, the investigations were performed also below critical magnetic field values $\mu_0 H_c = 80 \text{ mT}$ ^{108,109} and above up to 6.8 T. Although in such a high field the superconductivity of Pb is destroyed, these investigations help to get better understanding in physico-chemical

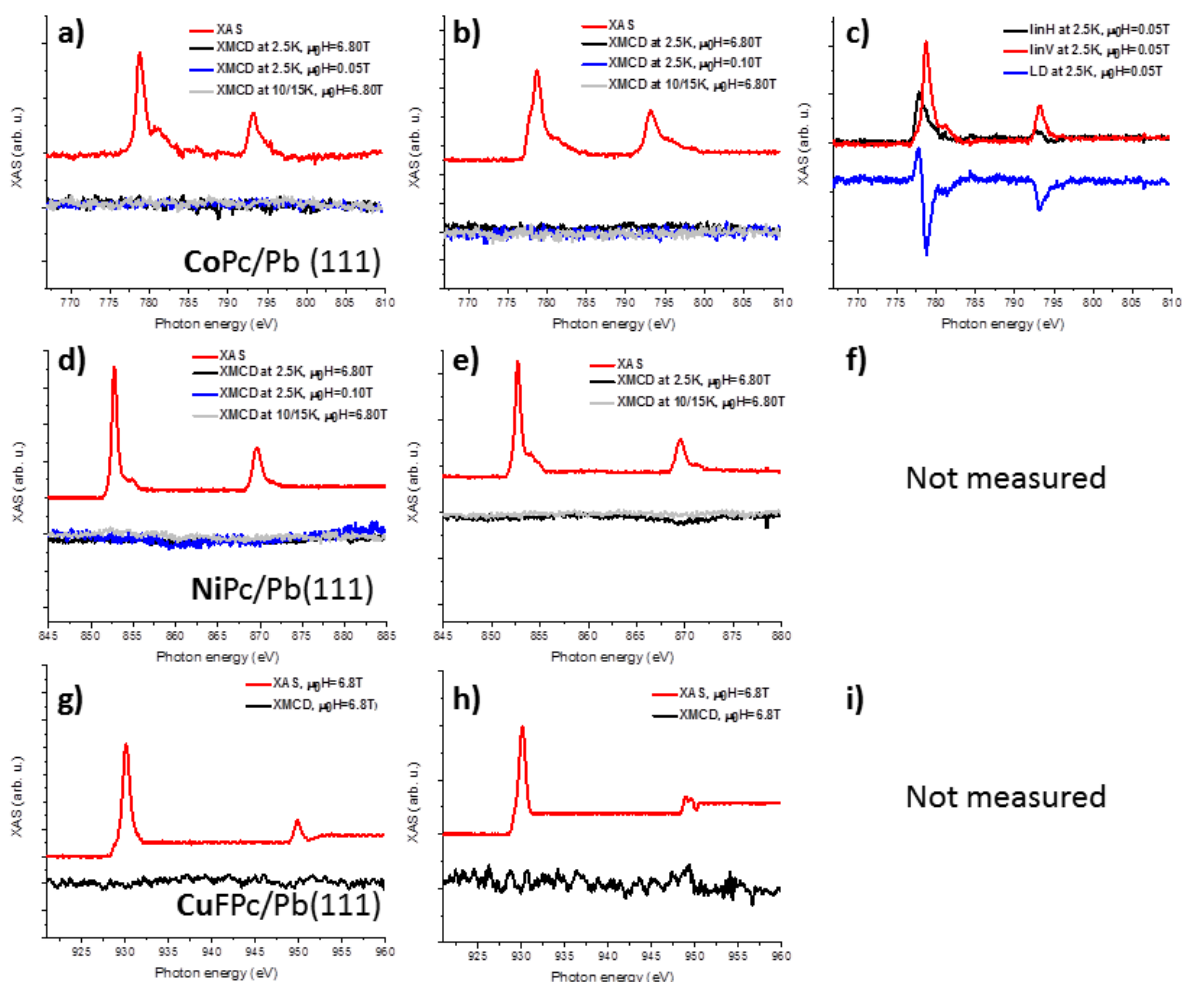
interactions of molecules and Pb substrate that are not driven by superconductivity. Last, in light of our recent observation of stable long-range ferrimagnetic ordering in the spin array consisting of MnPc and FePc molecules coassembled on Au(111)⁵¹, we wanted to investigate such coassembly also on Pb(111).



Figures 3.1.13 Cr (a-c), Mn (d-f) and Fe (g-i) XAS and XMCD L-edge spectra acquired in normal (first column) and grazing (other two columns) sample geometries. Spectra in first two columns are acquired with circularly polarized light (red-XAS@2.5K, black-XMCD@2.5K, 6.8T, blue-XMCD@2.5K, 0.05T, gray-XMCD@10/15K, 6.8T) while ones in the third column with linearly polarized (black-LinH@2.5K, 0.05T, red-LinV@2.5K, 0.05T, blue-LD=LinH-LinV)

Samples were prepared and characterized in the Surface Science lab and transferred to the X-Treme beamline, where probing at low temperatures and high magnetic fields is possible. Similar to the case of CrPc/Au(111), all here investigated samples were probed by

both linearly and circularly polarized X-rays in normal and grazing geometries. For all the acquired spectra, backgrounds are subtracted and results are shown in Figures 3.1.13 and 3.1.14. The spectra acquired with linearly polarized light serve as a probe for the molecular orientation on the surface. These dichroic signals which are visible for all probed systems confirm planar adsorption on Pb(111) substrate in agreement to previously reported cases^{46,50}.



Figures 3.1.14 Co (a-c), Ni (d-e) and Cu (g-i) XAS and XMCD L-edge spectra acquired in normal (first column) and grazing (other two columns) sample geometries. Spectra in first two columns are acquired with circularly polarized light (red-XAS@2.5K, black-XMCD@2.5K, 6.8T, blue-XMCD@2.5K, 0.05T, gray-XMCD@10/15K, 6.8T) while ones in the third column with linearly polarized (black-LinH@2.5K, 0.05T, red-LinV@2.5K, 0.05T, blue-LD=LinH-LinV) (Co only)

As evidenced by the presented spectra, the XMCD signal is only observed for CrPc and MnPc molecules adsorbed on Pb(111), which is slightly unexpected, especially for the FeFPc and CuFPc. For CoPc and NiPc, this is not so surprising as both of them were also quenched on Au(111) albeit for different reasons. Further on, XMCD was not observable regardless of the applied magnetic field strength or the sample temperature. This hints that the origin of the absent XMCD signal / magnetic moment is not related to the superconducting state of Pb(111), but rather to how Pb atoms are interacting with the FeFPc and CuFPc molecules. In addition, a shift of the XAS peak of about 2 eV is present in case of all quenched molecules compared to the reported literature values^{27,39,51,93} indicating some charge redistribution effects. Moreover, a significant change of the XAS shape is visible for these molecular systems, but additional experimental (STM, UPS) and theoretical treatment (DFT+U, Multiplets) is required for elucidation of this behavior. On the other hand, Cr XAS/XMCD spectra correspond very well to the spectra observed for the same molecules on Au(111), with very distinct features and positioned around the same photon energy. A very small difference was visible between the two temperatures the measurements had been performed at (2.5 and 10 K) reflected in reduction of intensity of XMCD signal as it is expected. A similar situation was observed with Mn, whose XMCD also showed typical distinct features as reported earlier on Au(111) and located at the same photon energies. For both CrPc and MnPc spectra, we have applied a sum rules analysis in accordance to (6) and (7) with using $\langle N_h \rangle(\text{Cr}^{1+}) = 5$ and $\langle N_h \rangle(\text{Mn}^{2+}) = 5$ and correction factors for these oxidation states (2 for Cr^{96} , 1.47 for $\text{Mn}^{2+ 110}$). The results of the analysis are summarized in Table 3.3.

Table 3.3 Obtained orbital and effective spin magnetic moments for CrPc and MnPc molecules on Pb(111)

	CrPc/Pb(111)		MnPc/Pb(111)	
	normal	grazing	normal	grazing
$m_{se} [\mu_B]$	0.8 ± 0.2	2.8 ± 0.4	1.7 ± 0.2	1.8 ± 0.3
$m_L [\mu_B]$	0.04 ± 0.01	0.10 ± 0.03	0.03 ± 0.01	0.15 ± 0.03

CrPc, as it was the case on Au(111), shows a strong in-plane anisotropy as evidenced by the immense increase of both of the moments in grazing incidence data. MnPc also shows an in-plane anisotropy, but only in the orbital moment on the contrary to Cr where both of them increased. Surprisingly, the Mn spin moment seems almost completely isotropic. In order to quantify the observed anisotropies, magnetization curves were recorded by sweeping the magnetic field and following the changes in the XMCD signals. For this purpose, we used the pronounced XMCD features from the spectra at 574.6 / 639.9 eV as a signal and at 571.5 eV / 637.0 eV as a background at both normal and grazing incidence for Cr / MnPc molecules, respectively. The curves were then scaled and fitted according to the procedure described in 3.1.1 and are shown in the Figure 3.1.15. For the CrPc molecules the fit showed an anisotropy energy of $K = 1.3 \pm 0.2$ meV MAE and $m = 1.7 \pm 0.2 \mu_B$ while for the MnPc molecules the fit showed a very low anisotropy energy, $K = 0.18 \pm 0.02$ meV MAE as anticipated and $m = 2.3 \pm 0.1 \mu_B$ which is well in line with the values obtained by sum-rules analysis.

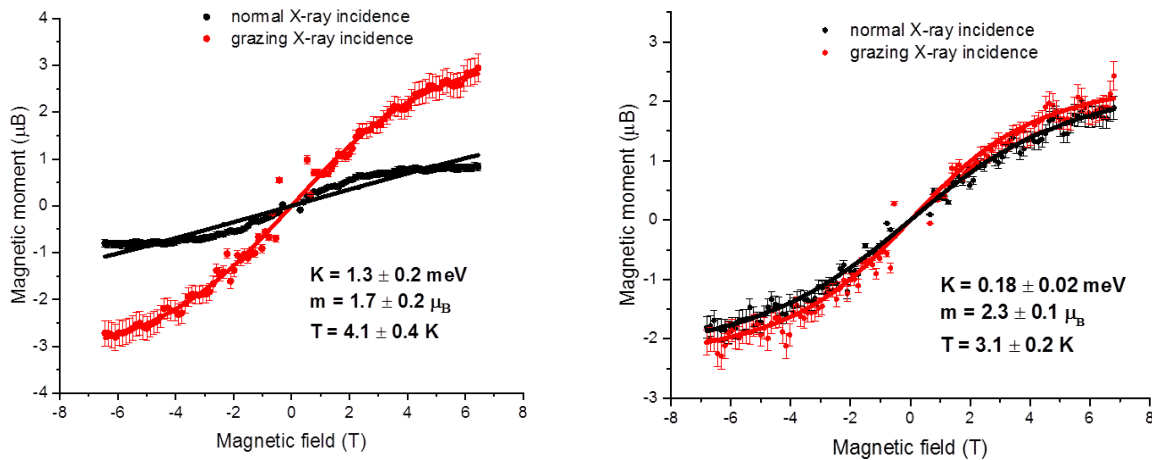


Figure 3.1.15. Fitted magnetization curves of CrPc (left) and MnPc(right) molecules supported on Pb(111) in two geometries, normal and grazing incidence of X-rays towards sample

Expanding the spatial extent of Shiba bound states would allow remote coupling of magnetic systems through a superconducting gap, enabling easier manipulation of Majorana quasiparticles and the creation of novel topological quantum devices. Majorana

quasiparticles have recently been created in direct interaction of closely assembled Fe single atoms on superconductor^{77,111} but have been reported to be of very short range character. A proposed alternative approach takes advantage of the spatially oscillating character of decaying Shiba states to enable chiral ordering through the RKKY coupling mechanism^{112,113}. Therefore we wanted to investigate possible interactions of our periodic spin array of coassembled FeFpc and MnPc molecules on a superconductor. This was significantly hindered by our observation that FeFpc molecules are quenched on Pb(111) substrate, but nevertheless it was interesting to check whether there are changes in the MnPc signals in such periodic spin array.

Phthalocyanine molecules have been demonstrated to self-assemble on Pb(111) in a similar manner like on Au(111)^{46,50,82}, however, we wanted to check whether this will also happen in the case when FeFpc is used (no fluorinated phthalocyanines were used in reported studies) or in the case of directed assembly used to create our chessboard like spin arrays. Therefore we have decided to probe these systems by STM. In the Figure 3.1.16, acquired images of FeFpc molecules on Pb(111) are shown. Similar to the non-fluorinated phthalocyanines, FeFpc was on rougher parts adsorbed on steps (left), while on smoother areas the molecules started assembling into chains or molecular islands (middle and right). Interestingly, in several images, FeFpc molecules appeared in a strange round shape (indicated with arrow in the middle image) as they were spinning.

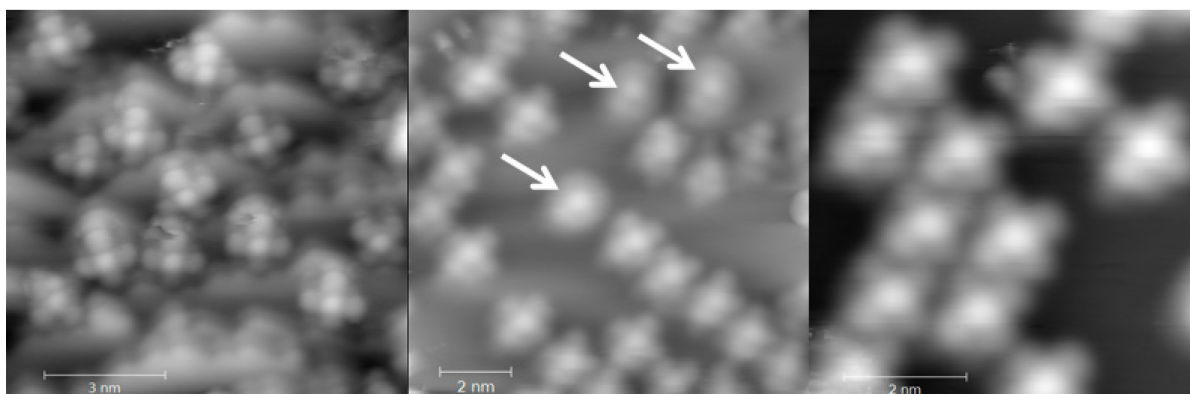


Figure 3.1.16 FeFpc molecules adsorbed on small terraces (left) and smoother areas (middle and right) of Pb(111). White arrows are indicating several molecules that appeared rather round than squared as usual. Images recorded at 4.2 K with $I_t = 100$ pA, $U_{bias} = -2.0$ V (left) and $I_t = 20$ pA, $U_{bias} = -1.5$ V (middle and right)

In the second case of directed assembly, results of voltage dependent measurements are shown in Figure 3.1.17, where it is clearly evident that MnPc and FeFPc molecules are assembled in an alternating manner also on Pb(111). Once the presence of the co-assembled network was confirmed by checking at several positions on the sample, in the next step we have employed STS to probe it. Figure 3.1.18 shows an assembly of 16 molecules (8 MnPc and 8 FeFPc) with indicated tip positions (above metal center) for Spectroscopy measurements (left), together with the averaged result of the measurements (right). Differential conductance spectra of FeFPc show a flat line evidencing that the quenching of magnetic moment is not

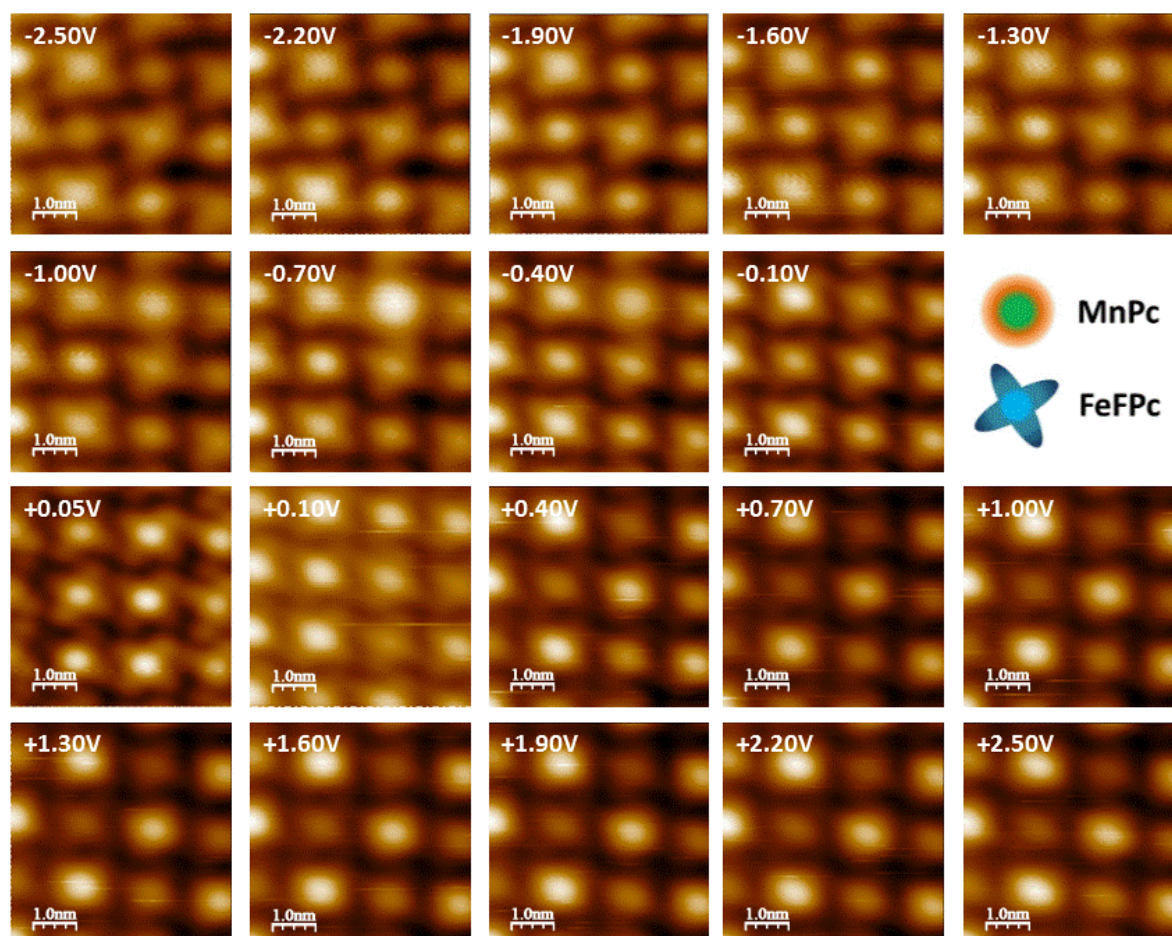


Figure 3.1.17 Voltage dependent STM images of MnPc and FeFPc molecules coassembled on Pb(111). 5 nm x 5 nm images were recorded at $T = 4.2$ K with the current setpoint of $I_t = 50$ pA, while biases are indicated on every image.

due to the Kondo interactions. The MnPc on the other hand demonstrates a clear peak around zero bias - similar, albeit broader than the ones reported by Franke et al.⁸². Interestingly, all 8 molecules in the investigated frame showed the same feature (averaging was just used to reduce noise level) on the contrary to the demonstrated Moiré pattern in the aforementioned work. This might be an indication of the collective interaction of the periodic array with the underlying Pb surface, in similarity to the same network supported on Au(111)⁵¹. The XMCD measurements shown in Figure 3.1.19 didn't show any apparent difference to the investigated layers of solely FeFPc or MnPc molecules, so they were not further analyzed.

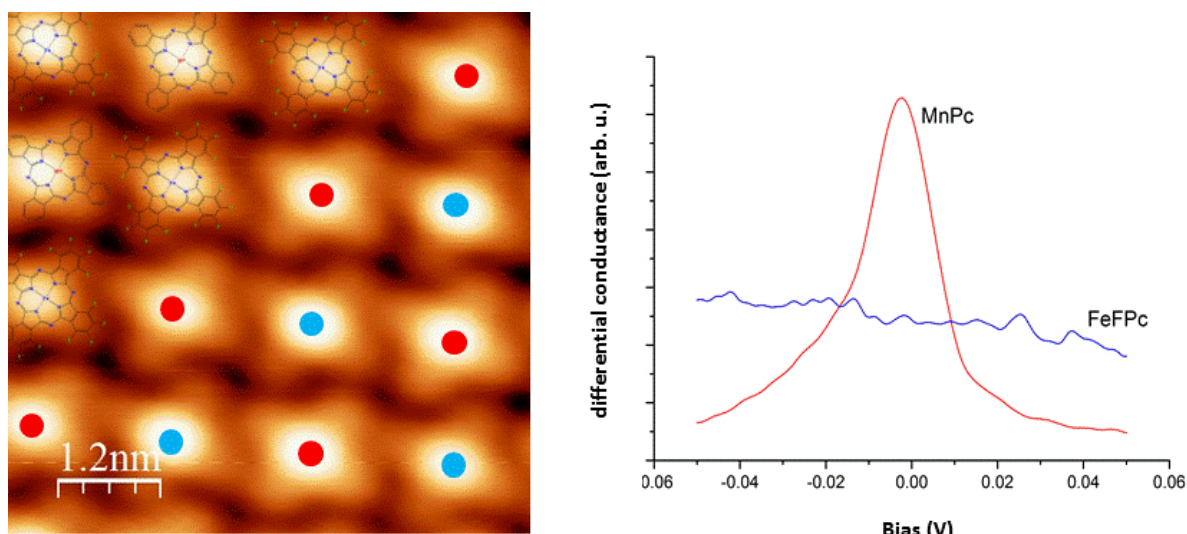


Figure 3.1.18 6 nm x 6 nm STM image of MnPc and FeFPc molecules coassembled on Pb(111) acquired at 4.2 K with $I_t = 50$ pA and $U_{bias} = 0.05$ V. Assembly of 16 molecules (8 MnPc and 8 FeFPc) with indicated tip positions (above metal center, red-Mn, blue-Fe) for Spectroscopy measurements (left), together with the averaged result of the measurements (right).

The shown results demonstrate the importance of X-ray investigations in complementarity to local probe techniques to investigate the coupling of spin systems to a superconductor. Although they can drive a system out of the superconductive phase in case when magnetic field is used like in here presented cases, it was shown that sometimes properties of the system won't depend greatly on whether system is or is not in the superconducting phase. This is making X-ray investigations even more important. In turn, this can help us, through better understanding how components interact, predict their

behavior in a combined manner, and also allow screening of the possibly interesting systems for deeper investigation or application in novel quantum devices.

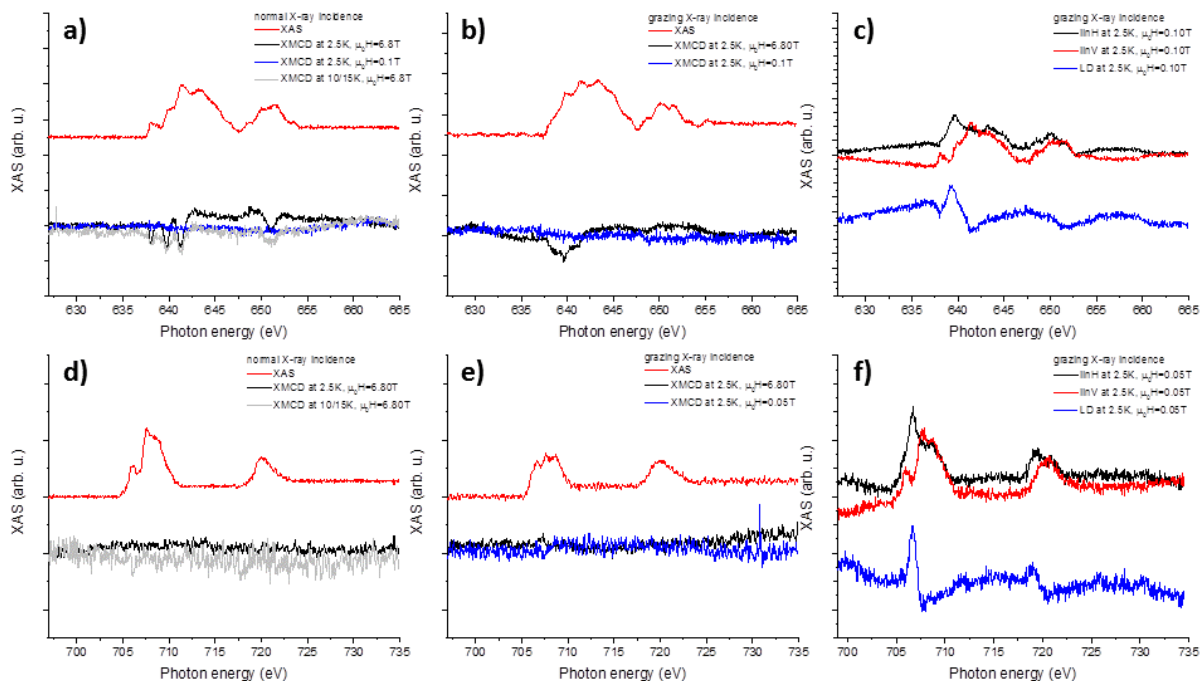


Figure 3.1.19 Mn (a-c) and Fe (d-e) L-edges XAS and XMCD spectra acquired in normal (first column) and grazing (other two columns) sample geometries of an alternating spin array coassembled on Pb(111). Spectra in first two columns are acquired with circularly polarized light (red-XAS@2.5K, black-XMCD@2.5K, 6.8T, blue-XMCD@2.5K, 0.05T, gray-XMCD@10/15K, 6.8T) while the ones in the third column with linearly polarized (black-LinH@2.5K, 0.05T, red-LinV@2.5K, 0.05T, blue-LD=LinH-LinV)

3.2 INTRA- AND INTER-MOLECULAR INTERACTIONS

Magnetic phenomena on the single molecule level are typically of intrinsic origin, for example the magnetism of SMMs or SIMs, also the strong anisotropies that are reported for some classes of molecules. In other cases, contrasting to the intrinsic ones, magnetic phenomena can be of collective origin and can be a consequence of the interactions of molecules with a larger entity – like electrons or atoms in a substrate or of the interaction of larger numbers of molecules. We will here address some cases where these intra- and inter-molecular interactions were manifested by the emergence of interesting magnetic phenomena.

3.2.1 MAGNETIC PROPERTIES OF HOMO- AND HETERO-METALLIC TRIPLY-FUSED PORPHYRINS

Most of the on-surface investigation of SMMs/SIMs on the Lanthanide based compounds that could be used for preparation of molecular layers demonstrated very peculiar properties^{7,9,10,13,14,98}. The inaccessibility of low-lying 4f states of these compounds by means of local probing techniques, however, hindered their wider application. The ability to create ordered layers of another class of molecules, namely triply-fused ZnZn-bisporphyrin¹¹⁴ inspired the investigations on newly created alternatives where instead of Zn atoms, spin-active metals such as Mn and Fe were incorporated in the extended π -conjugated system. Molecules were synthesized by our previously mentioned organic chemistry partners from University of Bern. Similar to the case of CrPc molecules, ¹H NMR was not viable option for characterization of the products of synthesis. On the other hand, UV-VIS spectroscopy proved to be a very good tool to discriminate between normal and singly- and triply-fused porphyrins by investigating the relative intensities of their Soret and Q-bands. For the normal porphyrin, the Soret band was usually way more intense than the Q-bands, in singly-fused porphyrins it was about twice as intense, while in the triply-fused porphyrins they were of equal intensities^{115,116}. Therefore UV-VIS spectroscopy was our choice for identifying the products of synthesis, in particular the existence of triply-fused

bisporphyrins. Several porphyrin compounds (Structures given in Figure 3.2.1a) were dissolved in two different solvents, MTBE and DCM and recorded UV-VIS (300-800 nm) spectra are shown in Figure 3.2.1 (b, c).

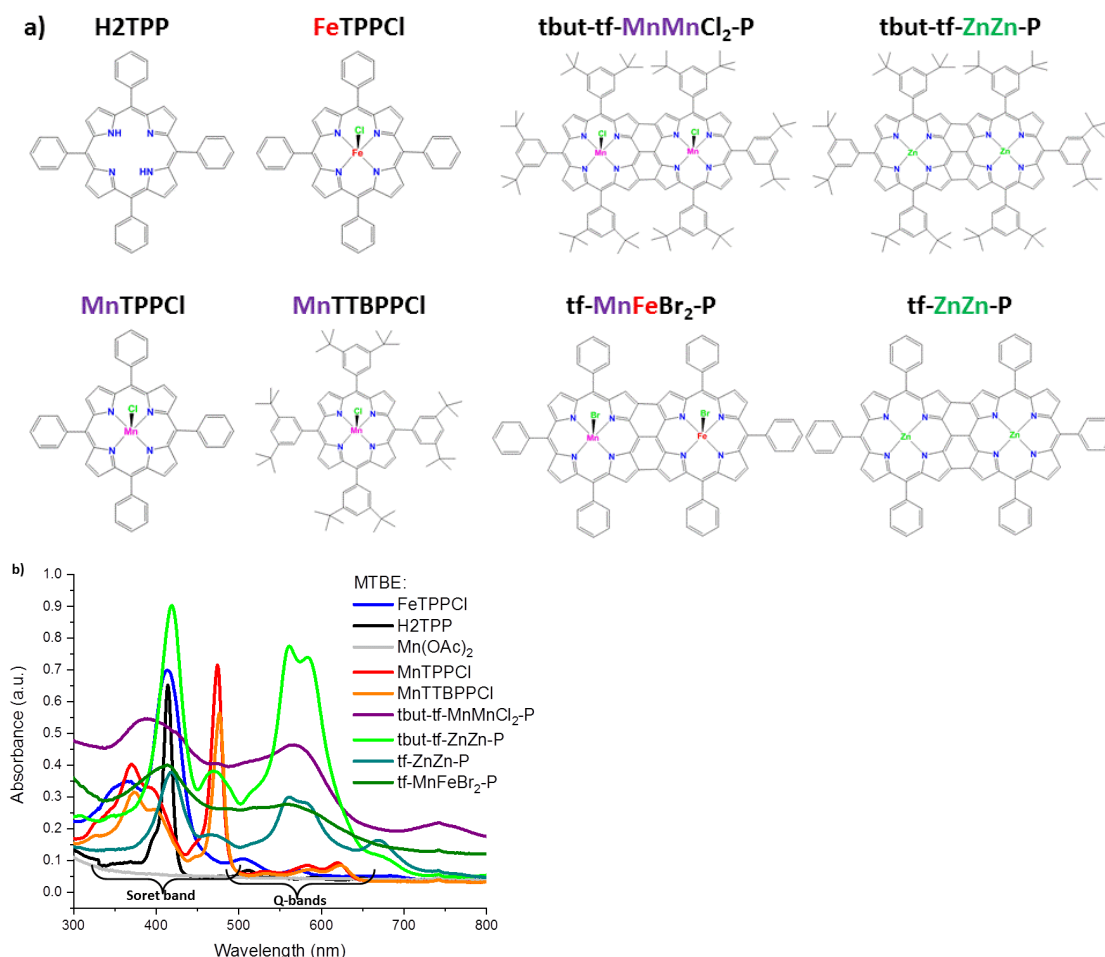


Figure 3.2.1 Molecular structures (a) and UV-VIS spectra of different porphyrin compounds dissolved in MTBE (b) and DCM (c). Since the purpose of the experiment was qualitative interpretation, concentrations of solutions were tuned to keep absorbance in the range of validity of Lambert-Beer law.

Equal intensities of the Soret and Q-bands of tf-MnFeBr₂-P and tbut-tf-MnMnCl₂-P molecules unambiguously confirm the presence of fused porphyrin dimers. The bands are, similar to the cases of single porphyrins further broadened due to MLCT (and LMCT) and d-d transitions¹¹⁷. The increase of the absorbance with decreased wavelength is most probably due to some impurities (small alkyl chains) still present in the powder.

Once the presence of the triply-fused dimers was confirmed for the $\text{tf-MnFeBr}_2\text{-P}$ and $\text{tbut-tf-MnMnCl}_2\text{-P}$ molecules, these two compounds were subjected to XAS/XMCD experiments, at first in their bulk (powder) form. Results of the experiments are summarized in Figure 3.2.2 for $\text{tbut-tf-MnMnCl}_2\text{-P}$ molecules and in Figure 3.2.3 for $\text{tf-MnFeBr}_2\text{-P}$ molecules.

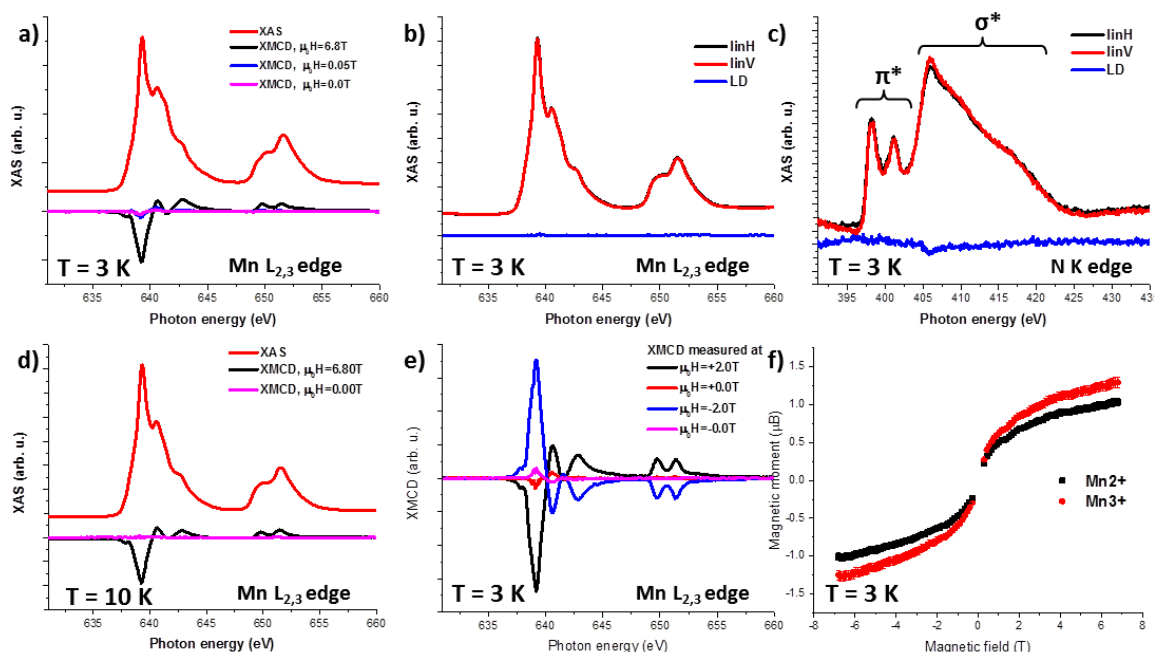


Figure 3.2.2 Mn (a,b,d,e) L-edges XAS/XMCD/LD spectra, N (c) K-edge XAS/LD and Mn Magnetization curve (e) acquired at $T=3\text{K}$ (a-c,e,f) and $T=10\text{K}$ (d) in normal sample geometry of the homometallic compound i.e. $\text{tbut-tf-MnMnCl}_2\text{-P}$ molecules powder. Spectra in (b) and (c) are acquired with linearly polarized light, while circularly polarized light was used for all other experiments shown. In e) XMCD signals at ± 2 T, and as well as at ± 0 T measured after magnetization to ± 2 T are shown (sign \pm indicates the direction 0 T was reached, in + 0 by ramping down from + 2 T and in - 0 by ramping up from - 2 T)

The position and the shape of Mn XAS suggests presence of both Mn^{3+} and Mn^{2+} oxidation states. This is unexpected for regular porphyrins containing only one metal atom which are usually found in the Mn^{3+} state^{23,118,119}. As expected for the powder samples, there is no dichroism visible in either Mn (Figure 3.2.2b) or N (Figure 3.2.2c) XAS spectra acquired with linearly polarized X-rays. At the N K-edge, two distinct features originating from $1s \rightarrow \pi^*$ transitions and broad feature originating from $1s \rightarrow \sigma^*$ transition are visible. These are typical for metal containing porphyrin molecules^{15,120–122}. The XMCD shows a distinct peak at

639.3 eV that is, also visible, but significantly weakened at 0.05 T and is even remanent at zero field and $T = 3$ K. Additionally, the remanent magnetization flips the sign with reversing the preceding magnetic field direction, indicating its magnetic origin (Figure 3.2.2e) but completely vanishes at the temperature of $T = 10$ K demonstrating its weak nature. Nevertheless, observing remanent magnetization in this case is a very interesting result that requires further elucidation. Due to the observed different oxidation states of the Mn ion, we have analyzed the spectra acquired at 6.8 T by applying the sum rules analysis in two ways, once assuming Mn being in its 2+ and once in the 3+ oxidation state. If we assume the Mn^{2+} state, the analysis provides a moment of $m_{\text{se}}(\text{Mn}^{2+}) = 1.0 \pm 0.1 \mu_B$ and of $m_L(\text{Mn}^{2+}) = 0.01 \pm 0.01 \mu_B$. In the Mn^{3+} case slightly higher values for the effective spin and orbital moments $m_{\text{se}}(\text{Mn}^{3+}) = 1.2 \pm 0.1 \mu_B$ and $m_L(\text{Mn}^{3+}) = 0.01 \pm 0.01 \mu_B$ are found taking into account different number of d-holes and correction factors. Both results are suggesting an $S=1/2$ state of the Mn central metal atom in the porphyrin cage. The magnetization curves that are acquired in the same way as established for the previously investigated systems show that the magnetization is not reaching saturation up to an applied magnetic field of 6.8 T (Figure 3.2.2f).

The origin of the observed remanence is not plausibly caused by intermolecular interactions as these big and bulky molecules are forming an amorphous and disordered solid phase leading to the conclusion that it has to be of intramolecular origin. Therefore, to understand the remanence of the examined bi-porphyrin system, we shall first address the presence or absence of Mn^{2+} ions on the basis of our data. Mn^{2+} is not typically contained in porphyrin systems and our XAS/XMCD data does not show similarities to reference Mn^{3+} porphyrin molecules we have probed (Figure 3.2.4d,g). This provides a hint that indeed, the Mn^{2+} ions are responsible for the observed peculiar magnetic properties. There are several reasons that could lead to the appearance of Mn^{2+} ions. Since the $\text{Mn}(\text{OAc})_2$ is used as a source of the Mn ions that are upon oxidation inserted into porphyrin, it could originate from some $\text{Mn}(\text{OAc})_2$ leftovers. Therefore we have measured XAS/XMCD spectra of $\text{Mn}(\text{OAc})_2$ powder at the same conditions. We have not observed signs of remanence in this case (Figure 3.2.4j,k). Therefore, even if some $\text{Mn}(\text{OAc})_2$ leftovers are present, these cannot

be responsible for the observed remanence. In another scenario it might be possible that some of the Mn ions are ligated with 2 Cl atoms and thus are coordinated in an octahedral ligand field¹¹⁹ or that some fraction of the Mn ions is without axial counterion. This is not observed for porphyrins in bulk powders or in solution, but the latter might occur upon their adsorption at and interaction with surfaces needed to stabilize the Mn^{2+} ion. In the case of bisporphyrins, it might also be a consequence of large delocalization of electrons in the π -conjugated system. It is indeed calculated that for triply-fused porphyrins the HOMO states exhibit a charge separation between the single porphyrin units of the triply-fused bisporphyrin^{123,124} that might act to stabilize Mn^{2+} ion. Although it is not completely understood what the origin of the observed remanence is, it is clear that it is an intrinsic molecular property and involves interaction (spin and/or charge) of Mn^{2+} and Mn^{3+} species through the delocalized electrons. Theoretical calculations in the framework of DFT+U would definitely contribute to a better understanding of the system.

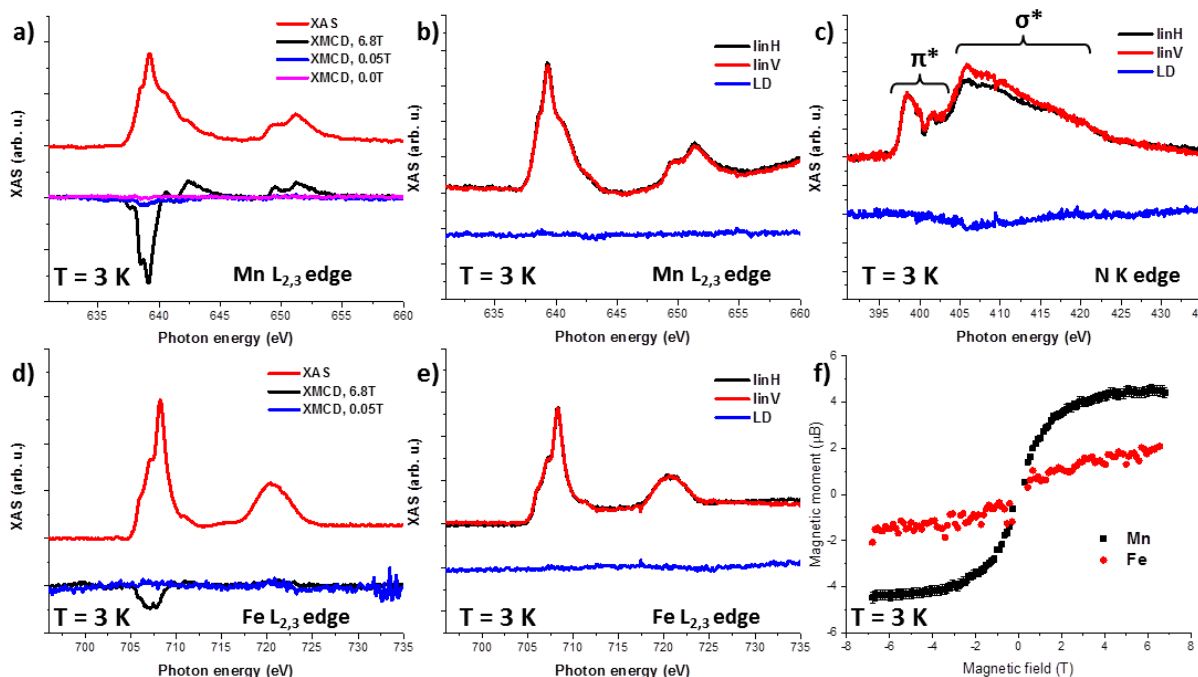


Figure 3.2.3 Mn (a,b), Fe (d,e) L-edges XAS/XMCD/LD spectra, N (c) K-edge XAS/LD spectra and Mn/Fe Magnetization curves (e) acquired at $T=3\text{ K}$ in normal sample geometry of the heterometallic compound i.e. *tf*- $\text{MnFeBr}_2\text{-P}$ molecules powder. Spectra in (b), (c) and (e) are acquired with linearly polarized light, while circularly polarized was used for all the other

In the case of tf-MnFe-Br₂-P, the identification of the oxidation states is slightly easier – the position and the shape of the Mn XAS peaks provide evidence for the presence of Mn in the Mn²⁺ oxidation state. This is similar to the case of MnTPP taking the Mn²⁺ oxidation state after adsorption to Co^{23,125} (see also Figure 3.4.8). Fe appears to be in Fe³⁺ state with a shape similar to the one of the reference FeTPPCI (Figure 3.2.4a). The XMCD of Mn shows strong signal peaking at 639.15 eV, while one of the Fe is rather low and positioned at 707.10 eV. Applying the sum rules provides the following values for the effective spin and orbital magnetic moments: $m_{se}(Mn^{2+}) = 4.0 \pm 0.3 \mu_B$ and $m_L(Mn^{2+}) = 0.45 \pm 0.05 \mu_B$, for Mn and $m_{se}(Fe^{3+}) = 1.2 \pm 0.1 \mu_B$ and $m_L(Fe^{3+}) = 0.15 \pm 0.01 \mu_B$ for Fe. In this analysis the number of d-holes (5 for both) and the correction factors (1.47 for Mn²⁺, 1.46 for Fe³⁺¹¹⁰) have been considered. This suggests that the center metal atoms are found in the following spin state: $S_{Mn} = 2$ and $S_{Fe} = 1/2$. Interestingly, both metals show a sizable orbital moment (~12% of the effective spin moment) but no remanence has been observed. Like in the case of the other powder materials, there is no dichroism visible in Mn (Figure 3.2.3b), Fe (Figure 3.2.3e), and N (Figure 3.2.3c) XAS spectra acquired with linearly polarized X-rays. In the N K-edge, instead of two sharp and distinct features visible in the π^* region for the other triply-fused (Figure 3.2.2c) or normal porphyrin molecules (Figure 3.2.4c,f,i), a rather broad peak is present with a feature at around 402 eV characteristic for the free base porphyrin (Figure 3.2.4l). This could indicate that in this case not all of the molecules are fully metallated.

Inspired by the interesting and versatile magnetic behavior of the two fused porphyrins, we wanted to investigate their behavior on surfaces, but have experienced severe problems with subliming them. This led to the implementation of a procedure for pulse valve deposition of these molecules directly from solution into the vacuum as it has been described in Section 3.4.2. In this way, we successfully deposited them on ferromagnetic Co substrate in a monolayer regime (according to XPS and XAS data, we lack STM data though) and have probed their interaction with the underlying substrate. The samples were, upon initial magnetization along easy magnetization direction probed at grazing incidence of the X-ray beam, in remanence at room temperature (RT) and at around 20 K (LT). XAS and XMCD spectra of both Mn (from both molecules) and Fe resemble very well the spectra of single

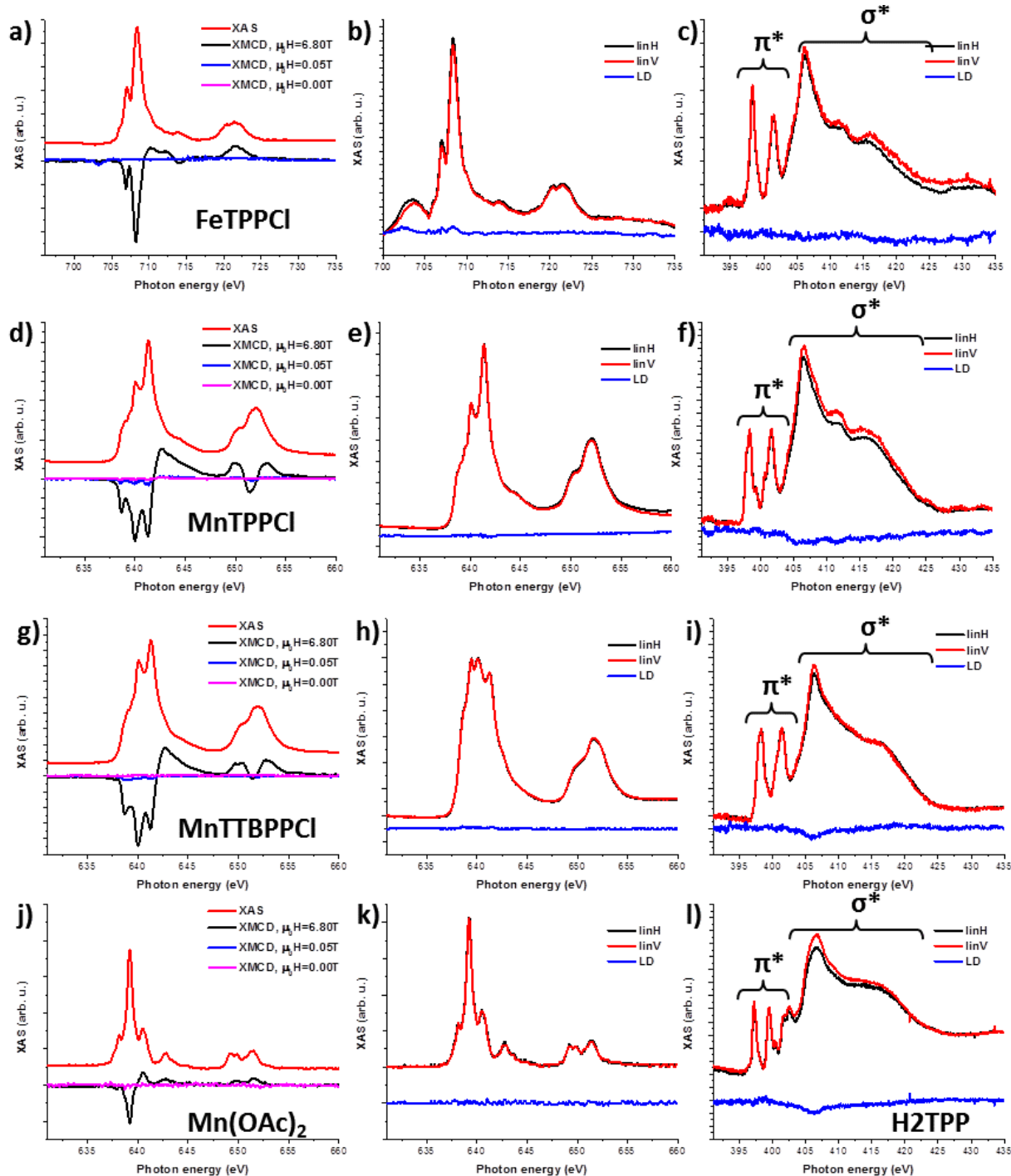


Figure 3.2.4 Fe (a,b), Mn (d,e,g,h,j,k) L-edges XAS/XMCD/LD spectra and N (c,f,i,l) K-edge XAS/LD spectra acquired at $T=3\text{K}$ in normal sample geometry of reference powder compounds: FeTPPCI (a-c), MnTPPCI (d-f), MnTTBPPCI (g-i), Mn(OAc)₂ (j,k) and H2TPP (l). Spectra in (a), (d), (g) and (j) are acquired with circularly polarized light, while linearly polarized light was used for all the other presented spectra. Structures of the porphyrin compounds are shown in Figure 3.2.1a

MnTPPCL and FeTPPPCL porphyrins supported on Co (Figure 3.4.8) as evidenced in Figure 3.2.5 (for *tbut-tf-MnMnCl₂/Co*) and in Figure 3.2.5 (for *tf-MnFeBr₂/Co*). The molecules are FM exchange coupled to the underlying Co substrate, and the XMCD signals of Mn and Fe increased in both cases with the decrease of the temperature, confirming the exchange origin of the observed magnetic moments. At the point of writing this thesis it was not tried to quantify the strength of the interaction as this experiment was a part of trial measurement at only 2 temperatures that would yield large error for the exchange interaction assessment. The detailed measurements at several temperatures are planned and would be performed in the nearest future.

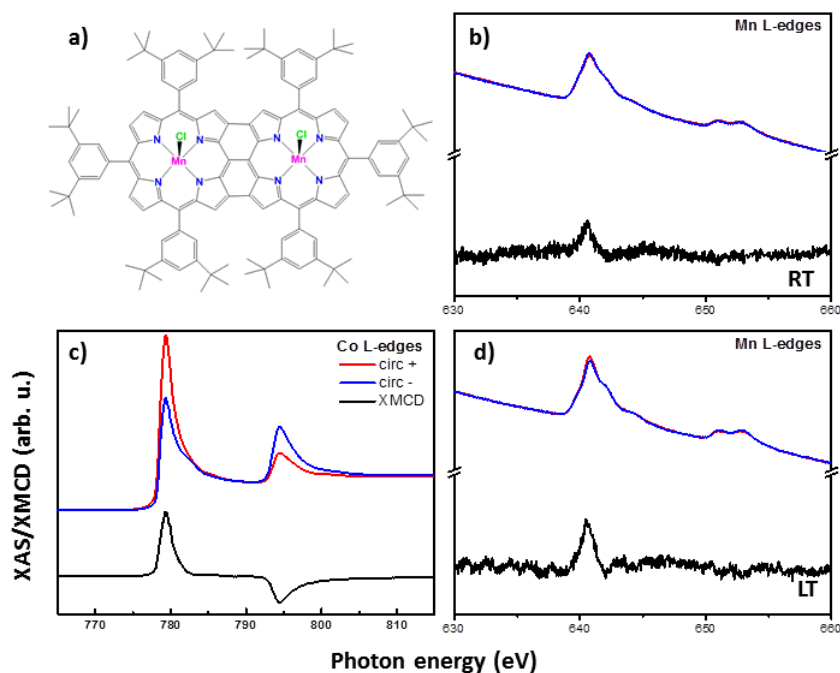


Figure 3.2.5 Molecular structure of the *tbut-tf-MnMnCl₂-P* (a) and Co (c) and Mn (b,d) L-edges XAS/XMCD spectra acquired at room (b,c) and low (~ 20 K) (d) temperature with circularly polarized light in grazing X-ray incidence. Spectra are acquired in remanence after initial magnetization of the sample along the easy magnetization direction

The similarity of XAS/XMCD spectra of the presented Co supported triply-fused porphyrins to the ones of the single FeTPPCL and MnTPPCL porphyrins could be due to the strong interaction with the underlying substrate that dominates over the interactions that could be present in the macrocycle ring. Another, less desirable option is that the macrocycle of the fused dimer breaks into the

subunits of basically single porphyrins due to the annealing in the deposition process that is necessary to desorb the solvent as detailed in Section 3.4.2. To answer this question, that could hinder the perspectives of these molecules to play a role in functional on-surface

architectures, additional experiments are required. Local probe techniques, together with the quantification of the exchange interaction strength through temperature dependent XAS/XMCD measurements could help us to determine whether the molecules are intact or not. In addition, it will be interesting to probe them on different non-magnetic substrates, for example Au(111), Ag(111) or HOPG. Nevertheless, these pilot experiments open up the field of molecular magnetism in that a new class of molecules containing two spin centers has been introduced. Importantly this platform can be modified by chemical means and thus provides a plethora of possibilities for tuning their magnetic properties.

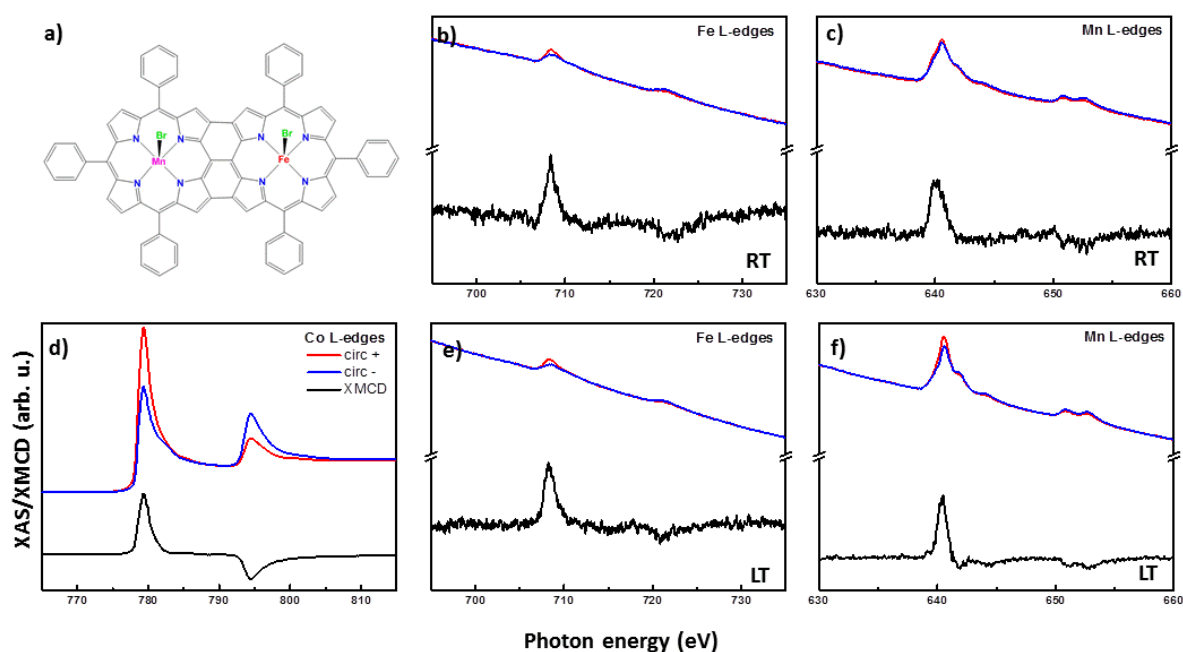


Figure 3.2.6 Molecular structure of the *tf*-MnFeBr₂-P (a) and Co (d), Fe (b,e) and Mn (c,f) L-edges XAS/XMCD spectra acquired at room (b-d) and low (~20 K) (e,f) temperature with circularly polarized light in grazing X-ray incidence. Spectra are acquired in remanence after initial magnetization of the sample along easy magnetization direction

3.2.2 SELF-ASSEMBLY AND MAGNETIC ORDER OF 2D SPIN LATTICES ON SURFACES

In a STM/S study of FePc molecules supported on Au(111) a broadening of the zero-bias feature was observed and ascribed to the possible simultaneous presence of Kondo and RKKY type interactions by Tsukahara et al.⁵² Later on, the same observation was treated as an orbital Kondo effect, as Fe valence fluctuation and as adsorption induced Fe spin switching which all provide physically different albeit possible origins for the experimentally observed phenomenon^{29,126,127}. Inspired by the lack of a conclusive interpretation, we performed combined STM/S and XMCD studies on another phthalocyanine system consisting of the co-assembly of iron fluorinated (FeFPc) and manganese (MnPc) phthalocyanines on Au(111). Here, an extraordinary example of unexpected low-dimensional magnetic structure was observed in the form of long range 2D-ferrimagnetic ordering. The ordering is attributed to the simultaneous presence of Kondo and RKKY type interactions mediated by the surface state electrons of the substrate in a supramolecular 2D Kondo lattice on Au(111)⁵¹. Only these combined STM/S and XMCD experiments on engineered molecular structures provided an unambiguous proof of RKKY ordering. Naturally, after the initial discovery, we wanted to test other binary combinations of the available phthalocyanine molecules in the same manner, both seeking for another system showing this peculiar behavior and at the same time learning more about the prerequisites for the ordering to happen.

In our first step towards the aforementioned investigations we have optimized the procedure for preparation of the alternating coassembly of two phthalocyanine molecules. In the previous investigations, the two molecular species were co-evaporated onto the substrate of choice kept at RT. The evaporation rate of each molecule was tuned independently using a QCM: to investigate the deposition rate for one molecule, the crucible with the other one was kept under a shutter. The quality was then controlled by XPS, looking into the ratios of C1s, N1s and F1s photoelectron peaks that could allow estimation of molecule ratios. If satisfactory samples were obtained, these were used for further investigations, otherwise samples had to be completely re-prepared. This lead to

considerable inefficiency and therefore we have tried an alternative way of preparation where molecules were deposited subsequently. We were guided by the idea that molecules possess sufficient kinetic energy to allow for their intermixing even if they are deposited subsequently. This had the advantage that if the amount/ratio of molecules was not satisfactory, as evidenced from XPS, it could still be corrected leading to higher success rate in sample preparation. The hypothesis was tested on several different samples by means of STM and in all the investigated cases the molecules co-assembled. In Figure 3.2.7 several samples of coassembly consisting of MnPc and FeFPc molecules are shown, while in the Figure 3.2.8, one example of a co-assembly of H₂Pc (metal free) and FeFPc molecules is shown. In the former case (Fig. 3.2.7) the co-assembly is easily visible, while in the latter case (Fig. 3.2.8), due to the bad image quality it becomes apparent/clear only after looking into the defects (pointed by arrow) where FeFPc (protrusions) replaced H₂Pc molecules.

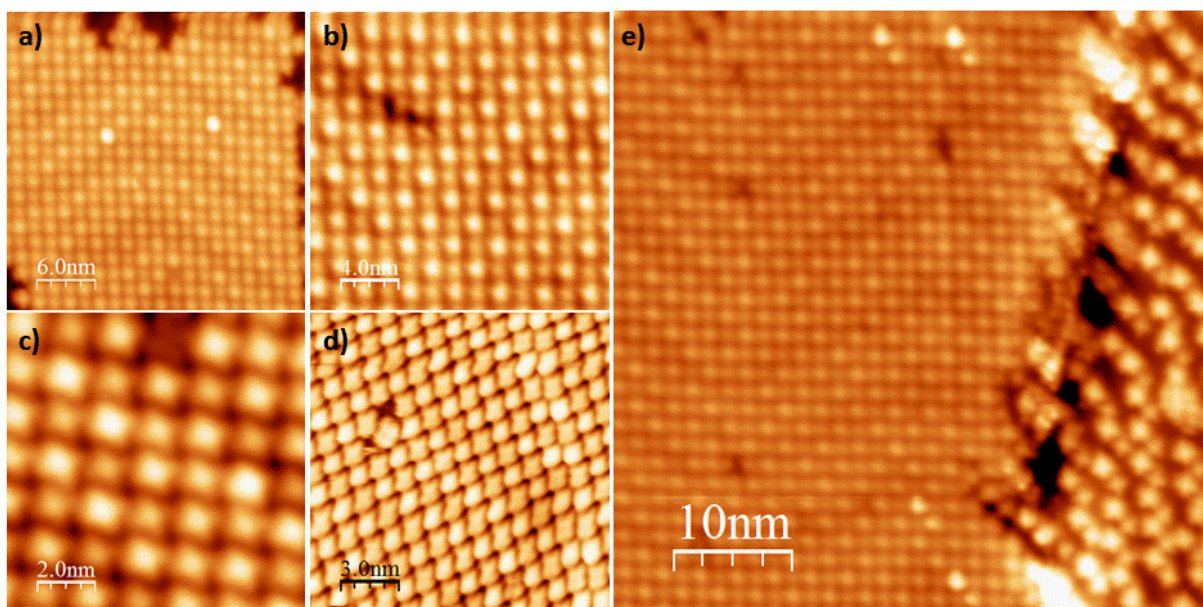


Figure 3.2.7 STM images of different samples where MnPc and FeFPc molecules co-assembled on Au(111) by subsequent deposition. Mn containing molecules are appearing brighter in STM compared to the Fe containing species. Images (a-c,e) were acquired at $T = 4.2$ K, while (d) was acquired at room temperature. Parameters used for the imaging: (a) $I_t = 10$ pA and $U_{bias} = 0.80$ V, (b) $I_t = 5$ pA and $U_{bias} = 0.10$ V, (c) $I_t = 10$ pA and $U_{bias} = 0.80$ V, (d) $I_t = 10$ pA and $U_{bias} = -0.95$ V, (e) $I_t = 5$ pA and $U_{bias} = 0.1$ V

After the procedure was modified and optimized as described, we started examining various surface supported monolayer binary systems of phthalocyanine molecules at our disposal. One of them was always fluorinated to promote coassembling. This includes combinations of FeFPc, CoFPc and CuFPc on one side and CrPc, MnPc, MnPcCl, FePc, CoPc, ZnPc and H₂Pc on the other side. Samples were probed at the X-Treme beamline by means of XAS/XMCD spectroscopy at the temperature of $T = 2.5$ K in both normal and grazing sample geometries (spectra not shown) and the results are summarized in the illustration in Figure 3.2.9a. Out of all investigated systems, only for

the combination of MnPc and FeFPc molecules ordering was observed to be remanent. The reason for this peculiar behavior is most probably the filling of the d-orbitals of the various metallo-phthalocyanines and especially of the d_{z^2} orbital as it has the proper symmetry to interact with the surface state electrons of Au(111). According to the displayed scheme (Figure 3.2.9b) CoPc should also be able to interact in the same way. This is not happening, however, as CoPc is completely quenched due to valence and charge fluctuations when adsorbed on Au(111)²⁷. It seems that we were really lucky that the very first system we investigated was the one that was suitable for long-range ordering. This knowledge can on the other hand help us in future design of the experiments and/or the devices that would require possibility to interact with the substrate.

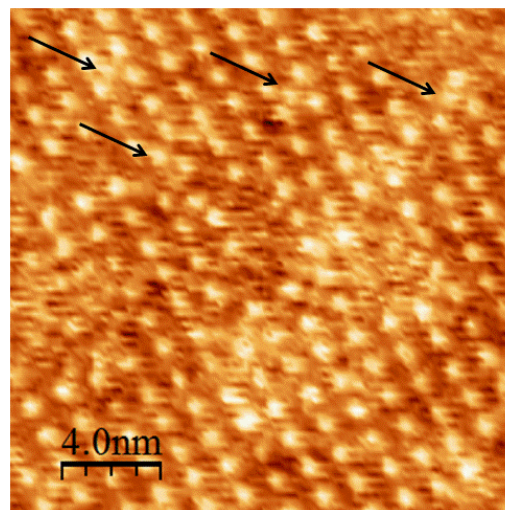


Figure 3.2.8 20 nm x 20 nm STM image of a sample where H₂Pc and FeFPc molecules co-assembled on Au(111) after their subsequent deposition. Arrows are pointing at the defects where FeFPc replaced H₂Pc molecules. Image has been acquired at room temperature with $I_t = 10$ pA and $U_{bias} = -0.80$ V

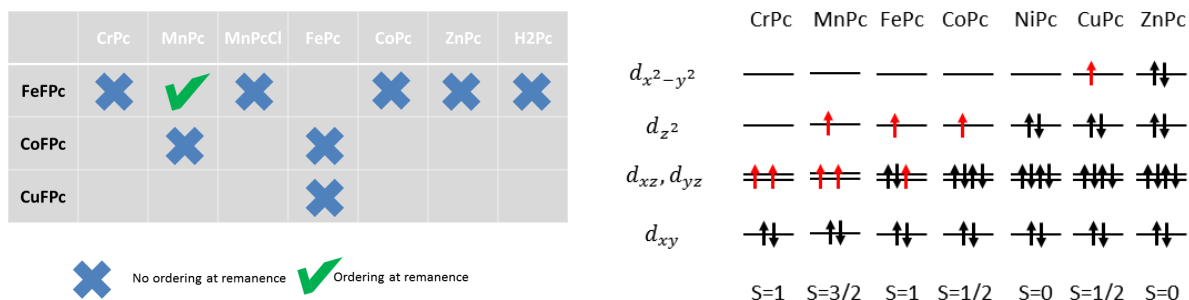


Figure 3.2.9 Tabular representation of the investigated binary phthalocyanine systems coassembled on Au(111) - (left) and filling of the d-orbitals of free phthalocyanine molecules (right). Red arrows represent unpaired electrons, while the black ones represent paired ones. Below is the spin state according to the number of unpaired electrons. Adapted from¹²⁸ by expanding to case of CrPc and ZnPc. Note that the electronic configuration of the center metal atoms in Porphyrins and Phthalocyanines can change as these molecules are adsorbed on surface.

In the last part of this chapter about the 2D co-assembly of a binary checkerboard pattern on non-magnetic Au(111), we wanted to see if and what kind of changes the formation of the 2D-Kondo lattice and the ferrimagnetic ordering would induce in the surface states of the Au(111) substrate. In particular we were interested in looking at the shape of the Fermi surface in proximity to the interface and the cuts along the k_x , k_y direction by means of Angle Resolved Photoelectron Spectroscopy (ARPES). The samples were prepared at the Surface Science Lab and transferred to the SIS beamline of the SLS in a slightly modified vacuum suitcase to accommodate special sample holders that can be used at the aforementioned beamline. Upon cooling down the samples to 10-15 K (this provides the lowest reachable temperature at the SIS beamline) the samples were aligned to adjust the position of the Γ -point to the center of the scan and energy-momentum dispersion is recorded using circularly polarized light with $E = 76$ eV in a sweeping mode (from -0.7 to 0.2 eV). We started the experiment from a clean Au(111) serving as a reference (Figure 3.2.10a) where standard dispersion with minima at -0.45 ± 0.05 eV is observed^{129,130} but we were not able to resolve the Rashba splitting of the surface state. Next, we investigated a purely organic molecular system consisting of metal-free phthalocyanine (H₂Pc) self-assembled on single-crystalline Au(111) substrates (Figure 3.2.10b). The surface state of the Au(111) substrate is, similar to other cases when π -conjugated systems were adsorbed on substrates

with promoted surface states^{131–138}, shifted towards the Fermi level, in this case by 0.10 eV. Further on, we have introduced one of the metal centers by preparing a coassembly of FeFPc and H₂Pc on Au(111). Here, the surface state shifts back down by 0.05 eV (Figure 3.2.10c) and stays at this energy even if the metal free phthalocyanine is replaced by MnPc (Figure 3.2.10d). This is a bit surprising, but could happen if the metal atoms are supplying some charge to the substrate due to their strong interaction with it¹³⁹. Unfortunately, except the shifts in the surface state we didn't observe any other effects, most probably due to the limited range of temperature that can be sampled at this beamline (> 10K, this is a considerably high limited in view of the Kondo peak in our STS studies (*vide infra*) disappearing above 8-10K). It is still important to keep these surface state shifts in mind as we model the system or for planning the future experiments.

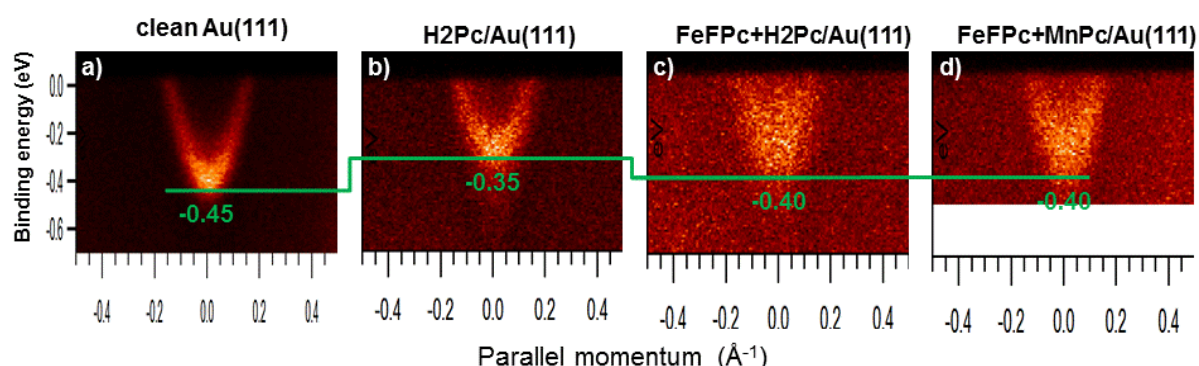


Figure 3.2.10 Energy vs parallel momentum dispersions of the Au(111) surface states on (a) clean Au(111), (b) monolayer of H₂Pc on Au(111), (c) monolayer of FeFPc and H₂Pc molecules coassembled on Au(111) and (d) monolayer of FeFPc and MnPc molecules coassembled on Au(111)

3.2.3 VERTICAL REORGANIZATION OF MOLECULAR BI- AND MULTI-LAYERS DUE TO MOLECULE-SUBSTRATE INTERACTIONS

Porphyrin and phthalocyanine molecules due to their extraordinary properties are used or envisaged for application in many photovoltaic^{140–143}, molecular electronic¹⁴⁴ and spintronic^{145–149} devices. In the effervescent field of molecular spintronics, this includes integrating them in magnetic tunnel junctions (MTJs) or similar spinterface devices, where molecules are localized between contact electrodes. Often such devices exhibit layered structures where stability of each layer is important for efficiency and durability of such devices. Migration processes during or after fabrication of device active layers provide a challenge for the design, the fabrication and the operation, also of spintronic devices. In the semiconductor technology, this is well known and extensively studied^{150,151}. It is of utmost importance to investigate such devices or model systems at elevated temperatures to emulate real working conditions as these reveal insight into the subtle interplay of molecule-substrate interactions. These mixing effects are well studied in 2D on-surface molecular systems^{152–154}, however only several examples exist addressing the 3D case^{120,155–159}. Here, we will report on the investigation of the vertical reorganization of phthalocyanine molecules in bi- but also multilayered systems by means of XAS/XMCD spectroscopy.

In light of recent discoveries of ordering in multilayered systems of phthalocyanine molecules¹⁴⁹, we wanted to investigate a heteromolecular bilayer of MnPc molecules deposited on FePc molecules that were supported on

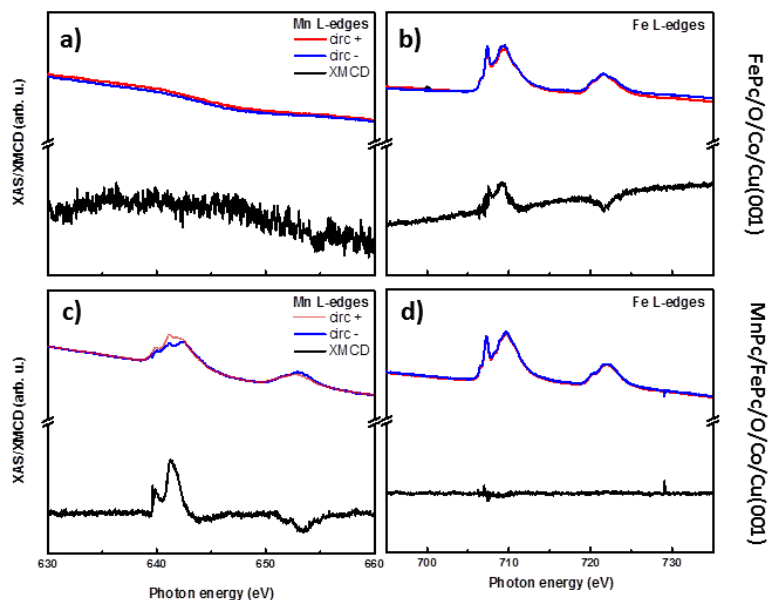


Figure 3.2.11 Mn and Fe XAS/XMCD L-edges measured at RT in grazing incidence on only FePc and MnPc “covered” FePc layer supported on O/Co substrate

oxygen terminated Co film (MnPc/FePc/O/Co system). We have first deposited a full layer of FePc molecules on O/Co substrate and measured both Mn and Fe XAS/XMCD spectra at room temperature. The measurements were performed in remanence upon initial magnetization of the film along the easy magnetization direction, in particular in the grazing direction of X-ray incidence. As it was expected, Fe XAS shows a certain XMCD signal that is AFM oriented to the one of the underlying substrate (not shown) while in the Mn region just background signal is visible (Figure 3.2.11a, b). In the next step, we have deposited ~ 1 ML of MnPc molecules on top of a full layer of FePc molecules and repeated the measurements. Surprisingly, we could see very strong exchange induced XMCD signal on Mn, while one of Fe almost completely disappeared (Figure 3.2.11c, d). This suggests, due to very short range of action of exchange interactions, that the molecules interchanged their positions in the top and/or bottom layer. Although MnPc was deposited second, it is now in contact with the substrate. The molecules are evaporated from the crucible kept at around 500K, so they possess high kinetic energy and upon impact on substrate this energy needs to be dissipated, such that a certain level of mixing would be expected. Therefore we have performed the experiment in reverse order, having full layer of MnPc deposited first and then deposited FePc on top of it. Now, no XMCD at all was visible on Fe, while Mn again showed very intense XMCD signal (Figure 3.2.12a, b). This was again surprising in because no mixing of the molecules occurred, suggesting a discrepancy between the interaction energies of the two molecules with the substrate.

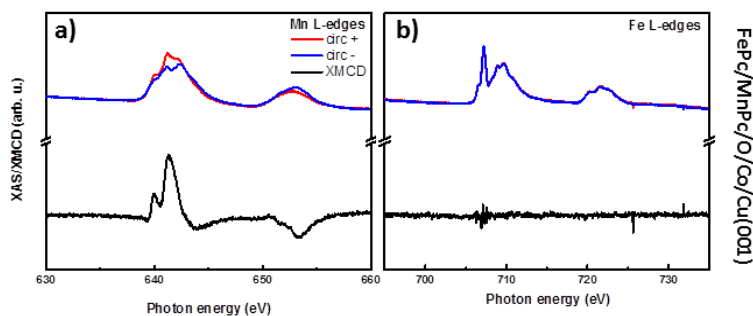


Figure 3.2.12 Mn and Fe XAS/XMCD L-edges measured at RT in grazing incidence on FePc covered MnPc layer supported on O/Co substrate

In order to check whether this discrepancy could be due to differences in magnetic interactions with the substrate, we have performed additional experiments where MnPc and FePc molecules were deposited on a full layer of non-magnetic ZnPc molecules. Like in the previous example, we have performed this experiment also in reversed order, where ZnPc molecules were deposited on compact layers of MnPc and FePc molecules. The acquired RT Mn

and Fe XAS/XMCD spectra are showed in Figure 3.2.13, where clear XMCD signals of Mn are visible regardless of deposition sequence, while almost no signal was visible for Fe in both cases. From the beginning it was not expected that magnetic interaction would play a pivotal role in the reported interlayer exchange as it accounts for only small fraction of total molecular adsorption energy as a measure of interaction with the substrate. These experiments exclude this possibility completely and hint on different decisive interaction as a driving force. Keeping in mind which molecules are found close to the surface, it can be concluded that $E_{\text{ads}}(\text{MnPc}) < E_{\text{ads}}(\text{ZnPc}) < E_{\text{ads}}(\text{FePc})$. In addition, since the molecules are of the same type and adsorption sites are identical, the differences are most probably dominated by the different interaction of the metal ions in the Pc macrocycles with the substrate.

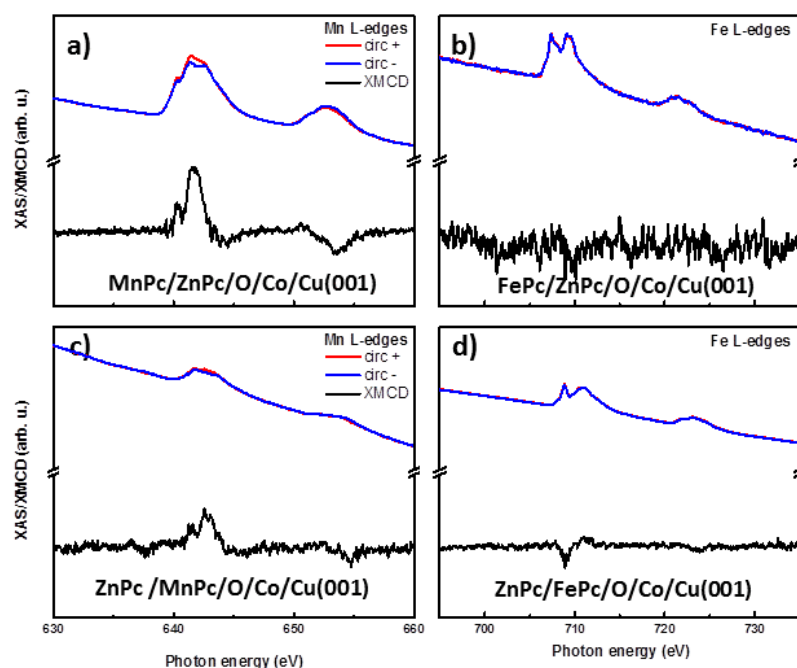


Figure 3.2.13 Mn and Fe XAS/XMCD L-edges measured at RT in grazing incidence on heteromolecular bilayers consisting of ZnPc and Mn/FePc molecules supported on O/Co substrate where ZnPc was deposited first (a,b) or second (c,d)

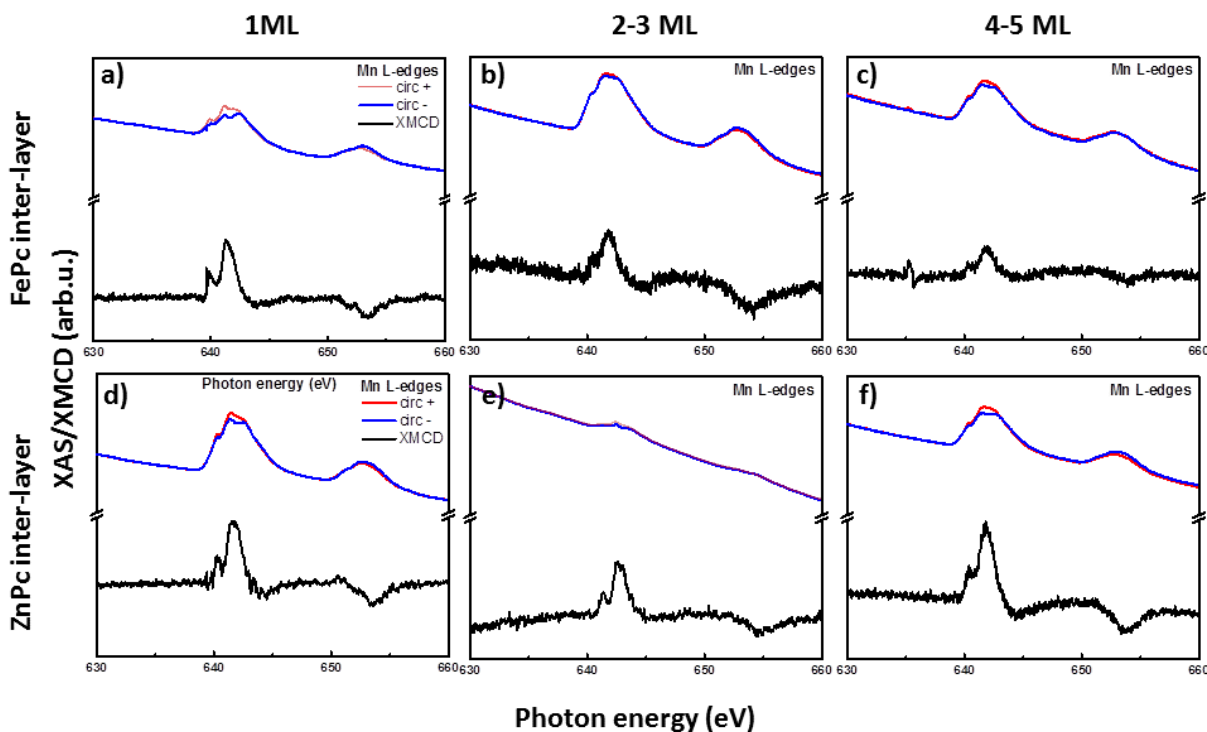


Figure 3.2.14 Mn XAS/XMCD L-edges measured at RT in grazing incidence on heteromolecular bi- and multilayers where MnPc molecules were deposited on FePc (a-c) or ZnPc (d-f) molecular films of increasing thickness supported on O/Co substrate

In the next step we wanted to glimpse into the mechanism of the molecular exchange so we have deposited MnPc molecules on FePc or ZnPc molecular films of increasing thickness (up to 5 ML thick) that were supported on O/Co substrate. Two mechanisms of the exchange seemed possible, diffusive molecular exchange facilitated by the initially high kinetic energy of the molecules in the precipitation process or metal exchange at the surface where the activation barrier is also overcome by the initially high kinetic energy of the precipitates. If the thickness of the spacer (inter)layer is then increased, more kinetic energy would be dissipated for molecules in the second deposition cycle migrating through this spacer layer. The idea was thus to see whether the increasing thickness of inter-layer molecules would progressively hinder molecular exchange. The results are shown in Figure 3.2.14 demonstrating that even at the thickness of 5ML of spacer molecules, exchange still takes place, although the Mn XMCD signal is reduced. This favors the first diffusive mechanism or indicates that the thickness was not sufficient to anticipate the energy which is unlikely. For a better understanding, treatment within a DFT+U and/or MonteCarlo framework is required to estimate barriers for the aforementioned processes.

In the last step, we wanted to investigate the influence of elevated temperatures to the mixing of the molecules. For that purpose, two samples with MnPc deposited on FePc and ZnPc molecular layers were prepared and characterized before (Figure 3.2.15a,c) and upon (Figure 3.2.15b,d) annealing to $T = 450\text{K}$ for 30 minutes. This temperature was selected as it lies below the

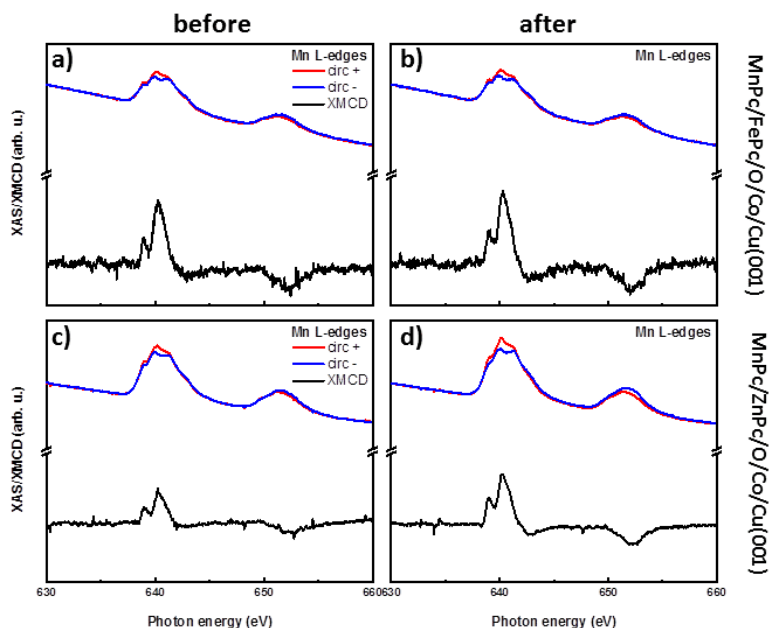


Figure 3.2.15 Mn XAS/XMCD L-edges measured at RT in grazing incidence on MnPc “covered” Zn/FePc molecular layers supported on O/Co substrate before (a,b) and after (c,d) thermal annealing

temperature at which desorption of second layer is reported^{158,159}. In both cases, it was detected that providing thermal energy to the system increased the number of MnPc molecules that got in contact with the substrate, as the XMCD signal increased by $\sim 20\%$ (normalized to XAS to exclude possible variations in the amount of molecules) in both cases. In a simplified picture, it seems that all MnPc molecules that reach the surface are anchored there due to a strong interaction with the substrate. The origin of such a strong interaction is at this point unclear. On the other hand it is known that phthalocyanine molecules are adsorbing on top of Oxygen atoms from the substrate³⁹ and it could be caused by some specific electronic effect such as chemical bonding and/or charge transfer due to a proper symmetry of the Mn orbitals with respect to oxygen ones. The phenomenon of mixing molecular layers was reported before^{158,159}, however this big asymmetry is not usual and needs to be taken into account for on-surface metalation reactions or when spintronic devices are designed as MnPc molecules can serve as passivation layer. We hope that aforementioned theoretical treatments would provide us with deeper insight into the involved interactions and help better understand the origin of this interesting mixing phenomenon.

3.3 TUNING OF THE MAGNETIC INTERACTIONS

Gaining control of or modifying the properties of on-surface architectures is of equally high importance in the prospect of using 2D metal-organic assemblies in spintronic devices. At this point, it became clear that magnetic interactions and properties of species on surfaces depend on several parameters – the distance to and the electronic structure of the spin-bearing center, the pathway of interaction as well as the presence of mediators of interactions. This level of understanding allowed numerous ways of tuning magnetic properties and interactions of molecules on surfaces.

3.3.1 SPIN MANIPULATIONS OF METAL-CONTAINING PHTHALOCYANINE MOLECULES BY H_2/H^* LIGATION

One of the possible ways for tuning the magnetic properties of molecules on surfaces, very much exploited in the world of molecular magnetism is the application of external chemical stimuli^{21,36–44}. The stimuli can influence magnetic properties in two ways – it can directly alter the electronic structure of the spin active center or it can induce structural changes and displacements of the spin active center thus changing symmetries and ligand field around it. In most of the reported studies, highly toxic chemical stimuli such as CO, NO or NH_3 are used^{38,39,41,160,161} while in some other STM/S studies, atomic hydrogen (H^*) was the choice^{36,37,162}. In the case when H^* was used, it was demonstrated that it can be adsorbed to metal center, but also on two periphery N atoms of phthalocyanine molecules^{37,162}. In case it was attached to the periphery atoms, molecules were slightly bending upward thus reducing interaction with the substrate as evidenced by the increased mobility of these molecules on the substrate. In one particular study, it was discussed that dosing large dose of molecular hydrogen (H_2) would lead to ligation with a single H atom due to partial dissociation of H_2 on Au(111). If a compressed layer of molecules was present on the substrate it will be constrained to ligating only to the metal center³⁷. This, together with the lack of spectroscopic, in particular XAS/XMCD characterization of the induced changes upon exposure to hydrogen, motivated us to perform several experiments with hydrogen

exposures. For this, we planned to use compressed layers of phthalocyanine molecules supported on Au(111) and expose them first to molecular (H_2) and later to the atomic (H^*) hydrogen created by cracking the molecular one with a hot filament. Like this, we could probe two separate regimes of influence of hydrogen ligation; first influence only on the metal center, and later also collective influence to the whole molecule and molecule-substrate interactions.

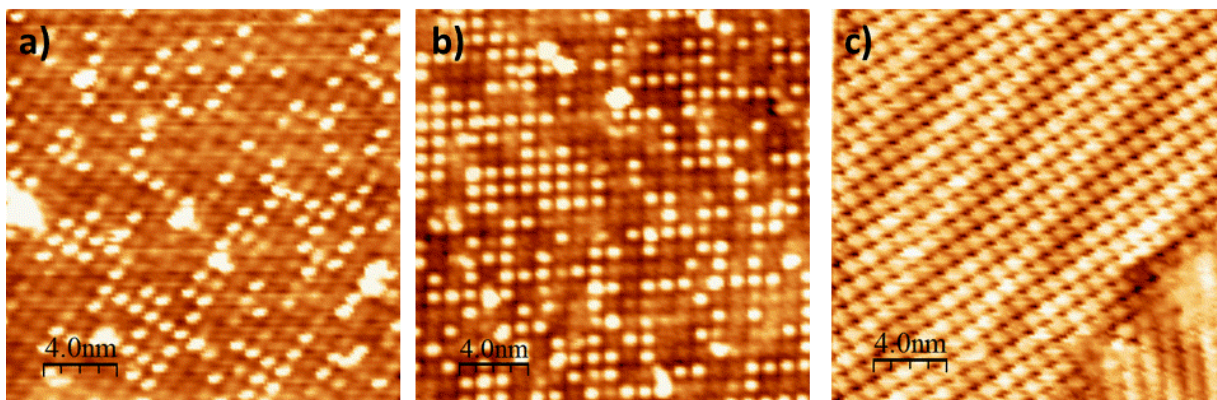


Figure 3.2.16 STM images (20 nm x 20 nm) of ~1ML of CrPc molecules self-assembled on Au(111) substrate upon exposure to 30000 L of molecular hydrogen H_2 at room temperature (a), where at ~30% of molecules hydrogen (protrusion) is observed and (b) subsequent 30000 L exposure, where at ~50% of molecules hydrogen (protrusion) is observed. (c) shows the same sample after successful annealing to 400K in order to desorb the hydrogen molecules as evidenced from absence of the protrusions in the center of molecules. All images are recorded at $T=100K$ with $U_{bias}=-1.2V$ and $I_{set}=10pA$ on the same sample and hydrogen coverage is estimated as an average from at least 4 different images

First step before performing the XAS/XMCD experiments was optimization of the dosing process. Therefore we have first exposed full layer of CrPc molecules on Au(111) at room temperature to a different dose of molecular hydrogen. Upon exposure to ~30000 L, around 30% of the molecules are observed as a protrusion that we ascribe to the ligated molecules (Figure 3.2.16a) while upon increase of the dose to 60000 L it increases to around 50% (Figure 3.2.16b). Annealing of this sample to $T = 400 K$ led to complete desorption of the H_2 from the sample (Figure 3.2.16c). The protrusions we observed are not really observed in other STM studies of phthalocyanine molecules – on the contrary, usually the depression was observed upon ligation with hydrogen^{36,37,162}. Since CrPc was a new molecule, and lacking reference data, we repeated the experiment but now with MnPc on Au(111) that was

extensively studied. Surprisingly, very similar protrusions are observed also on the MnPc, in addition to the hydrogen that was adsorbed between the molecules (Figure 3.2.17).

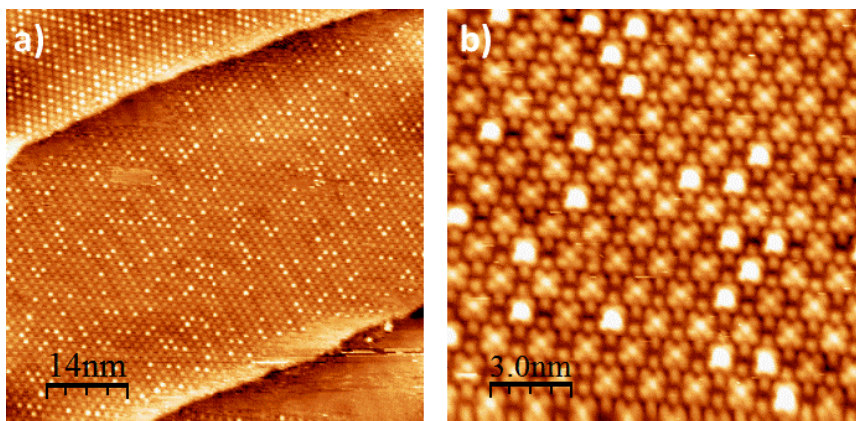


Figure 3.2.17 75 nm x 75 nm (a) and 15 nm x 15 nm (b) STM images of ~1ML of MnPc molecules self-assembled on Au(111) substrate upon exposure to 60000 L of molecular hydrogen H_2 at room temperature, where at ~25% of molecules hydrogen (protrusion) is observed. Images are acquired at room temperature with the following parameters: $U_{bias} = -1.25$ V and $I_{set} = 20$ pA

Both results of dosing hydrogen on CrPc and MnPc are showing big protrusions

(around 1 Å above the molecules) instead of the expected depression according to the previous studies of MnPc/Au(111). It could be that in our case molecular hydrogen is attached to the molecules instead as there are some examples of H_2 ligating to Fe, Cr, W complexes^{163–165}. However from the presented data it is not possible to undoubtedly conclude it. Interestingly, Figure 3.2.17b) also shows hydrogen adsorbed on the Au(111) surface thus completely changing the assembly pattern of the MnPc molecules. Next, we have dosed atomic hydrogen on a full layer of CrPc molecules on Au(111) by applying the same dose of hydrogen gas but while running a hot filament in the sample vicinity. As expected, a disordered molecular layer has been formed due to reduced interaction with the substrate. This is a consequence of hydrogen binding to the lateral nitrogen atoms (Figure 3.2.18). Unfortunately, in this case we couldn't reverse the effects caused by H^* dosing up to the temperatures where molecules desorbed or polymerized on the surface. In spite of the uncertainty whether atomic or molecular hydrogen is adsorbed in the first mentioned case, the effects of dosing are completely different in the two dosing scenarios; therefore we will refer to the first case as a molecular hydrogen and to the second case as atomic hydrogen dosing in the following part reporting on the XAS/XMCD investigations. This terminology will

be further used in spite of the caveat that in the first case H_2 could still split at the substrate and produce limited amount of H^* due to the inefficiency of that process. The H^* could then preferentially ligate only to the molecule's metal center (this is however not supported

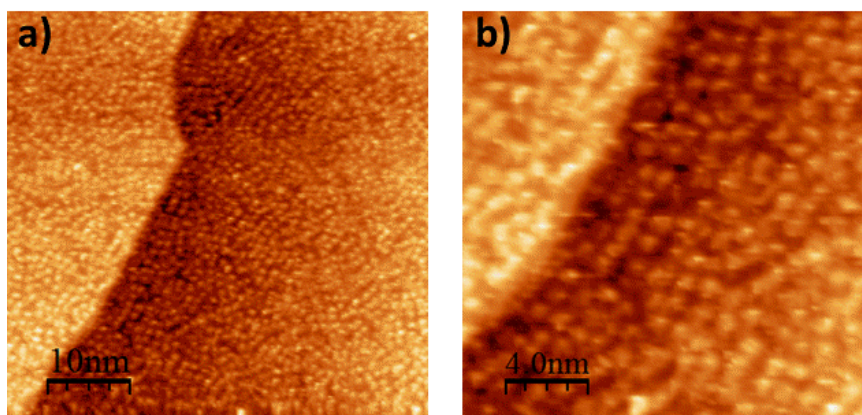


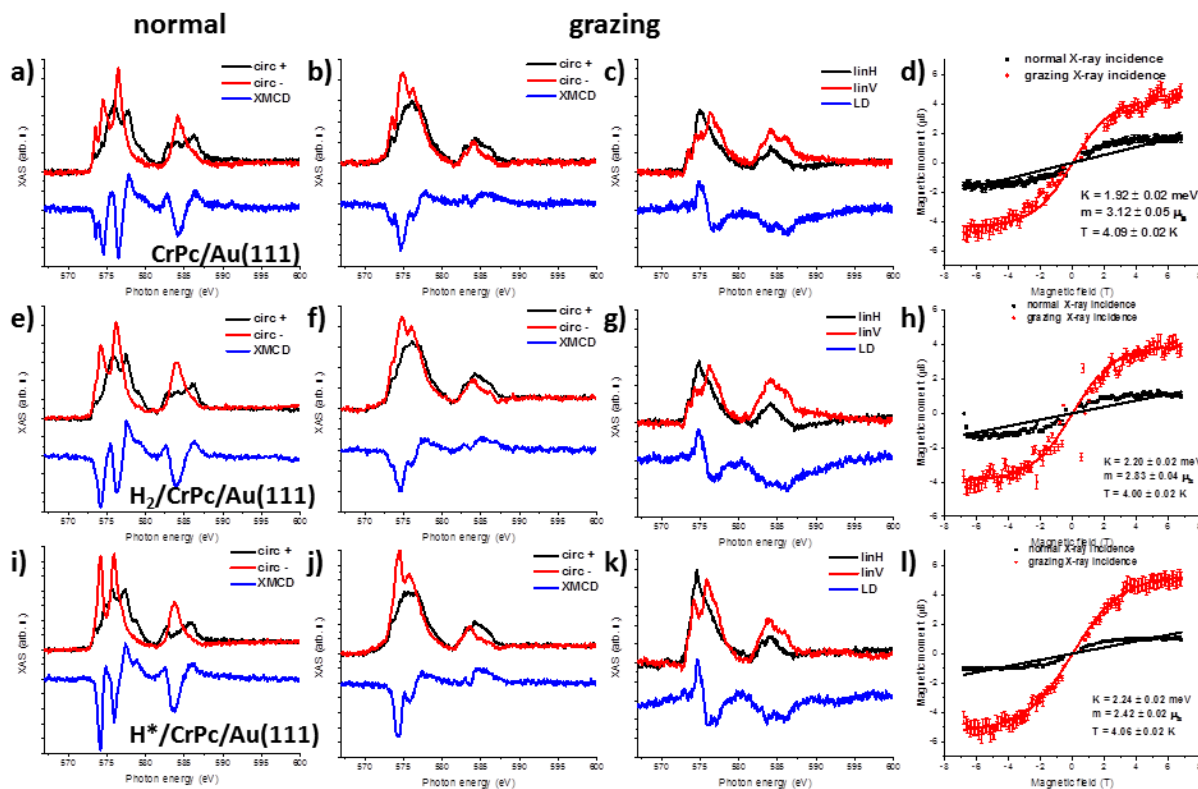
Figure 3.2.18 STM images (50 nm x 50 nm - (a) and 20 nm x 20 nm - (b) of ~ 1 ML of CrPc molecules assembled on Au(111) substrate upon exposure to atomic hydrogen H^* created by exposure to 60000 L of molecular hydrogen next to a hot filament while sample is kept at room temperature. Figures (b,c) show that dosing of atomic hydrogen destroyed ordering of molecular layer, with some local ordering still present. The images are recorded at $T=100$ K with $I_{set}=10$ pA and $U_{bias}=-0.6$ V

by the different appearance of MnPc in the current and previous STM studies).

Once we have established the two dosing regimens of molecular and atomic hydrogen, we started investigating the effects they have on magnetic properties of phthalocyanine molecules supported on Au(111). Several samples were investigated by means of XMCD spectroscopy at the X-Treme beamline of the SLS. This beamline was chosen due to the high magnetic field (up to 7 T) and very low temperatures (down to ~ 2.5 K) reachable there. Samples were prepared and characterized in the Surface Science lab and transferred to the beamline, as it has been previously described. At the beamline, upon cooling down to ~ 2.5 K, samples were probed by both linearly and circularly polarized X-rays in normal and grazing sample geometries. Additionally, where appropriate, magnetization curves were acquired. After characterization of the samples, they were first exposed to the dose of 60000 L of molecular hydrogen, and the complete measurement sequence was repeated. Then samples were annealed to $T = 400$ K to desorb the molecular hydrogen and exposed to atomic hydrogen as previously described and the corresponding measurements were repeated.

CrPc/Au(111) was chosen as the first system to be investigated according to the described procedure. The acquired spectra together with the magnetization curves are shown in Figure

3.2.19. In both XAS and XMCD spectra acquired in normal and grazing incidence, slight changes are observable upon molecular hydrogen dosing (Figure 3.2.19e,f). The most pronounced changes with regard to the bare CrPc/Au(111) spectrum appear at the lower energy end of the



Figures 3.2.19 Cr L-edges XAS/XMCD/LD spectra of 1 ML CrPc on Au(111) acquired in normal (first column) and grazing (next two columns) sample geometries and magnetization curves (black-normal, red-grazing) acquired at 2.5 K before (first row) and after molecular (second row) or atomic hydrogen (third row) exposure. The spectra in the third column are acquired with linearly polarized light while all the others were acquired with circularly polarized light. The XAS/XMCD spectra in the first two columns are acquired with an applied field of 6.8 T, the XAS/LD spectra in the third column with an applied field of 0.05 T while magnetization curves are acquired by sweeping the field from -6.8 T to 6.8 T

spectra (574.6 eV). The changes become more apparent after atomic Hydrogen has been dosed (Figure 3.2.19i,j). At this lower side of the XAS spectra, usually the transitions involving the d_{z^2} orbital are appearing. This association is also supported by the strong angular dependence of the absorption visible in the spectra acquired with linear light⁸ (Figure 3.2.19d,h,l). This

⁸ In a sample orientation used at the X-Treme beamline, horizontally polarized linear light serves as a selective probe for out-of-plane oriented orbitals, while vertically polarized light probes in-plane orbitals

means that mostly the d_{z^2} orbital is influenced by H_2/H^* dosing, which is in accordance with the STM data showing axial ligation of the hydrogen. In order to quantify to what extent the magnetic properties are influenced, we have first performed the sum rules analysis, and then fitted the obtained magnetization curves. The results are summarized in the Table 3.4.

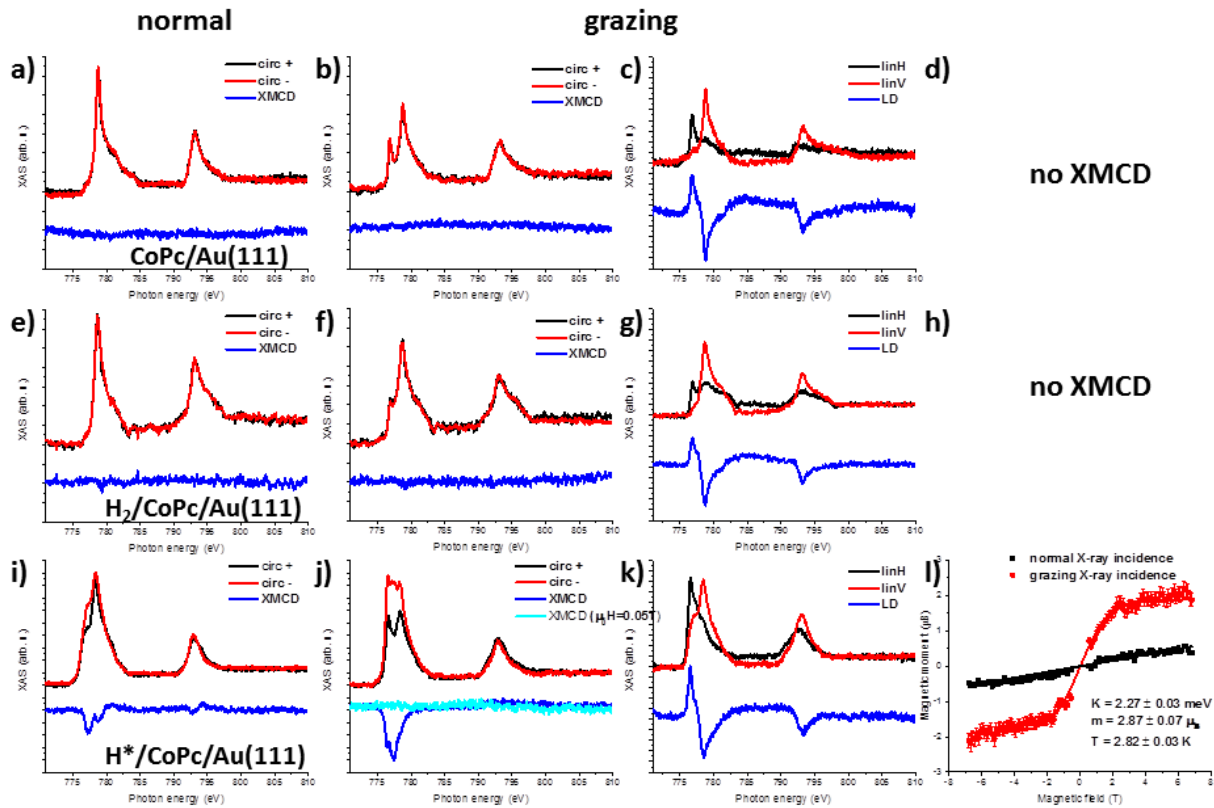
Table 3.4 Obtained orbital (m_L) and effective spin (m_{SE}) magnetic moments of Cr from sum rules analysis together with total moments (m) and the MAE (K) from magnetization curves fitting

	CrPc/Au(111)		H_2 /CrPc/Au(111)		H^* /CrPc/Au(111)	
	normal	grazing	normal	grazing	normal	grazing
$m_{se} [\mu_B]$	1.5 ± 0.2	4.5 ± 0.7	0.4 ± 0.2	4.0 ± 0.7	0.8 ± 0.2	5.0 ± 0.7
$m_L [\mu_B]$	-0.02 ± 0.01	0.20 ± 0.03	0.25 ± 0.03	0.20 ± 0.05	0.17 ± 0.03	0.15 ± 0.05
$m [\mu_B]$	3.12 ± 0.05		2.83 ± 0.04		2.42 ± 0.02	
$K [meV]$	1.92 ± 0.02		2.20 ± 0.02		2.24 ± 0.02	

The obtained results are indicating towards a significant decrease of the effective spin moment with a simultaneous increase of the orbital moment of Cr in normal incidence and increase of the MAE upon exposure to molecular or atomic hydrogen that is more pronounced in the former case. The decrease of the effective spin moment in the normal incidence case can be understood by hydrogen induced charge redistribution from the previously occupied d_{z^2} orbital to the degenerate d_{π} orbitals leading to an increase of the orbital magnetic moment and anisotropy. This redistribution occurs as the d_{z^2} orbital is lifted in energy due to the presence of a ligand along z-direction. In addition, this ligation is also expected to weaken the interaction with the substrate due to energy discrepancy. Although this descriptive interpretation seems to fit well with the observed effects, for more precise interpretation DFT+U, especially looking into the charge density distribution can be of great importance.

In the next experiment, we wanted to test the proposed model on another interesting system, CoPc/Au(111). On this substrate, the spin of the Co atom from the molecules is quenched due to the strong valence and charge fluctuations²⁷. Nevertheless, there were studies where the modification (dehydrogenation) of the molecules by the STM tip changed the molecule-substrate interaction which re-induced the magnetic moment, as evidenced by the presence

of the Kondo effect³¹. Therefore we wanted to check if a similar effect could be induced by hydrogen ligation.



Figures 3.2.20 Co L-edges XAS/XMCD/LD spectra of 1 ML CoPc on Au(111) acquired in normal (first column) and grazing (next two columns) sample geometries and magnetization curves (black-normal, red-grazing) acquired at 2.5 K before (first row) and after molecular (second row) or atomic hydrogen (third row) exposure. Spectra in the third column are acquired with linearly polarized light while all the others were acquired with circularly polarized light. The XAS/XMCD spectra in the first two columns are acquired with an applied field of 6.8 T, XAS/LD; the spectra in the third column with an applied field of 0.05 T while the magnetization curves are acquired by sweeping the field from -6.8 T to 6.8 T

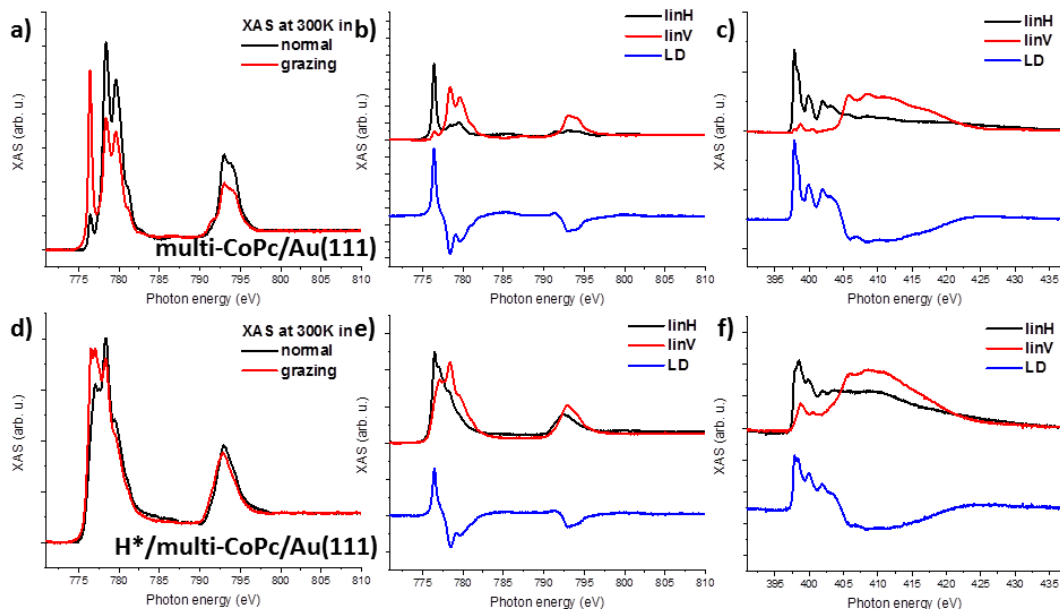
The samples were characterized before (Figure 3.2.20a-d) and after exposure to molecular (Figure 3.2.20e-h) and atomic (Figure 3.2.20i-l) hydrogen. This characterization was performed similarly to the previous case. After the molecular hydrogen exposure, very subtle changes in XAS are observed both in normal and grazing incidence. Again the changes are mostly located at the lower end of the absorption edge (Figure 3.2.20e-h). No XMCD signal is observed, however, at this moment. Exposure of the sample to atomic hydrogen on the other hand induced significant changes to the XAS. In particular a magnetic dichroism

(XMCD signal) with in-plane anisotropy appeared for the H* exposed molecule in applied field. The XAS shifted to lower energy, suggesting a Co²⁺ oxidation state and was broadened due to additional orbitals involved in the X-ray absorption. Sum rules analysis and magnetization curve fitting results are summarized in the Table 3.5. The analysis reveals very strong orbital moments and an anisotropy that is comparable to the one observed for CrPc, which is a bit surprising for CoPc at first. In principle, the strong anisotropy may be explained by a transfer of an electron (or partial charge redistribution) from d_{π} orbitals to the $d_{x^2-y^2}$ or even more likely to the d_{z^2} orbital that would become close in energy if the symmetry of the molecule changed. This is possible upon exposure to atomic hydrogen as it has been reported to attach to the two peripheral N atoms of phthalocyanine molecules^{37,162}.

Table 3.5 Orbital (m_L) and effective spin (m_{SE}) magnetic moments of Co obtained from sum rules analysis together with the total moments (m) and MAE (K) from magnetization curves fitting

	normal	grazing
$m_{se} [\mu_B]$	0.5 ± 0.2	1.6 ± 0.3
$m_L [\mu_B]$	0.08 ± 0.01	0.49 ± 0.04
$m [\mu_B]$	2.87 ± 0.07	
$K [\text{meV}]$	2.27 ± 0.03	

To elucidate the possibility of H reacting with peripheral N atoms, and to investigate the influence of substrate vicinity on the adsorption, we have deposited a multilayer of CoPc molecules on Au(111) and probed it at room temperature before (Figure 3.2.21a-c) and upon exposure to atomic hydrogen exposure (Figure 3.2.21d-f). By the comparison of Co XAS spectra acquired with linearly and circularly polarized X-rays we can identify similar features for the multilayer and monolayer covered sample. These results indicate that the change of the spin state is not only due to the change of the interaction with substrate but also due to charge reorganization in the CoPc molecules. Changes observed in the N K-edge spectra upon hydrogen dosing demonstrate that the modified spin state may indeed be a consequence of a symmetry change due to attachment of two hydrogen atoms to the two periphery N atoms.



Figures 3.2.21 Co L-edges XAS/XMCD/LD spectra acquired on a multilayer of CoPc molecules on Au(111) in normal and grazing sample geometries at room temperature before (first row) and after exposure to atomic hydrogen (second row). Spectra in first column are acquired with circularly polarized light while all the other spectra were acquired with linearly polarized light. All spectra have been acquired with an applied field of 0.05 T

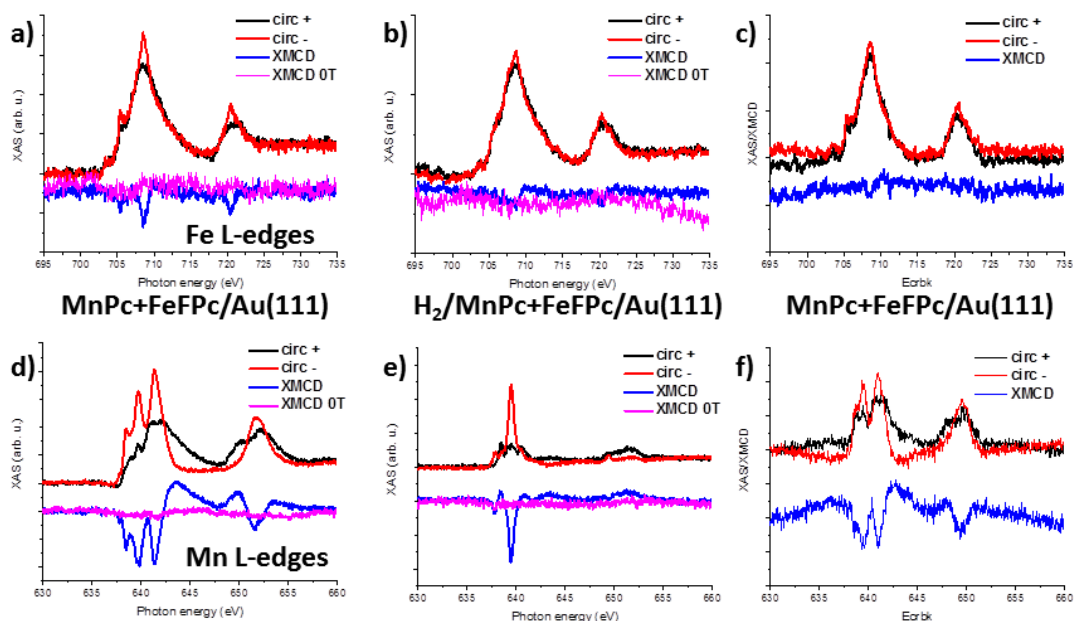


Figure 3.2.22 Mn (a-c) and Fe (d-e) L-edges XAS and XMCD spectra acquired in normal sample geometry of an alternating spin array of MnPc and FeFPc molecules coassembled on Au(111). Spectra are acquired at 2.5 K and 6.8 T before (a,d) after exposure to molecular H₂ (b,e). Spectra in c), f) are recorded after annealing of exposed sample to T = 400 K in order to desorb H₂.

Investigation of the previous systems helped us to gain a certain level of understanding of mechanisms involved in spin modifications of single molecular species supported on Au(111) upon exposure to molecular or atomic hydrogen. However, we also wanted to examine how the modifications of spins in individual molecules would affect complex magnetic structures such as 2D ferrimagnet consisting of MnPc and FeFPc molecules coassembled in a checkerboard array. Here, the interactions with the substrate are very important, and modification of them could lead to the destruction of the previously observed ordering. If the stimuli can be afterwards desorbed, it would represent an interesting tool for reversible switching of the ferrimagnetic ordering.

We have prepared samples consisting of the aforementioned molecules and probed them by means of XAS/XMCD spectroscopy in normal X-ray incidence at the temperature of 2.5 K. Only normal incidence is discussed here as that was the direction where remanence was observed. After the initial characterization and confirmation that there is a remanence (Figure 3.2.22a,d), the sample was exposed to molecular hydrogen and the spectra shown in Figure 3.2.22b,e) have been measured. Upon the molecular hydrogen exposure, the Fe XAS changes slightly, while there is significant decrease of the observable Fe XMCD. Such behavior is most probably induced by lifting of the d_{z^2} orbital in energy and spillover of the electron from this orbital to the degenerate d_{π} orbitals where they are getting paired to the second unpaired electron of Fe metal. The Mn XAS and XMCD, on the other hand, completely changed upon the exposure with an extremely high peak appearing slightly below 640 eV (Figure 3.2.22d). Such a behavior has not been observed for any other phthalocyanine molecules investigated here. In addition, there was no XMCD observed in the remanence for neither Fe nor Mn, providing evidence that the ferrimagnetic ordering is destroyed. Applying sum rules analysis revealed that Mn is observed in its high spin state, with $S = 5/2$ which is a bit surprising. For the Fe, it became evident that the observed decrease in XMCD signal was due to the orbital moment reduction (Table 3.6). As it has been anticipated, upon annealing of the sample to $T = 400$ K, both Mn and Fe XAS and XMCD spectra regained the shapes they had before hydrogen dosing, indicating that the hydrogen is desorbed (Figure 3.2.22c,f). Unfortunately, during this process the crystal got slightly loose (cooling down to 2.5K and heating to 400 K cycles induced stress on the clamps holding the crystal), so after desorption the reached temperature was higher than 2.5 K as evidenced by

instabilities in the signal. This didn't allow us to provide direct evidence that the ferrimagnetic ordering has been restored, however the restoration of XAS/XMCD signals indicates that this is the case.

In the next step, we have exposed this sample to atomic hydrogen (H^*), and repeated the measurements – Figure 3.2.23b,d). In this case, the Fe XAS/XMCD spectra changed completely compared to the previous one. A clear and completely different XMCD signal was visible now. The Mn signal was visible now. The Mn on the other hand, didn't change much, except that the intensity of the XMCD feature at 640 eV increased even more compared to the case when it was exposed to molecular hydrogen. Sum rules analysis

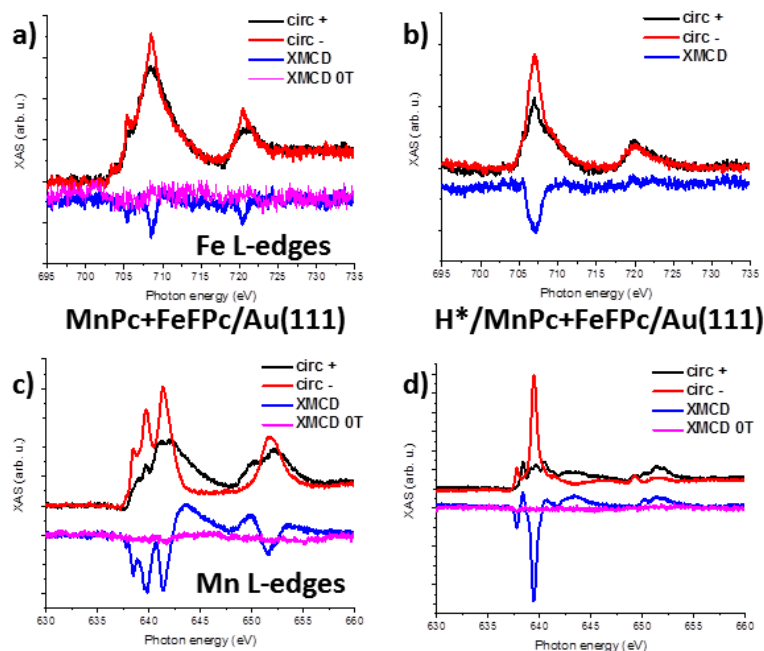


Figure 3.2.23 Mn (a,b) and Fe (c,d) L-edges XAS and XMCD spectra acquired in normal sample geometry of an alternating spin array of MnPc and FeFPc molecules coassembled on Au(111). Spectra are acquired at 2.5 K and 6.8 T before (a,c) and after exposure to atomic hydrogen (H^*) (b,d). Unfortunately desorption trial was here unsuccessful

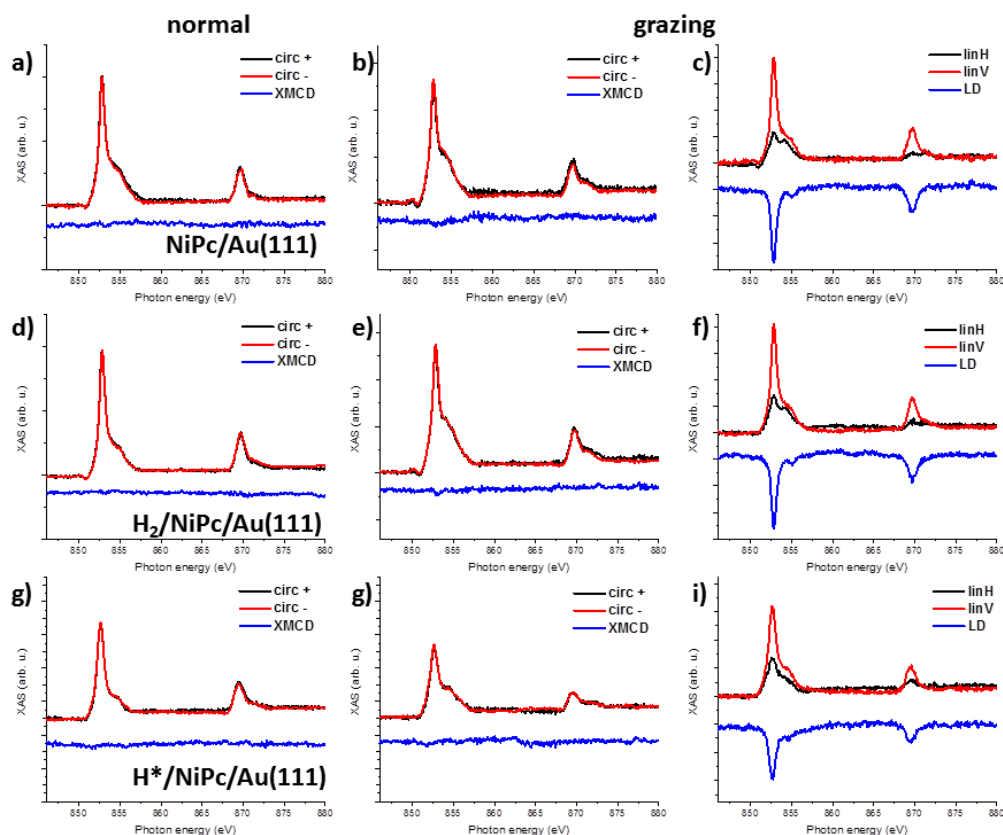
demonstrates again a Mn high-spin state of $S = 5/2$, while the effective spin moment of the Fe corresponded to the $S = 1$ spin state accompanied by the restoration of orbital moment. This could happen according to a mechanism following a similar scenario as in the case of CoPc - a symmetry change of the FeFPc molecule induced by the attachment of two hydrogen atoms to the two periphery nitrogen atoms. Interestingly, the observed high spin state of the MnPc molecules is in apparent contrast to the observed quenching of the magnetic moment evidenced by the vanished Kondo effect reported in previous STM studies^{37,162}. The high spin state in absence of a Kondo signal might be caused by complete decoupling of the MnPc molecules from the substrate. Additional information could be provided by measurements in grazing incidence or

by acquisition of magnetization curves, for example. In our investigations we have focused on the reversible switching of the ferrimagnetic ordering, and have so far only performed measurements in normal incidence of the X-rays.

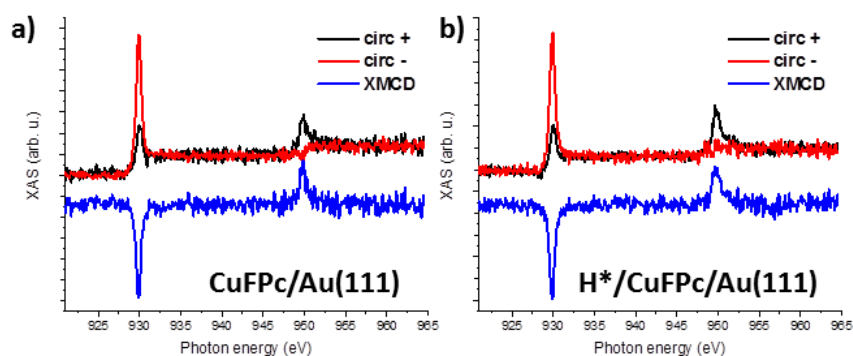
Table 3.6 Orbital (m_L) and effective spin (m_{se}) magnetic moments of Mn and Fe obtained from sum rules analysis applied to spectra acquired in normal sample geometry at 6.8 T and 2.5 K

	MnPc+FeFPc/Au(111)		H ₂ /MnPc+FeFPc/Au(111)		H [*] /MnPc+FeFPc/Au(111)	
	Mn	Fe	Mn	Fe	Mn	Fe
$m_{se} [\mu_B]$	2.0 ± 0.2	0.1 ± 0.1	4.9 ± 0.4	0.2 ± 0.1	5.6 ± 0.5	2.0 ± 0.3
$m_L [\mu_B]$	0.25 ± 0.05	0.50 ± 0.05	0.20 ± 0.05	0.15 ± 0.05	0.23 ± 0.05	0.55 ± 0.05

Finally, we wanted to investigate the influence of hydrogen ligands on phthalocyanine molecules with fully occupied d_{z^2} orbitals. For that purpose we used NiPc and CuFPc molecules adsorbed on Au(111). The NiPc samples were, similar to the previous case characterized before (Figure 3.2.24a-c) and after exposure to molecular (Figure 3.2.20d-f) and atomic (Figure 3.2.20g-i) hydrogen. As intuitively expected, no changes were observed in these spectra not even upon atomic hydrogen exposure. The only possible reason for such behavior is that hydrogen simply doesn't interact with the Ni since the orbital having symmetry in the favored direction is fully occupied. In the earlier STM studies reporting about the attachment of more hydrogen atoms to MnPc, the authors claimed that either 1 or 3 atoms were always attached, but never only two. This selective behavior has been attributed to symmetry issues and has been explained by the propensity of two atoms to desorb as a hydrogen molecule once attached to the same molecule. This could mean that in the case of NiPc, the entire molecule is protected by filling of the d_{z^2} orbital. STM investigation of NiPc molecules against exposure to molecular and atomic hydrogen are needed to check this hypothesis. No change was observed upon exposure of CuFPc /Au(111) to atomic hydrogen for the same reason (Figure 3.2.25).



Figures 3.2.24 Ni L-edges XAS/XMCD/LD spectra acquired in normal (first column) and grazing (next two columns) sample geometries acquired at 2.5 K before (first row) and after molecular (second row) or atomic hydrogen (third row) exposure. Spectra in third column are acquired with linearly polarized light while all the others were acquired with circularly polarized light. The XAS/XMCD spectra in first two columns are acquired with applied field of 6.8 T, XAS/LD in third column with applied field of 0.05 T



Figures 3.2.25 Cu L-edges XAS/XMCD spectra acquired in normal sample geometry at 2.5 K before (a) and after exposure to atomic hydrogen (b). Spectra are acquired with circularly polarized light and with applied field of 6.8 T

In this chapter investigations have been presented on how spin states of various phthalocyanine molecules can be altered by use of chemical stimuli, in particular by hydrogen. Upon exposure to molecular and atomic hydrogen we have observed a broad spectrum of different changes of the spin states in the magnetic molecules selected for investigations. If molecular hydrogen is dosed, the interaction is limited only to the metal center of the phthalocyanine molecules that can influence the filling of the d-orbitals via the modified ligand field. In case of atomic hydrogen dosing, however, also the N-atoms of the molecule interact with the dosed hydrogen. This leads to symmetry changes that need to be taken into account when ligand field is modeled. In addition, it has been shown that in the former (molecular hydrogen) case, this process is completely reversible, while in the latter (atomic hydrogen) case it leads to irreversible changes of both the spin state of the metal center and of the molecule. Last, it seems that hydrogen is able to induce changes only if the d_{z^2} orbital is partially occupied. With all this in mind, we managed to tune the anisotropy of CrPc molecules, induce spin in quenched CoPc molecules or quench (decrease) it in FeFPc. Also we have reversibly switched the ferrimagnetic ordering in our coassembly and have interpreted the results in the framework of ligand field theory. Naturally, some of these spectroscopic observations are to be complemented by local probe investigations as well as by theoretical/computational simulations towards a more complete and elusive understanding of the surface enabled phenomena.

3.3.2 SURFACE MODIFICATION OF CO FERROMAGNETIC FILMS FOR TUNING EXCHANGE INTERACTIONS OF ADSORBED MOLECULES

Another important aspect of concern in the context of spinterface engineering is definitively the substrate as a support of on-surface architectures. The surface and surface site specific electronic states also crucially affect the surface physicochemical properties of a material. The adsorption potential of the surface, for example, can be locally modified which drives and/or directs self-assembled structures of ad-molecules^{166,167}. In case of on-surface metalation, functionalization of surfaces can facilitate or inhibit the reactions due to steric hindrance or reduced surface diffusion^{168,169}. In light of molecular magnetism, small structural changes on the substrate can induce big changes in the magnetic response of spin bearing ad-molecules due to the subtle nature of these interactions. It was shown that introduction of an oxygen adlayer on ferromagnetic supports flips the magnetic interactions from FM to AFM^{23,106}. Also the opposite occurs, as demonstrated in Section 3.1.1 of this Thesis. A similar effect has been shown for graphene used as a spacer layer between molecules and the substrate²⁴. Adlayers have served to also stabilize fragile SCO molecules¹⁷⁰ or tune the magnetic anisotropy^{14,97}. Every new support represents a new playground for tuning the magnetic interactions and provides therefore an important tool for investigations of on-surface magnetism.

Following up on the experiments on O terminated Co and Ni surfaces, our attention was driven to peculiar properties of also graphene terminated ferromagnetic substrates. In light of these discoveries, we started seeking for a new possibility to alter the surface composition of our Co and Ni films. Plausible candidates were provided by elements in the vicinity of O in the periodic table of elements. This is supported with both their similar size and their similar chemical properties. We first chose N and started to search the literature for preparation techniques to incorporate N into our metallic films. This was not possible to happen in a process similar to the one used for creating oxygen terminated substrates, where we had oxidized our films in the intermediate step of metal deposition (more details in Section 2.7) by simple exposure to O₂ gas. The high chemical stability of N₂ molecules provides an

obstacle here. On the other hand, several examples existed in literature where N reconstructed Cu substrates were prepared by low energy sputtering with nitrogen ions¹⁷¹⁻¹⁷³, where a sputter gun was used to provide ionized and dissociated nitrogen molecules that were then accelerated towards the sample. Upon such treatment the samples had been annealed and nicely ordered $c(2 \times 2)$ superstructures were reported on Cu. We further optimized this method for the specific case of Co film grown on Cu(001) single crystals. At first we have tried to do so on thin Co film already grown on Cu(001). The optimization here included varying the nitrogen pressure, the energy of the sputter gun, the sputtering time and the sputtering angle on one side as well as the temperature and the duration of the annealing cycle on the other side of the process. The results were evaluated by means of XPS where the N content on the sample was determined. LEED has been used to assess the uniformity of the N formed surface superstructure by the appearance and sharpness of the $c(2 \times 2)$ diffraction spots. With increasing N_2 pressure or sputtering time it was expected that the N content in the Co sample increases, while annealing oppositely decreases the N content on the sample. After confirming this general trend, significant effort has been put into finding parameter combinations that were yielding sufficient amount of nitrogen. Once satisfactory XPS results were achieved, samples were subjected to STM investigations to assess the roughness of the substrate. Satisfactory XPS/LEED results have been achieved within a range of parameter settings. STM, however, was always showing that the roughness of the films was high as evidenced in Figure 3.3.26c. We have therefore altered the N exposure procedure in that that we first created nitrogen superstructures on Cu(001) and subsequently grew the Co film. Very much to our initial surprise, a N surfactant mediated growth behavior has been observed and led fast to satisfactory results displayed in Figure 3.3.26d. In a further optimized procedure, the Cu(001) crystal was sputtered for 10 minutes in $p(N_2)=7 \times 10^{-7}$ mbar with a kinetic energy of the sputter beam of 500 eV while the surface was kept perpendicular to the incoming ion beam and was simultaneously annealed to around $T = 500$ K. The annealing was continued after sputtering ended for another 10 minutes. This typically yielded around 4 at% of nitrogen on Cu(001). Subsequent growing of the Co film according to the procedure described in Section 2.7 was producing smooth

c(2x2)-nitrogen terminated surface of Co as seen by LEED and STM. The N/Co film was growing in the form of extended islands with sharp edges along [100] and [010] directions, similar to the O/Co film and in contrast to the bare Co film (comparison of LEED patterns and STM images of Co, O/Co and N/Co substrates is shown in Figure 3.3.26a-c). During literature research for optimization of the process for N/Cu preparation, another Cu superstructure, namely Cl c(2x2) came to our attention^{169,174–176} and we were interested in trying to prepare it also on Co. Two different procedures for the preparation of this superstructure were proposed; The first one involved exposure of the sample to Cl₂ gas and subsequent annealing to facilitate diffusion of Cl-atoms across the substrate, while the other, reported as more favorable, involved the deposition of the ionic compound CuCl₂ onto clean Cu crystal and subsequent annealing^{169,174–176}. We have selected the latter, less invasive procedure and optimized the amount of CuCl₂ needed for the formation of a superstructure on the complete layer. For this purpose, we used anhydrous CuCl₂ that contained no (or less) water in the crystal structure, in order to reduce possible contaminations. During Co deposition, the sample was heated (to T = 400 K) and surfactant mediated growth occurred like in the

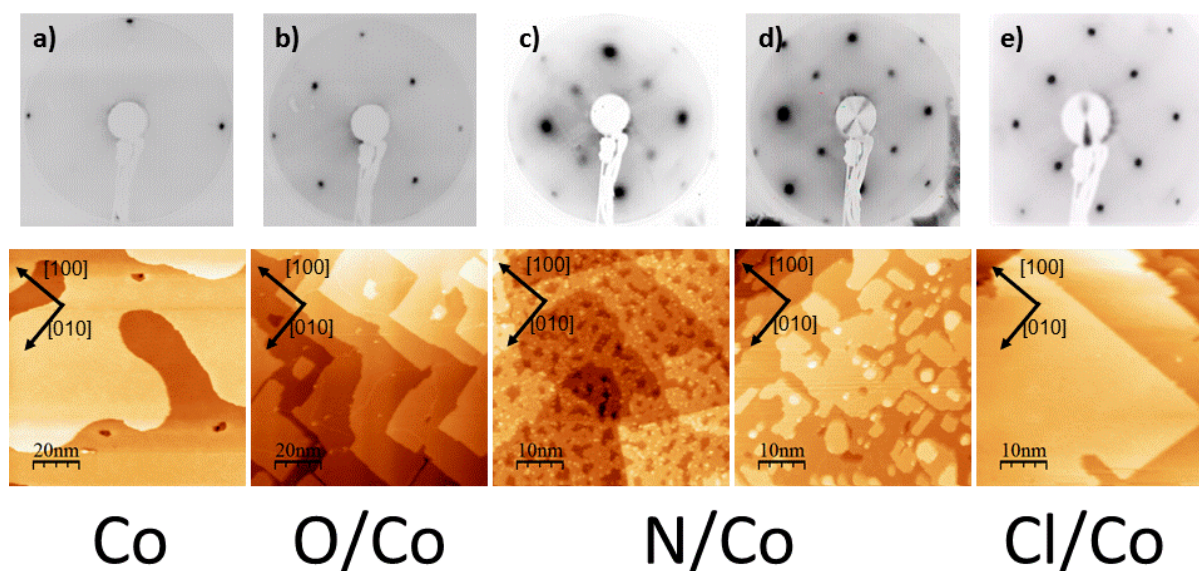


Figure 3.3.26 Comparison of LEED patterns and STM images of Co (a), O/Co (b), two N/Co (c, d) and Cl/Co (e) substrates. LEED images are acquired at electron energies of 53.2, 53.2, 134.0, 126.3 and 135.2 eV from left to right. STM images are acquired with $U_b=1.1V$, $I_t=30pA$; $U_b=1.25V$, $I_t=10pA$; $U_b=-0.51V$, $I_t=10pA$; $U_b=-0.81V$, $I_t=10pA$; $U_b=-0.48V$, $I_t=10pA$ parameters, from left to right

previously explained cases. Similar to the case of O and N, Cl was migrating to the surface, was floating there during the Co growth, and was forming a $c(2 \times 2)$ superstructure. The formation of this superstructure is reflected in the distinct diffraction spots in the LEED patterns, but also in the observation of rectangular terraces with sharp edges along $[100]$ and $[010]$ directions as they are visible in the STM images presented in Figure 3.3.26e. Although LEED and STM already provide valuable information about these superstructures, more detailed insight is desirable for understanding the subtle magnetic interactions therein.

For this purpose, we decided to employ the X-ray Photoelectron Diffraction (XPD) technique as briefly introduced in Section 2.3. This method has recently received attention as it helped understanding structures of several systems that were difficult to assess otherwise. For example, due to its chemical sensitivity, XPD helped unravel the structure of the buckled h-BN layer, the orientation of adsorbed C₆₀ molecules or even to look inside endohedral fullerenes^{65,177–179}. The principle behind is rather simple – the emitted photoelectrons are scattered by the surrounding atoms and lead to the formation of diffraction patterns that can be recorded in their angular dependence at photoelectron energies selected by the analyzer. The scattering can be followed either by angular (both polar and azimuthal) or energy scans and results in angle or energy resolved diffraction patterns. The former patterns can in principle be transformed into real-space images by a 2D phased Fourier transform but it was shown that rather large errors and artefacts appear in the such determined real space images¹⁸⁰. In order to circumvent this problem, the analysis is performed by guessing the structure and by simulating the diffraction pattern using single or multiple scattering codes; the simulated diffraction patterns are then compared to the experimentally measured ones and the quality of the agreement is quantified by calculating R-factors⁶⁵. This way it is possible to obtain very precise values of interatomic distances, which are also of interest for the characterization of the superstructures we obtained here.

We decided to acquire angle resolved diffraction patterns for two newly created superstructures (N/Co and Cl/Co) but also for the O/Co for easier comparison and determine the distance at which adsorbates (O, N and Cl) are residing. Samples were prepared in the Surface Science lab and transferred to the PEARL beamline of the SLS in an already

established procedure with a vacuum suitcase. Here, measurement conditions were optimized to acquire suitable signals of both substrate (Co) and superstructures (O, N and Cl). For the acquisition of angle resolved scans the Co2p, O1s, N1s and Cl2p photoelectron peaks were used and the photon energy was tuned such that all peaks appeared at the kinetic energy of $E_{\text{kin}} = 217.0$ eV. Lowering the kinetic energy is beneficial from several aspects: it improves the Photoionization Cross-Sections, increases the surface sensitivity due to lowering of the escape depth of electrons and promotes scattering processes. The angle scans were then acquired in a sweeping mode (several eVs around photoelectron peak) with 2 degree steps of the polar angle (θ) from 0 to 84 and 40 degree steps of the azimuthal angle (ϕ) from 0 to 360. Thereby these angle scans allow for the complete stereographical mapping of the diffraction hemisphere with the wide angular acceptance of the analyzer (60 degrees). The scans were then processed using the IgorPro software according to the following procedure: The raw data was processed by first performing a background subtraction and then by integrating the peak areas. Next, the detector angle is cropped to the useful angle (-25, 25 degrees). This is necessary as the efficiency of the analyzer is very low at high angles. Once the data is cropped to this range, it is also normalized first to remove inhomogeneities of the detector against the rotation of the detector angle axis and later also to remove the polar angle dependence. The scan is then plotted as a stereographic projection. Here, refinements can be performed and the result is then used for a comparison of the simulated patterns during the structure optimization process. The resulting measured scans of all aforementioned superstructures are displayed in plots a) and c) of Figures 3.3.28 (O/Co), 3.3.30 (N/Co) and 3.3.32 (Cl/Co).

In order to extract structural information from the measured angle scans, we had to perform multiple scattering simulations using the PEARL multiple-scattering cluster calculations and structural optimization (PMSCO) code developed by PEARL beamline scientist Dr. Matthias Muntwiler. The code is in its core based on the Electron Diffraction in Atomic Clusters (EDAC)¹⁸¹ code but provides several upgrades compared to the original code. These include the possibility of running the code in different modes, of averaging over multiple symmetries, of calculating the modulation function and most importantly of several

different structural optimization algorithms i.e. particle swarm optimization (PSO), grid search and gradient search. In particular, we have used the PSO algorithm for the optimization of the structural parameters. In this mode, structural parameters are optimized by interactively trying to improve a candidate solution with regard to a given measure of quality. In our case that means by comparison of measured and simulated spectra reflected in the calculated R-factor. This allows for the optimization of multiple input parameters used for MSC in a very efficient way.

The starting point for optimization is based on a cluster of atoms included in the simulation and defining emitting atoms. The cluster is in this case modeled as a slab consisting of 3 layers of Co atoms in fcc crystal structure with [001] direction (Figure 3.3.27). It is centered on an adsorbate atom that is used as emitter when adsorbate scans are simulated. Due to the different symmetry of the Co atoms surrounding adsorbate, all atoms within the red circle in Fig. 3.3.27 had to be included as emitters in simulations. The total number of atoms included in cluster was defined with r_{max} , the diameter of the green circle around the central adsorbate atom. In the calculations, the distance between the adsorbate atom and the first Co layer (d_{ACo}), but also the distances between first and second ($d_{Co_1Co_2}$), and second and third ($d_{Co_2Co_3}$) layers of Co atoms were varied. Beside these, a few additional parameters needed for the code ($distm$, $tdebye$, $tsample$, V_0 , Z_{surf}) were optimized. A large part of the effort was put on the optimization of structural parameters, while other parameters were left open for optimization. For all systems, several rounds of optimization were needed to reduce the R-factor. Limits for the starting parameters for each are listed in Tables 3.7 (O/Co), 3.8 (N/Co) and 3.9 (Cl/Co). The distributions of R-factors across the mentioned structural parameters are displayed in Figure 3.3.29 (O/Co), Figure 3.3.31 (N/Co) and Figure 3.3.33 (Cl/Co). For the lowest obtained R-factor in each scan, the simulated diffraction pattern is displayed next to the measured diffraction pattern in plots b) and d) of Figures 3.3.28 (O/Co), 3.3.30 (N/Co) and 3.3.32 (Cl/Co).

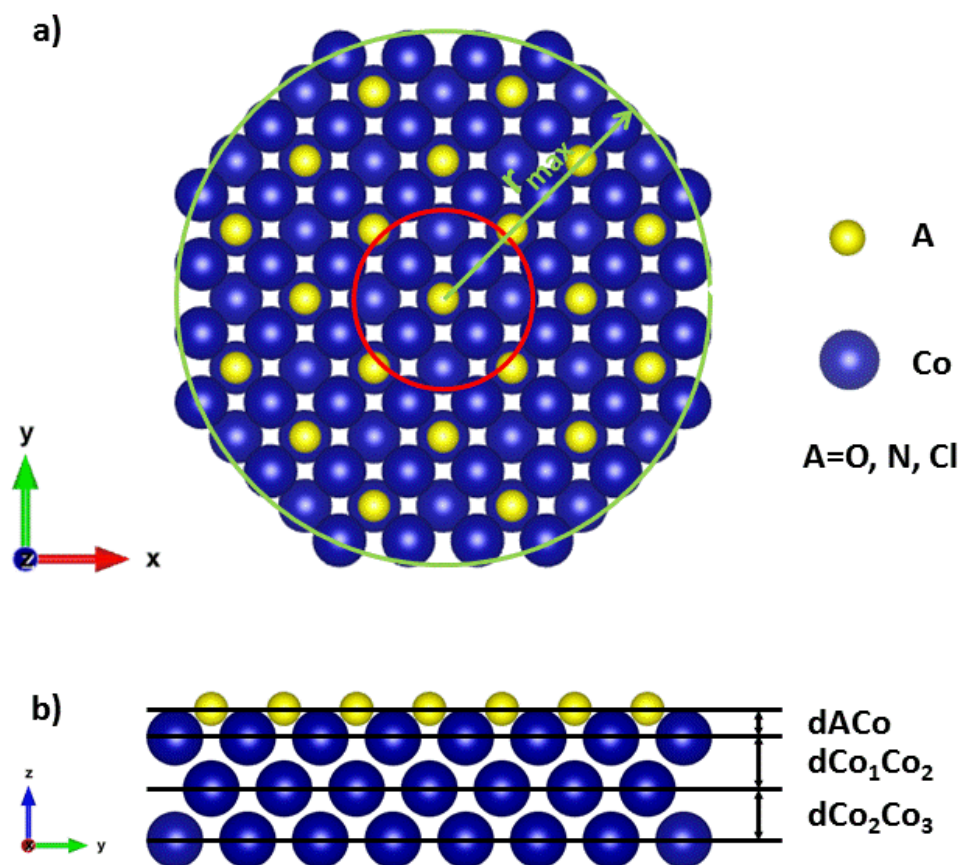


Figure 3.3.27 Top (a) and side (b) view of the model cluster used for simulations of diffraction patterns. The red circle denotes the emitter atoms used in the simulations, while green one defines total number of atoms used in the simulation

O/Co superstructure

Table 3.7. Starting parameter limits (min, max) for the MSC of O/Co system

	O1s					Co2p	
	calc 1	calc 2	calc 3	calc 4	calc 5	calc 1	calc 2
dOCo/A	-3.5, 1.5	0.0, 1.0	-3.0, -1.0	0.1, 0.9	0.1, 0.9	0.1, 0.9	0.1, 1.1
dCo1Co2/A	1.6, 2.0	1.4, 1.8	1.4, 1.8	1.4, 1.8	1.4, 1.8	1.4, 1.8	1.5, 2.0
dCo2Co3/A	1.7, 1.9	1.75, 1.85	1.75, 1.85	1.55, 1.85	1.55, 1.85	1.75, 1.85	1.55, 1.85
distm /Å	4.252	4.252	4.252	4.252	4.252	4.252	4.252
rmax/Å	6.0, 10.0	5.0, 9.0	5.0, 9.0	4.0, 9.0	5.0, 9.0	5.0, 9.0	5.0, 15.0
tdebye/K	386	386	386	386	386	386	386
tsample/K	300, 600	150, 450	150, 450	50, 400	50, 400	50, 400	50, 500
V0/V	0, 20	0, 30	0, 30	5, 20	5, 20	5, 20	0, 20
Zsurf/Å	0.5, 1.5	0.5, 1.5	0.5, 1.5	0.5, 2.0	0.5, 2.0	0.5, 1.5	0.5, 2.0

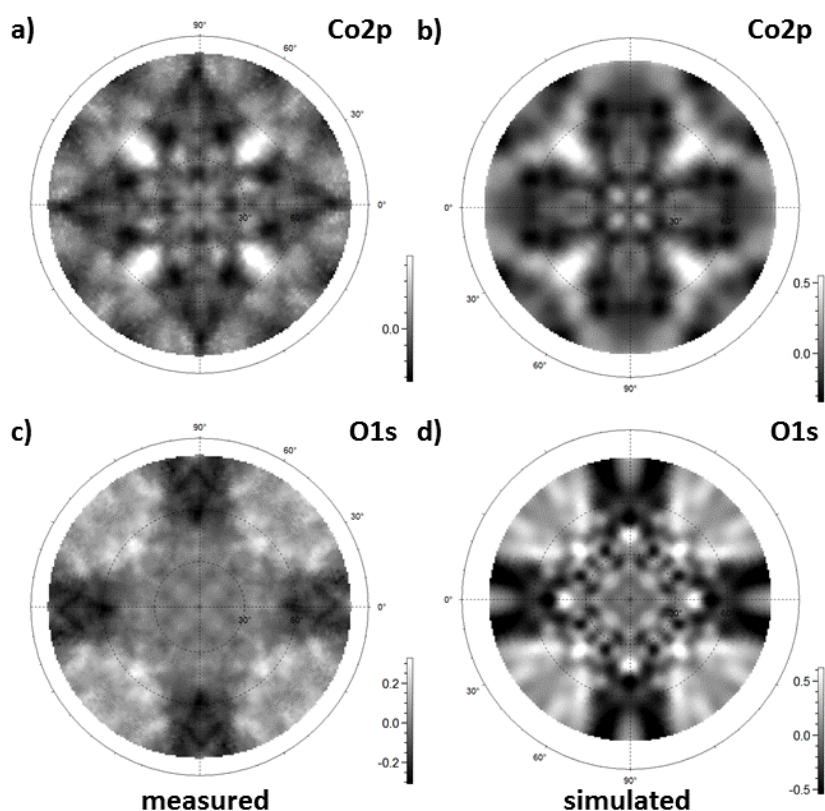


Figure 3.3.28 Stereographic representations of experimentally obtained (a, c) and simulated (b, d) diffraction patterns of Co2p and O1s scans of O/Co superstructure. The presented calculated plots represent patterns obtained with the lowest R-factor

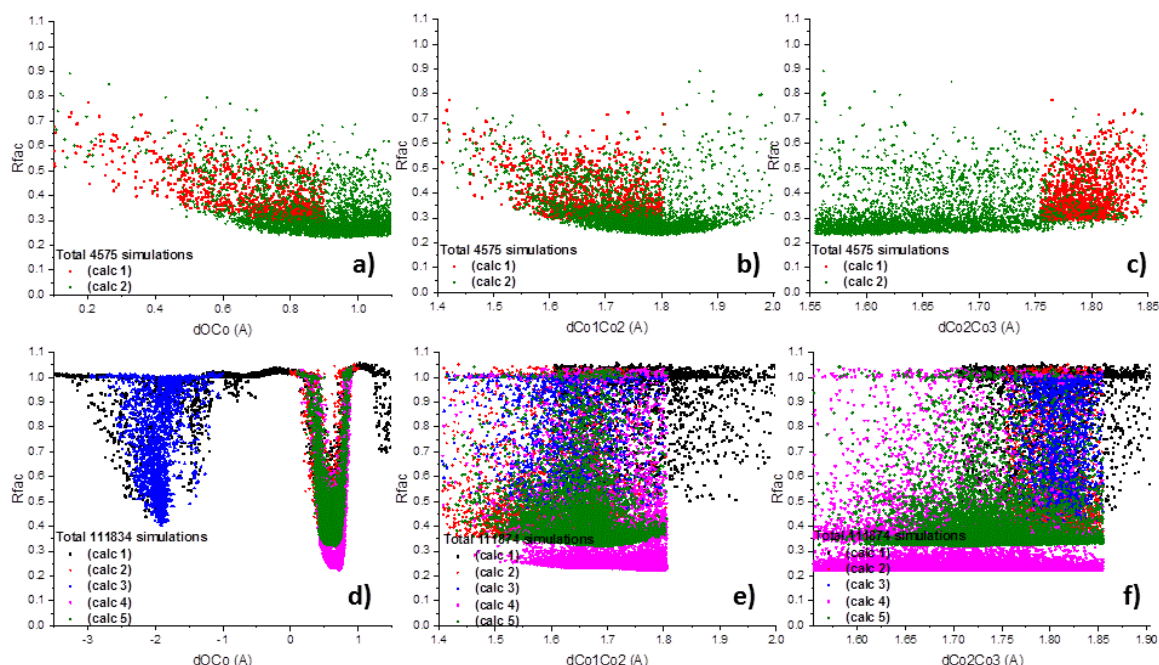


Figure 3.3.29 Distributions of *R*-factors over structural parameters $d\text{OCo}$ (a,d), $d\text{Co}_1\text{Co}_2$ (b,e) and $d\text{Co}_2\text{Co}_3$ (c,f) for $\text{Co}2p$ (a-c) and $\text{O}1s$ (d-f) angular scans on O/Co superstructure.

For the optimization of structural parameters of the O/Co superstructure, 7 calculations were performed, 5 on $\text{O}1s$ and 2 on $\text{Co}2p$. In total 116409 simulations were performed, 111834 on $\text{O}1s$ scan and 4575 on $\text{Co}2p$ scan. Due to the way bigger number of emitters in the case of $\text{Co}2p$ scans, simulations were taking way longer, so the number of simulated structures, and thus the convergence is lower. In the $\text{O}1s$ scan simulations, clear *R*-factor minima are visible for $d\text{OCo}$ and allow better convergence and determination of this value. The lowest $R_{\min} = 0.23 \pm 0.03$, giving for $d\text{OCo} = 0.65 \pm 0.11 \text{ \AA}$. As for the determination of the two other structural parameters, no minima is visible for the $d\text{Co}_2\text{Co}_3$. This can be expected, as this distance shouldn't change (not so sensitive to adsorbate). The $d\text{Co}_1\text{Co}_2$ on the other hand displays the minima in $\text{Co}2p$ scan and the value we get for the $R_{\min} = 0.23 \pm 0.03$ is same as for the $\text{O}1s$ scan. This yields $d\text{Co}_1\text{Co}_2 = 1.80 \pm 0.10 \text{ \AA}$ and is fitting the value obtained for interlayer distance from the crystallographic data.

N/Co superstructure

Table 3.8. Starting parameter limits (min, max) for the MSC of N/Co system

	N1s				Co2p			
	calc 1	calc 2	calc 3	calc 4	calc 1	calc 2	calc 3	calc 4
dNCo/A	-3.5, 3.5	-1.0, 0.0	0.0, 1.0	-1.0, 0.0	-1.0, 0.0	0.0, 1.0	-1.0, 0.0	0.0, 1.0
dCo1Co2/A	1.6, 2.0	1.6, 2.0	1.6, 2.0	1.6, 2.0	1.6, 2.0	1.6, 2.0	1.6, 2.0	1.6, 2.0
dCo2Co3/A	1.7, 1.9	1.7, 1.9	1.7, 1.9	1.7, 1.9	1.7, 1.9	1.7, 1.9	1.7, 1.9	1.7, 1.9
distm/A	4.252	4.252	4.252	4.252	4.252	4.252	4.252	4.252
rmax/A	6.0, 10.0	6.0, 10.0	6.0, 10.0	6.0, 10.0	6.0, 10.0	6.0, 10.0	6.0, 10.0	6.0, 10.0
tdebye/K	386	386	386	386	386	386	386	386
tsample/K	100, 500	100, 500	100, 500	300, 700	300, 900	15, 400	300, 900	15, 400
V0/V	0, 30	0, 30	0, 30	0, 30	0, 30	0, 30	0, 30	0, 30
Zsurf/A	0.5, 1.5	0.5, 1.5	0.5, 1.5	0.5, 1.5	0.5, 1.5	0.5, 1.5	0.5, 1.5	0.5, 1.5

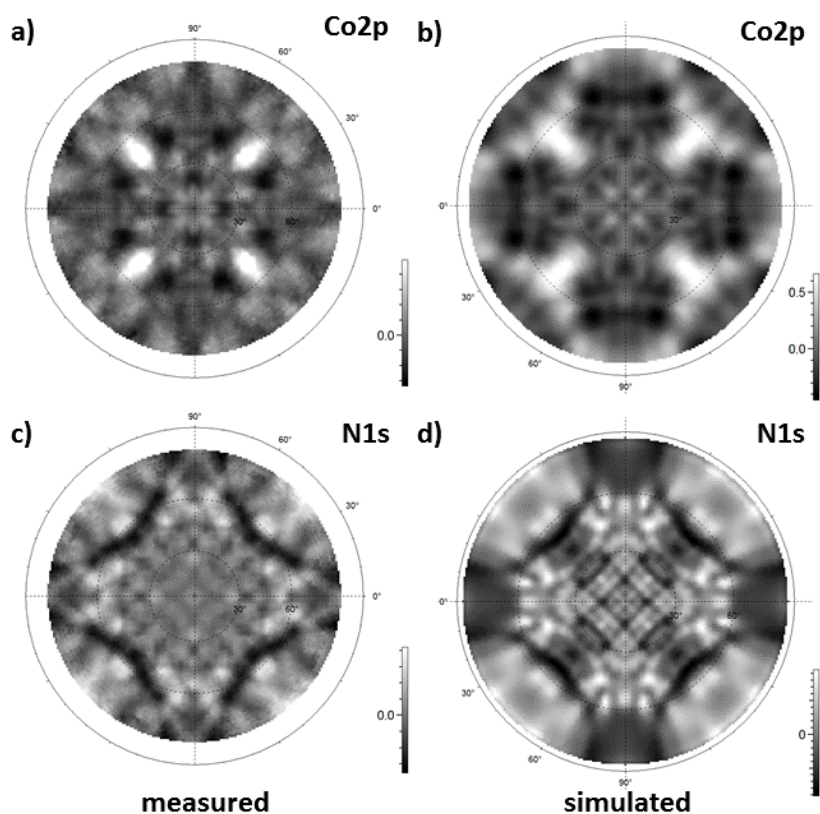


Figure 3.3.30 Stereographic representations of experimentally obtained (a, c) and simulated (b, d) diffraction patterns of Co2p and N1s scans of N/Co superstructure. The presented simulated ones represent patterns obtained with the lowest R-factor

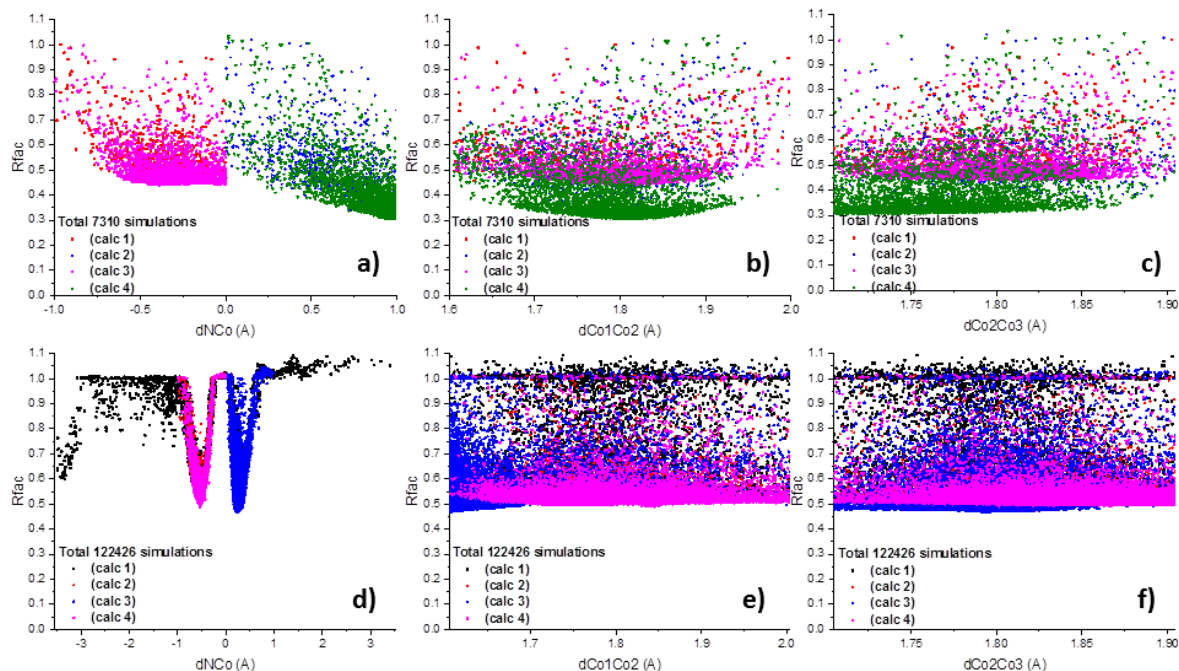


Figure 3.3.31 Distributions of R -factors over structural parameters $dNCo$ (a,d), dCo_1Co_2 (b,e) and dCo_2Co_3 (c,f) for $Co2p$ (a-c) and $N1s$ (d-f) angular scans on N/Co superstructure

In the case of N/Co superstructure, 8 calculations were performed, 4 on $N1s$ and 4 on $Co2p$. In total 129736 simulations were performed, 122426 on $N1s$ scan and 7310 on $Co2p$ scan. Again, in the adsorbate, $N1s$ scan simulations, clear R -factor minima are visible for $dNCo$ but are higher than values achieved in O/Co case. The lowest $R_{min} = 0.47 \pm 0.07$, giving for $dNCo = 0.27 \pm 0.11$ Å which is way lower than in case of O/Co . Since N has a smaller radius it is thus expected that it can diffuse deeper into the substrate. As for the determinations of two other structural parameters, again no minima is visible for the dCo_2Co_3 as expected. The dCo_1Co_2 on the other hand displays the minima in $Co2p$ scan and the value we get for the $R_{min} = 0.30 \pm 0.04$ is same as for the $N1s$ scan. This yields same value for $dCo_1Co_2 = 1.80 \pm 0.10$ Å as in the case of O/Co and is expected as both N and O are rather small to induce significant change in the Co layer.

Cl/Co superstructure

Table 3.9. Starting parameter limits (min, max) for the MSC of Cl/Co system

	Cl2p					Co2p		
	calc 1	calc 2	calc 3	calc 4	calc 5	calc 1	calc 2	calc 3
dClCo/A	-3.5, 3.5	-0.1, 1.0	1.1, 1.75	1.8, 2.3	2.31, 3.5	-0.1, 1.0	1.1, 1.75	1.8, 2.3
dCo1Co2/A	1.6, 2.0	1.7, 2.0	1.6, 2.0	1.6, 2.0	1.6, 2.0	1.6, 2.0	1.6, 2.0	1.6, 2.0
dCo2Co3/A	1.7, 1.9	1.6, 2.0	1.6, 2.0	1.6, 2.0	1.6, 2.0	1.6, 2.0	1.6, 2.0	1.6, 2.0
distm/A	4.252	4.252	4.252	4.252	4.252	4.252	4.252	4.252
rmax/A	6.0, 10.0	5.0, 10.0	5.0, 10.0	5.0, 10.0	5.0, 10.0	5.0, 10.0	5.0, 10.0	5.0, 10.0
tdebye/K	386	386	386	386	386	386	386	386
tsample/K	100, 500	50, 450	50, 450	50, 450	50, 450	50, 450	50, 450	50, 450
V0/V	0, 30	0, 30	0, 30	0, 30	0, 30	0, 30	0, 30	0, 30
Zsurf/A	0.5, 1.5	0.5, 1.5	0.5, 1.5	0.5, 1.5	0.5, 1.5	0.5, 1.5	0.5, 1.5	0.5, 1.5

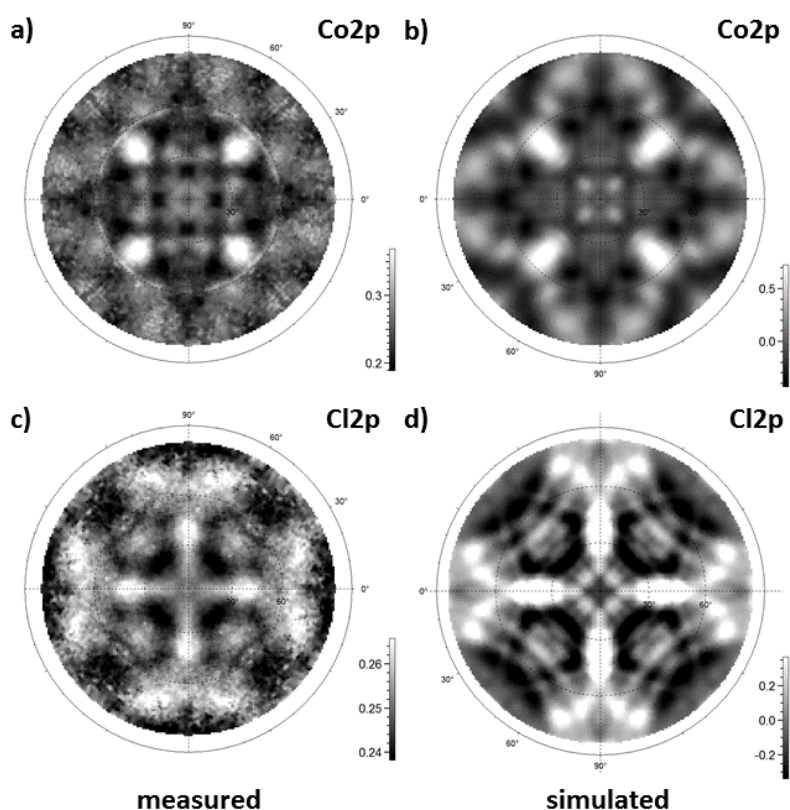


Figure 3.3.32 Stereographic representations of experimentally obtained (a, c) and simulated (b, d) diffraction patterns of Co2p and Cl2p scans of Cl/Co superstructure. The presented simulated ones represent patterns obtained with the lowest R-factor

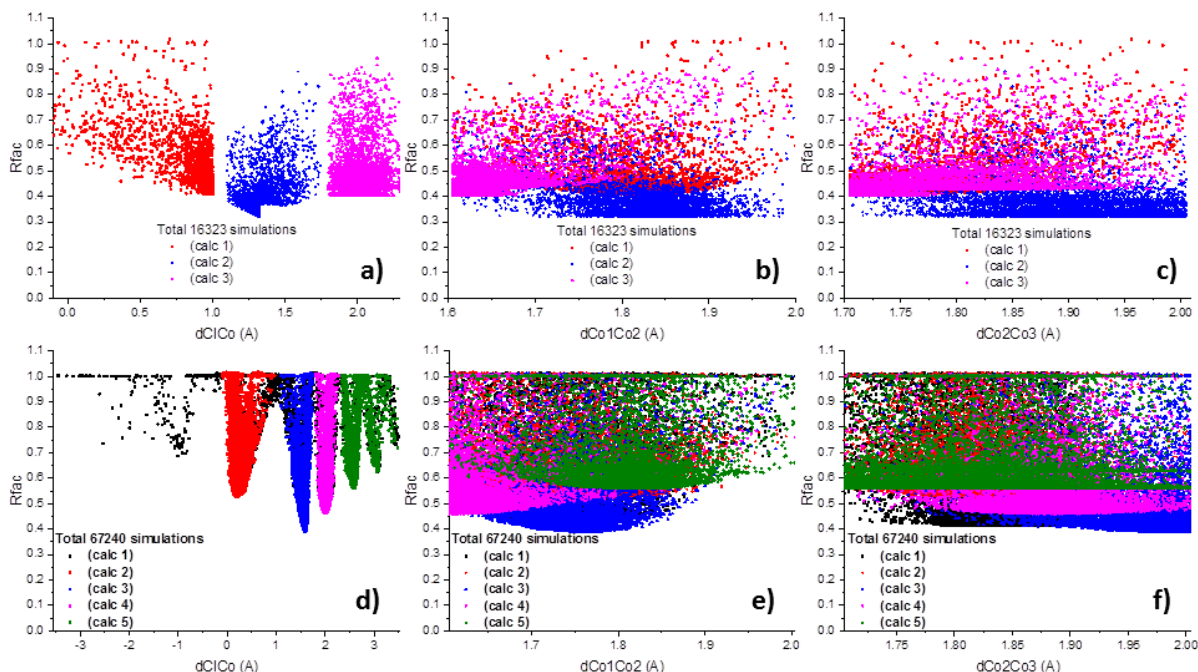


Figure 3.3.33 Distributions of *R*-factors over structural parameters *dClCo* (a,d), *dCo₁Co₂* (b,e) and *dCo₂Co₃* (c,f) for Co2*p* (a-c) and Cl2*p* (d-f) angular scans on Cl/Co superstructure

In the last investigated case of the Cl/Co superstructure, 8 calculations were performed, 5 on Cl2*p* and 3 on Co2*p*. In total 83563 simulations were performed, 67240 on Cl2*p* scan and 16323 on Co2*p* scan. Multiple *R*-factor minima are visible for *dClCo* in a Cl2*p* scan simulations. The lowest obtained *R*-factor is $R_{\min} = 0.39 \pm 0.06$, giving for $dClCo = 1.58 \pm 0.08$ Å which is way higher (almost whole Co-Co interlayer distance) than in both cases of O/Co and N/Co but is in line with measurements of this distance on Cu^{169,174–176}. Cl has a very big atomic radius and is thus expected to rest further away from the substrate. Since in the Co2*p* scan, no minima are observable for any of the structural parameters, the minimum for *dCo₁Co₂* in the Cl2*p* scan is used for *dCo₁Co₂* determination. The R_{\min} is reached in the same calculation and the determined distance $dCo_1Co_2 = 1.75 \pm 0.10$ Å is slightly lower than in the previous two cases. The obtained values of the *d*Co distances can help predict the magnetic properties of adsorbed molecules on these substrates. Moreover, the demonstrated approach can even be extended to the direct investigation of the adsorption geometries of such molecules, giving the XPD method significant importance in the investigations of other low-dimensional systems than those simple cases of adsorbate induced reconstructions.

3.4 NOVEL EXPERIMENTAL SETUPS

The investigation of novel low-dimensional magnetic system is an often challenging job that asks for the creative and coordinated design of experiments or for the development/adaptation of novel techniques to be achieved.

3.4.1 EXPERIMENTAL SETUP FOR TIME-RESOLVED XAS AT SIM BEAMLINE OF SLS

Although the development of synchrotron light sources brought along new possibilities to investigate matter with UV/X-ray light and helped address many of the questions that were before thought as impossible to be investigated there is a limit of how far it can reach. Synchrotron X-rays are suitable for probing structures reaching the nanometer scale in space and beyond – as shown in this thesis it is suitable for investigations of molecular and atomic structures. The “reachable” time scale, however, lies far beyond fundamental timescales of magnetism. This has triggered discussions and implementations of novel light sources that can cover also these time scales, in particular X-ray Free Electron Lasers (Figure 3.4.1). In parallel with the development of the X-FELs, several ways of improving the time scale

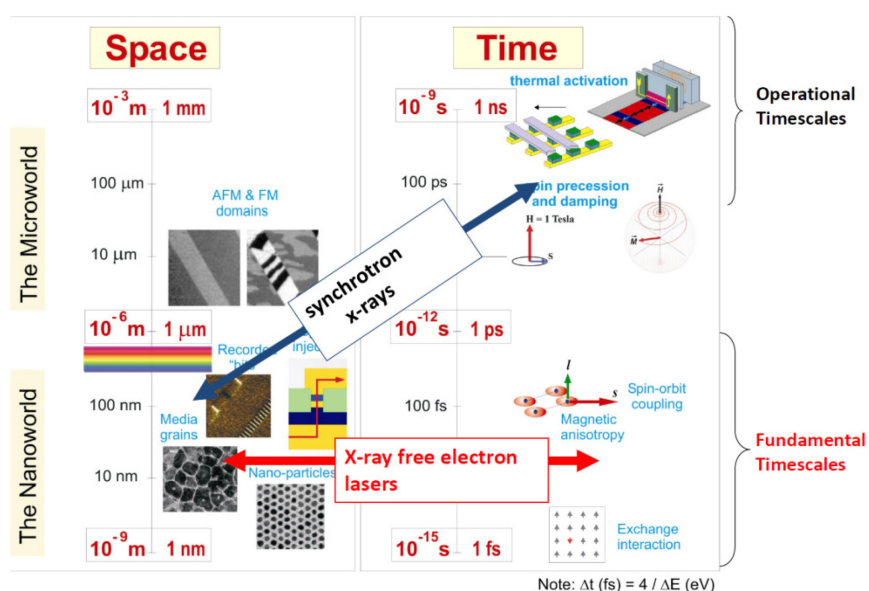


Figure 3.4.1 Length and time scales covered by the synchrotron and FEL sources^{4,69}

reachable with synchrotron radiation were proposed: A particularly suitable one is taking advantage of time-structure of the synchrotron light which depends on the pulse shaping of the electron bunches in the ring that has

become more and more advanced with the implementation and onward development of the RF techniques to operate the 2nd and 3rd generation synchrotron light sources. Namely, electrons used to produce light in synchrotrons are not distributed continuously but are rather separated into bunches placed into well-defined pockets. The number of possible pockets is defined by the RF frequency of the machine and in case of the SLS there are 480 pockets each of 2ns width. In a typical SLS running mode, 390 of them are filled in a continuous, so-called multibunch mode (for example from 0 to 389) while one, 4 times more intense bunch referred to as Camshaft is placed in the separate pocket nr 465 and is used for various diagnostic purposes. If the X-ray signal originating from this bunch can be resolved from the rest of them, it can serve as a probe pulse for the laser pump pulse in a time-resolved pump-probe experiment (Figure 3.4.2). The temporal resolution here is limited to the width of such a pulse (typically 50-100ps) and the repetition rate to the one of the synchrotron used (1.04MHz in case of SLS). In several experiments it has been demonstrated that this separate bunch can be well resolved by an avalanche photodiode and that it can be used for such experiments^{182,183}. This is however limited to experiments where X-rays are transmitted through the samples, which in our case was not applicable. In addition, the TEY mode that is commonly used in our static measurements was not applicable for this type of measurements as there was no possibility to temporally resolve the current flowing to the sample. Therefore, we have put significant effort into developing a setup capable of detecting the time-resolved signal generated in X-ray absorption related photoelectron emission. In order to do so, a new data acquisition mode designed by Pollux beamline scientist Jörg Raabe has been implemented and optimized. This involved mounting and setting up a

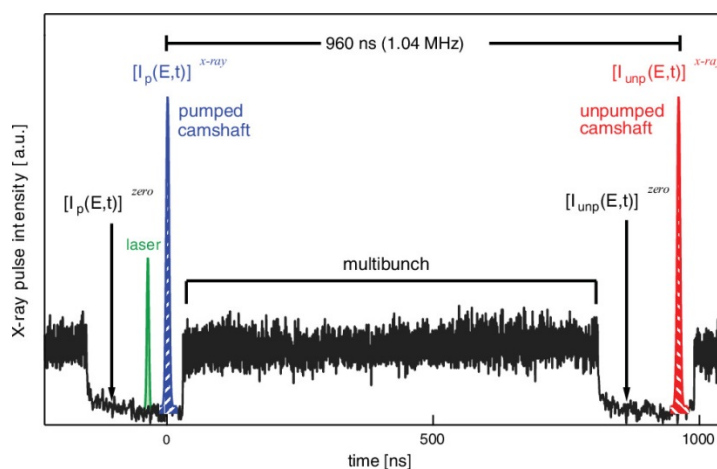


Figure 3.4.2 Time structure of the SLS and demonstration of possibility of using Camshaft for pump-probe experiments¹⁸²

suitable detector, coupling it to the fast electronics and readout channels at the beamline, and the development of acquisition software and several tests.

For this purpose, Multi-Channel Plate (MCP) detectors capable of acquiring signals with high temporal resolution that is typically used in time-of-flight mass spectrometry can be used for the detection of the emitted electrons (photo, Auger and secondary electrons) upon X-ray absorption. The advantage of this PEY mode is also that it can be biased with certain voltage to attract or filter electrons within a certain energy range. Setting up the detector involved the development of an electronic circuitry serving as the interface for connecting it to fast counting electronics based on field-programmable gate array (FPGA) integrated circuits. The FPGA circuits were programmed by Jörg Raabe and served for a fast readout of the signals produced by the MCP detector. In particular, the electrons emitted from the sample were amplified and transformed into a voltage pulse upon hitting the MCP detector. This pulse was then analyzed by the fast FPGA circuits. The pulses were timestamped upon detection and collected over a certain timeframe (typically 50-90 ms) as defined by the external trigger. They were sorted/counted by the detection time by placing into one out of

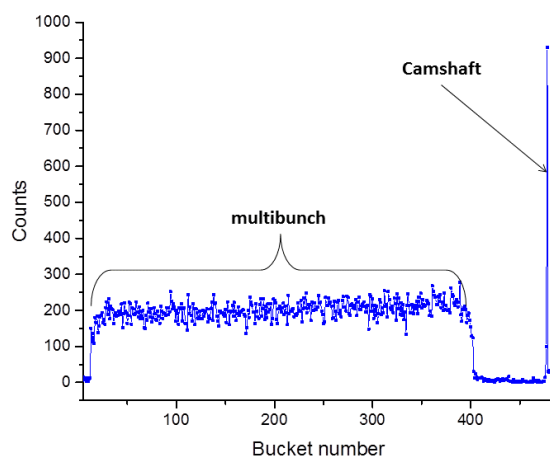


Figure 3.4.3 Resolved time structure of the SLS by use of MCP detector

the Figure 3.4.3.

Further on, we tested the acquisition setup and recorded spectra by looking into the Camshaft signal. Comparison of normal TEY acquired and in this way obtained TR-XAS are

480 (if one filling pattern is acquired) or 960 (if two consecutive patterns were acquired) time windows and then sent to a readout unit. At the readout unit, an array containing 480 or 960 elements with numbers of counts is detected, representing one or two filling patterns of the SLS. The data was immediately processed by self-written data acquisition code. This allowed us to fully resolve the filling pattern of the SLS as evidenced in

shown in the Figure 3.4.4. As expected, the signal quality on the TR-XAS is significantly worse as we are looking into signal produced only by 4/394 photons (assuming that 4 times more electrons in the camshaft produce 4 times more photons), and longer acquisition is required for signal improvement. Nevertheless, the setup is ready and proved to be capable of resolving XAS signals on the time scale of the camshaft pulse and as such also ready to be used in TR-XAS experiments.

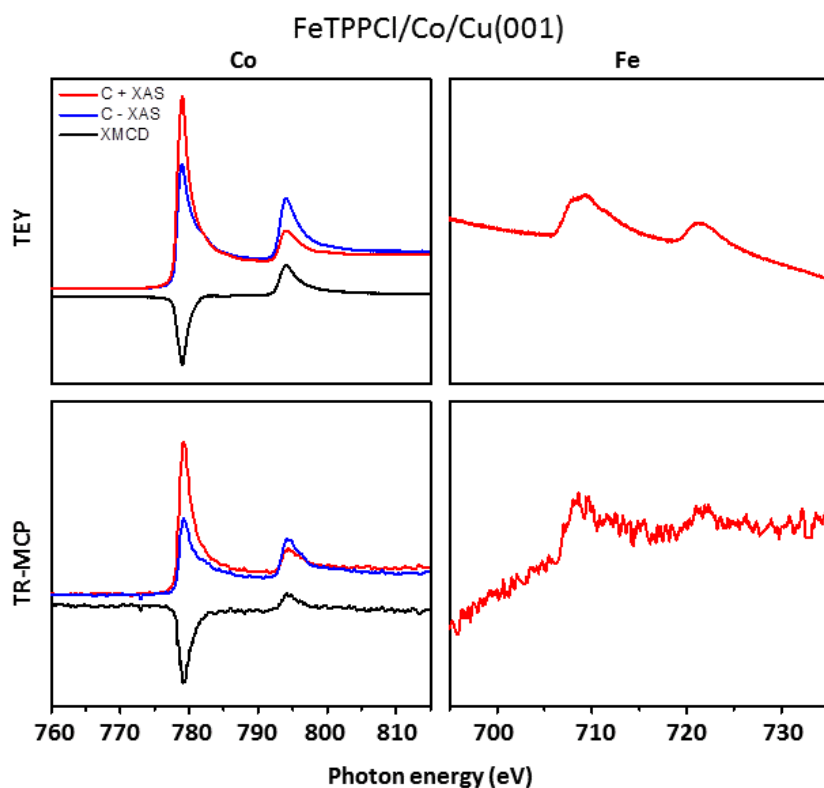


Figure 3.4.4 Comparison of Co and Fe $L_{2,3}$ spectra acquired on FeTPPCI molecules adsorbed on Co in TEY and TR-XAS mode

3.4.2 PULSE-VALVE MOLECULAR DEPOSITION FROM SOLUTIONS

In the field of surface science, thermal evaporation is the most commonly used method for preparation of well-defined films. This is possible for smaller and thermally stable molecules, but it is a big issue if the molecules are thermally instable. Difficulties and limitations in preparing single layered samples of robust SMM molecules spurred the use of Single Ion Magnets (SIMs) and paramagnetic molecules that were easy to handle. In order to avoid problems with the thermal decomposition of molecules, several groups created ordered monolayers in UHV from solutions by Electron-Spray Ion Beam Deposition (ES-IBD)^{8,184,185} or even less invasive Pulse Valve Deposition^{186–190}. The latter was also in our case a viable option for deposition of the special type of molecules described in Section 3.2.1 that were proven to be not suitable for thermal evaporation. In the pulse valve deposition technique, the desired molecules are injected into vacuum and onto the sample directly from solution through a small, needle-controlled orifice. Part of the solvent evaporates immediately when entering the vacuum, while the rest of it is removed from the sample by subsequent annealing^{188,189}. The principle of the method is rather simple, but it is compromised by several difficulties that will be here discussed. Previous applications were mostly using inert substrates such as Au(111), Si(111) and Cu(111), while we had the intention of using highly reactive Co/Cu(001) as well.



Figure 3.4.5 Picture of commercial pulse valve as received from company (Parker Inc)

The first encountered problem was the compatibility with UHV system. Namely, most commonly used pulse valves (Figure 3.4.5) - Parker Inc) are produced for operation with normal vacuum system, thus with a small o-ring at the connecting flange, rendering huge leaks into UHV (it was not possible to achieve pressure better than 7×10^{-7} mbar) so adaptation was required to make it compatible with UHV parts. This was achieved by welding the standard pulse valve to CF40 flange that

is then compatible with the system and afterwards the system was easily reaching 10^{-10} mbar range.

Selecting the suitable solvent for the tests was the next important issue as it needs to fulfill several requirements. First, the molecules of interest shall be soluble in the particular solvent to be able to use it at the first place. Next, the chosen solvent should have a high vapor pressure such that evaporation in vacuum is favored. The solvent shouldn't interact strongly neither with the substrate nor with the molecules of interest, as this would produce difficulties for its removal upon deposition. Ideally, it should contain an element that is not present in the molecules so that it is easier to identify it and monitor the cleaning process by means of XPS. For the selection, extensive literature research (e.g.¹⁹¹), extensive discussions with the chemistry partners, but also several trial-error experiments were performed. The two final candidates, that were later used for the experiments described in this thesis were dichloromethane-DCM and metyl-tertbutylether-MTBE (in some cases, alternative diethylether-DE was used).

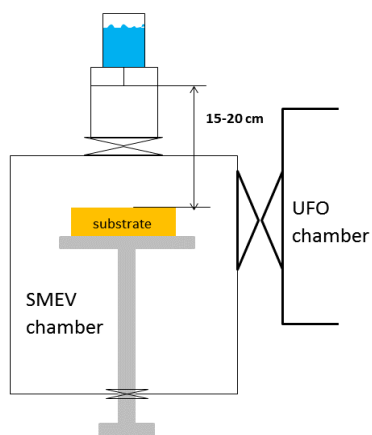


Figure 3.4.6. Schematic representation of pulse valve position in the SMEV chamber of Surface science lab

As it has been mentioned in Section 2.7, for the sample preparation, a clean sample or a sample with a deposited magnetic film was placed on a movable stage in the chamber for pulse valve deposition (SMEV from schematic in Figure 2.1a)). Here it was positioned 15-20 cm away from the inner orifice of the pulse valve (Figure 3.4.6). As evidenced in the schematic representation at Figure 3.4.6, the pulse valve was attached to the chamber where sample was held by a gate valve. The pulse valve had to be prefilled with the solution of concern to the experiment. This procedure involved several pulses with the gate closed to avoid the uncalibrated deposition of solvent/air onto the sample. The gate has been opened only as everything was ready for deposition and has been kept open only during the process. This improved pressure recovery and reduced the exposure of the sample to higher pressure for a more extended period of

time. The base pressure in the chamber where the sample was kept was in the 10^{-9} - 10^{-10} mbar range, while it was reaching $>10^{-2}$ mbar for a short time as the orifice was opened but recovered immediately to 10^{-7} - 10^{-8} mbar. The sample was afterwards moved to the XPS chamber where spectra were acquired before and after every step of stepwise annealing to remove the solvent. It was found that 6 pulses of 0.1s duration followed by annealing to around 550-600K are producing ML coverages of the investigated molecules. As we used ferromagnetic substrates, we planned to use the less reactive O/Co to reduce the amount of contaminations expected to occur as a side effect during the deposition. Interestingly, upon annealing process used to remove solvent, we observed that also oxygen from functionalization was removed, which was not the case when the same sample was heated to the same temperatures without prior deposition of molecules from the pulse valve. An example of this process reflected in O1s, Co2p, N1s and C1s XPS spectra of clean O/Co (black lines), O/Co after pulse valve deposition (red lines), and one after annealing (blue lines) is shown in Figure 3.4.7.

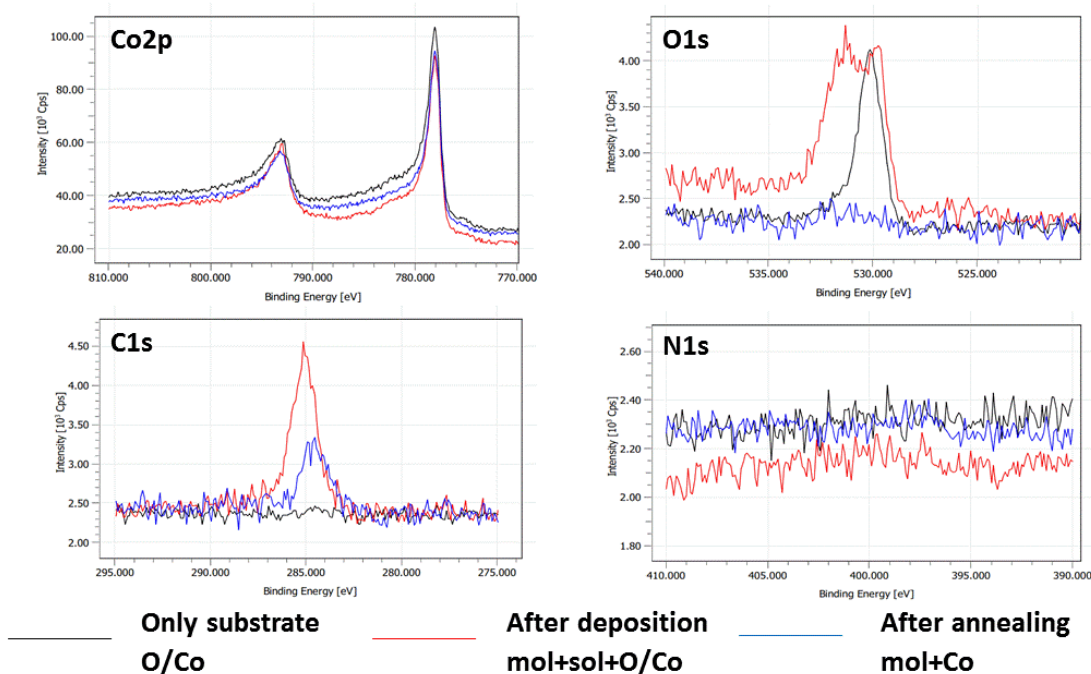


Figure 3.4.7 Example O1s, Co2p, N1s and C1s XPS spectra of clean O/Co (black lines), O/Co after pulse valve deposition of porphyrin molecules dissolved in MTBE (red lines), and after annealing for solvent desorption (blue lines). The clear decrease is visible in C1s spectra, while also O1s is reduced almost completely – also the O from surface functionalization is removed.

Additionally, we wanted to test the magnetic properties of MnTPPCI and FeTPPCI molecules deposited by pulse valve deposition on Co (starting from O/Co) and compare these to the ones of sublimed molecules on clean Co. Comparison of these is showed in Figure 3.4.8, where the same XAS/XMCD features are visible in both cases. To our knowledge, this is the first example of such molecules deposited on Co substrate in a way different than sublimation as magnetic properties of the substrate were easily destroyed otherwise.

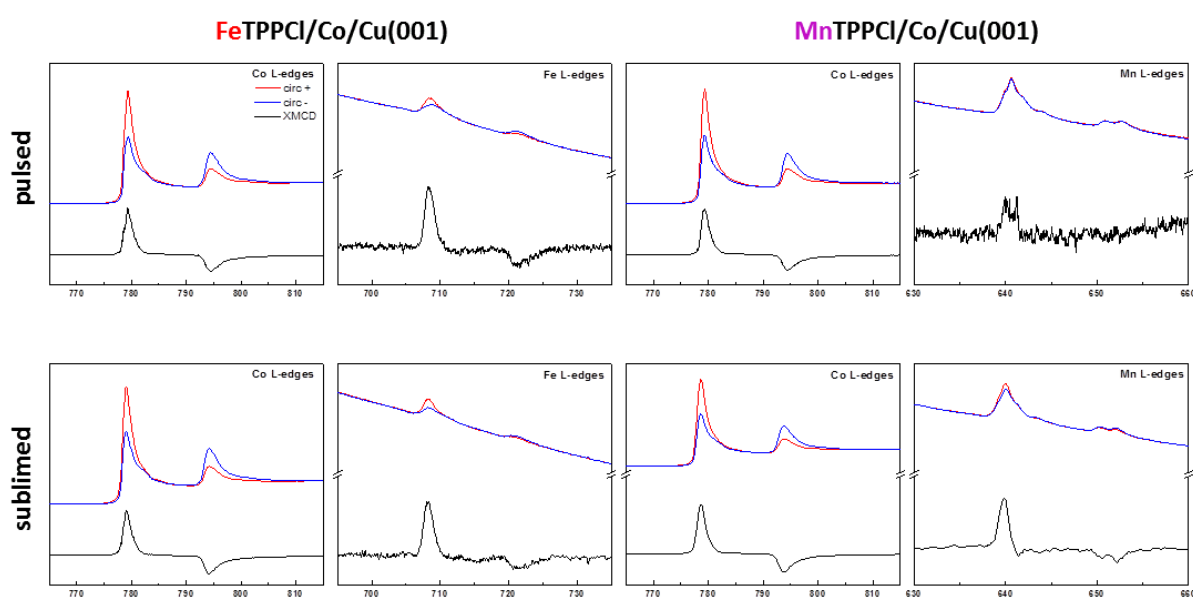


Figure 3.4.8 Comparison of room temperature XAS and XMCD spectra obtained at Co, Fe and Mn L_{3,2} edges on ~1ML of Fe(Mn)TPPCI molecules on ferromagnetic Co film where molecules were deposited by pulse injection technique (first row) and by thermal evaporation (second row). The XAS shapes of molecules look identical, and it is evidenced that they are FM coupled in both cases

Chapter 4

CONCLUSIONS AND PROSPECTS

In this thesis different combinations of spin-bearing square planar molecules and carefully selected surface substrates have been investigated aiming to answer scientific questions related to low dimensional magnetism. Also the aim is to gain control over these very interesting and functional material architectures for their potential application in quantum devices. Unraveling the subtle interplay of the spin dependent electronic and chemical interactions involved at these designer nanomaterials, their interfaces and surfaces, provides a necessary step towards gaining control over property prediction and rational material design. Thereby I have been working on a fascinating scientific goal geared towards future implementation which spans across several aspects of molecular magnetism like i) novel spin architectures, ii) intra and intermolecular interactions, iii) novel controls to tune and iv) characterize the interactions in these innovative materials often also called 'quantum materials'. During the journey of my thesis I have used a unique collection of local probing and X-ray based techniques grace to the key role that the University of Basel played in the early stages of Scanning Probe based nanosciences and to the unique experimental endstations implemented at the Swiss Light Source which allow for the in depth investigation of electronic, magnetic and structural properties at surfaces. While significant progress has been obtained, it is also important to recognize that every progress in scientific

understanding or technological control raises more new questions and opportunities such that at all instances it is motivating to proceed and difficult to stop.

By studying the magnetism of Cr-phthalocyanine molecules supported on several different ferromagnetic and non-magnetic substrates a very versatile behavior was observed. On the substrates where easy magnetization axes were matching the anisotropy of the molecule, stronger interactions were observed than in the case of misalignment of these axes. By introducing O as a spacer mediating the interactions, the interaction pathways have been modified and enhanced in the direction of the O orientation, i.e. out of plane. The investigation of Cr-phthalocyanines on Au(111) also revealed that these molecules can take a very strongly anisotropic magnetization by their specific interaction with this substrate. At the moment, the origin of this anisotropy is not completely understood. As cited at the beginning of this thesis, the history of science shows that theories are perishable. In order to answer scientific questions that are puzzling, we have to question the integrity of currently established concepts and theories towards their replacement or refinement. The unexpected and unexpectedly broad range of magnetization of CrPc may provide such a case where at least the interdependence of the surface molecular interaction and the electronic and magnetic anisotropy in presence also of emerging hybrid states may need to be refined. Theoretical treatment in the framework of DFT+U would facilitate deeper insight. Multiplet calculations, in addition, would help us to estimate the intensity of the dipolar contribution to the spin moment and its angular dependence, in order to identify the origin of high anisotropy.

The investigations on Pb(111) demonstrate the importance of X-ray investigations to complement to local probe investigations of spin systems interacting with the peculiar electronic system of a superconductor. We have observed here that in a series of 3d-metal phthalocyanine molecules adsorbed on Pb(111) only CrPc and MnPc show an XMCD signal, while all the other magnetic moments were quenched by the interaction with the substrate. Moreover, in the case of the quenched XMCD signals, a significant XAS shift was observed, most probably due to a charge transfer. It was also shown in our work that some of the properties of the system do not depend on whether the system is or is not in the

superconducting phase rendering the investigations with X-rays more important. On the other hand it would be interesting to probe the interaction of CrPc molecules with Pb(111) in its normal and superconducting state by local probe techniques as interesting quantum phenomena had been demonstrated for ad-MnPc. It is possible that CrPc would show a similar behavior so it represents a strong candidate for future investigation. Other investigations could involve thin layers of Pb(111) to increase the critical field and to probe the interplay of oriented spins and superconductivity.

In the experiments with triply fused bisporphyrin molecules we have observed that in the bulk form of the homometalic MnMn variant there is magnetic remanence. The measurement has been repeated with increasing precaution and against numerous references to rule out possible detrimental side effects of another material in the experimental setup. Additionally, the origin of this effect is not expected to be lying in intermolecular interactions as these big and bulky molecules are forming amorphous and thus disordered solid phases. We take this as evidence for the intramolecular origin of this magnetism. Further, pilot experiments have been performed where these molecules were deposited on Co substrates. We clearly observe their magnetic coupling up to room temperature and above and therefore demonstrated that they provide a new class of a spin bearing molecular building block containing two spin centers. These are further tunable by chemical means, in particular by a plethora of ion exchange and substitution techniques established for porphyrins. It will be also most interesting to see how the molecules that showed remanence in the bulk would behave on different non-magnetic substrates, for example Au(111), Ag(111) or some other ones.

Following our recent observation of long range 2D ferrimagnetic ordering in heteromolecular network of Fe and Mn phthalocyanine molecules supported on Au(111), we further looked into the interactions of these molecules with the substrate by means of ARPES. At a second stage we have been screening the other possible 2D network combinations of 3d metallo-phthalocyanines and trying to identify magnetic ordering. We have discussed the results in view of the 3d orbital symmetries of the different metals and recognized the importance of their filling for promoting interactions via the electrons in the

Au(111) surface in the framework of RKKY interaction. Coincidentally, the very first system we had investigated was the only suitable one to exhibit long-range ordering, -- at least within the temperature range of ~ 2 K, which we can currently investigate.

In the multilayer systems we intended to investigate for the possibility of a more complex inter-molecular interaction, we observed that molecular exchange happens in vertical direction leading to the reorganization of layers. We investigated this surprising phenomenon and assigned it to adsorption energy differences i.e. to the advantage of MnPc interacting directly, possibly by a (partial) charge transfer with the metallic bottom substrate. This effect also causes an asymmetry in the mixing of heteromolecular layers as one of the components will be pinned to the substrate. This needs to be taken into account for the on-surface metalation reactions or if the spintronic devices are designed.

Although the use of chemical stimuli was not new for investigating and tuning the magnetic moment of molecules interacting with metallic substrates, we have used a different and less toxic ligand compared to the earlier used NO or CO. Also here we reported on the alterations of the spin states of various phthalocyanine molecules by their exposure to molecular and atomic hydrogen. In the former case, this process is completely reversible, while in the latter case irreversible changes of both the spin state of the metal center and the molecules itself have been observed. We have used this ligation process for several processes then – for the tuning of the magnetic anisotropy of CrPc molecules, for inducing spin in quenched CoPc molecules or for the reversible switching of the previously mentioned ferrimagnetic coassembly. Additionally, we have observed a huge change in the XMCD signal of the MnPc molecules upon ligation. This latter effect asks for a stringent quantitative interpretation as it can be potentially used in gas sensors or in similar applications.

Also, the ability to functionalize a Co surface with either N or Cl adlayers has been demonstrated. Here, X-ray Photoelectron Diffraction has been employed to precisely determine the interatomic distances in the created functionalized surfaces. This allows for predicting the properties of adsorbed molecules, in particular the strength of their magnetic exchange interaction with the substrate. It also demonstrates the advantage of the XPD technique - with its proven superiority in comparison to STM and/or LEED or other surface diffraction

techniques for determining interatomic distances. It is grace to the element and chemical sensitivity together with the ability to investigate the structures or atoms hidden under the surface which makes the technique so powerful and important.

Further on, we have adapted a detector that is commonly used in time-of-flight mass spectrometry for acquiring fast, time-resolved XAS signals at the SIM beamline of the SLS. This is achieved by taking advantage of the temporal structure of the SLS - it focusses on the acquisition of signals from a single isolated bunch of electrons from the SLS. The setup has been successfully tested and it is ready for TR-XAS or pump-probe experiments with a suitable system. It demonstrates also how collaborative work at the SLS leads to knowledge transfer from one beamline to another beamline as well as in exchange with users.

In the last part it is shown how we successfully implemented the technique of deposition of large non-sublimable molecules into UHV directly from solution - this is in turn how we deposited investigated tf-P in a first place. The comparison of XAS/XMCD data on MnTPPCI and FeTPPCI molecules deposited by sublimation and via pulse valve on Co film showed no apparent differences. The developed technique, however, is not limited to these systems and can be also used for nanoparticles or other large systems.

As it was said in a beginning, this thesis represents a humble contribution to the world of molecular magnetism in the form of smaller puzzle pieces of a greater image.

BIBLIOGRAPHY

1. Capri, A. Z. *Quips, quotes, and quanta: an anecdotal history of physics*. (World Scientific, 2007).
2. *Dynamic fields and waves*. (Inst. of Physics Publ, 2000).
3. Waldrop, M. M. The chips are down for Moore's law. *Nature* **530**, 144–147 (2016).
4. *Magnetism*. (Springer Berlin Heidelberg, 2006).
5. Caneschi, A. *et al.* Alternating current susceptibility, high field magnetization, and millimeter band EPR evidence for a ground $S = 10$ state in $[\text{Mn}_{12}\text{O}_{12}(\text{CH}_3\text{COO})_{16}(\text{H}_2\text{O})_4] \cdot 2\text{CH}_3\text{COOH} \cdot 4\text{H}_2\text{O}$. *J. Am. Chem. Soc.* **113**, 5873–5874 (1991).
6. Sessoli, R., Gatteschi, D., Caneschi, A. & Novak, M. A. Magnetic bistability in a metal-ion cluster. *Nature* **365**, 141–143 (1993).
7. Milios, C. J. *et al.* A Record Anisotropy Barrier for a Single-Molecule Magnet. *J. Am. Chem. Soc.* **129**, 2754–2755 (2007).
8. Kahle, S. *et al.* The Quantum Magnetism of Individual Manganese-12-Acetate Molecular Magnets Anchored at Surfaces. *Nano Lett.* **12**, 518–521 (2012).
9. Dreiser, J. *et al.* X-ray induced demagnetization of single-molecule magnets. *Appl. Phys. Lett.* **105**, 032411 (2014).
10. Westerström, R. *et al.* An Endohedral Single-Molecule Magnet with Long Relaxation Times: $\text{DySc}_2\text{N}@\text{C}_{80}$. *J. Am. Chem. Soc.* **134**, 9840–9843 (2012).
11. Westerström, R. *et al.* Surface Aligned Magnetic Moments and Hysteresis of an Endohedral Single-Molecule Magnet on a Metal. *Phys. Rev. Lett.* **114**, (2015).
12. Bogani, L. & Wernsdorfer, W. Molecular spintronics using single-molecule magnets. *Nat. Mater.* **7**, 179–186 (2008).
13. Dreiser, J. Molecular lanthanide single-ion magnets: from bulk to submonolayers. *J. Phys. Condens. Matter* **27**, 183203 (2015).
14. Dreiser, J. *et al.* Out-of-Plane Alignment of Er(trensal) Easy Magnetization Axes Using Graphene. *ACS Nano* **10**, 2887–2892 (2016).
15. Wäckerlin, C. *et al.* Giant Hysteresis of Single-Molecule Magnets Adsorbed on a Nonmagnetic Insulator. *Adv. Mater.* **28**, 5195–5199 (2016).
16. Gambardella, P. Giant Magnetic Anisotropy of Single Cobalt Atoms and Nanoparticles. *Science* **300**, 1130–1133 (2003).
17. Scheybal, A. *et al.* Induced magnetic ordering in a molecular monolayer. *Chem. Phys. Lett.* **411**, 214–220 (2005).
18. Lodi Rizzini, A. *et al.* Coupling of single, double, and triple-decker metal-phthalocyanine complexes to ferromagnetic and antiferromagnetic substrates. *Surf. Sci.* **630**, 361–374 (2014).
19. Wende, H. *et al.* Substrate-induced magnetic ordering and switching of iron porphyrin molecules. *Nat. Mater.* **6**, 516–520 (2007).
20. Bernien, M. *et al.* Fe-porphyrin monolayers on ferromagnetic substrates: Electronic structure and magnetic coupling strength. *Phys. Rev. B* **76**, (2007).
21. Wäckerlin, C. *et al.* Controlling spins in adsorbed molecules by a chemical switch. *Nat. Commun.* **1**, 1–7 (2010).
22. Bernien, M. *et al.* Tailoring the Nature of Magnetic Coupling of Fe-Porphyrin Molecules to Ferromagnetic Substrates. *Phys. Rev. Lett.* **102**, (2009).
23. Chylarecka, D. *et al.* Self-Assembly and Superexchange Coupling of Magnetic Molecules on Oxygen-Reconstructed Ferromagnetic Thin Film. *J. Phys. Chem. Lett.* **1**, 1408–1413 (2010).
24. Hermanns, C. F. *et al.* Magnetic Coupling of Porphyrin Molecules Through Graphene. *Adv. Mater.* **25**, 3473–3477 (2013).

25. Girovsky, J. *et al.* Antiferromagnetic coupling of Cr-porphyrin to a bare Co substrate. *Phys. Rev. B* **90**, (2014).
26. Eguchi, K., Takagi, Y., Nakagawa, T. & Yokoyama, T. Magnetic Interactions of Vanadyl Phthalocyanine with Ferromagnetic Iron, Cobalt, and Nickel Surfaces. *J. Phys. Chem. C* **118**, 17633–17637 (2014).
27. Stepanow, S. *et al.* Mixed-valence behavior and strong correlation effects of metal phthalocyanines adsorbed on metals. *Phys. Rev. B* **83**, (2011).
28. Gargiani, P. *et al.* Spin and orbital configuration of metal phthalocyanine chains assembled on the Au(110) surface. *Phys. Rev. B* **87**, (2013).
29. Minamitani, E. *et al.* Symmetry-Driven Novel Kondo Effect in a Molecule. *Phys. Rev. Lett.* **109**, (2012).
30. Mugarza, A. *et al.* Electronic and magnetic properties of molecule-metal interfaces: Transition-metal phthalocyanines adsorbed on Ag(100). *Phys. Rev. B* **85**, (2012).
31. Zhao, A. Controlling the Kondo Effect of an Adsorbed Magnetic Ion Through Its Chemical Bonding. *Science* **309**, 1542–1544 (2005).
32. Ohta, N., Arafune, R., Tsukahara, N., Kawai, M. & Takagi, N. Enhancement of Inelastic Electron Tunneling Conductance Caused by Electronic Decoupling in Iron Phthalocyanine Bilayer on Ag(111). *J. Phys. Chem. C* **117**, 21832–21837 (2013).
33. Gopakumar, T. G. *et al.* Coverage-Driven Electronic Decoupling of Fe-Phthalocyanine from a Ag(111) Substrate. *J. Phys. Chem. C* **115**, 12173–12179 (2011).
34. Krull, C. *Electronic structure of metal phthalocyanines on Ag(100)*. (2014).
35. Zhang, Q., Kuang, G., Pang, R., Shi, X. & Lin, N. Switching Molecular Kondo Effect via Supramolecular Interaction. *ACS Nano* **9**, 12521–12528 (2015).
36. Liu, L. *et al.* Reversible Single Spin Control of Individual Magnetic Molecule by Hydrogen Atom Adsorption. *Sci. Rep.* **3**, (2013).
37. Yang, K. *et al.* Reversible Achiral-to-Chiral Switching of Single Mn–Phthalocyanine Molecules by Thermal Hydrogenation and Inelastic Electron Tunneling Dehydrogenation. *ACS Nano* **8**, 2246–2251 (2014).
38. Tsukahara, N., Minamitani, E., Kim, Y., Kawai, M. & Takagi, N. Controlling orbital-selective Kondo effects in a single molecule through coordination chemistry. *J. Chem. Phys.* **141**, 054702 (2014).
39. Wäckerlin, C. *et al.* Two-Dimensional Supramolecular Electron Spin Arrays. *Adv. Mater.* **25**, 2404–2408 (2013).
40. Wäckerlin, C. *et al.* Ammonia Coordination Introducing a Magnetic Moment in an On-Surface Low-Spin Porphyrin. *Angew. Chem. Int. Ed.* **52**, 4568–4571 (2013).
41. Wäckerlin, C. *et al.* On-surface coordination chemistry of planar molecular spin systems: novel magnetochemical effects induced by axial ligands. *Chem. Sci.* **3**, 3154 (2012).
42. Stróżecka, A., Soriano, M., Pascual, J. I. & Palacios, J. J. Reversible Change of the Spin State in a Manganese Phthalocyanine by Coordination of CO Molecule. *Phys. Rev. Lett.* **109**, (2012).
43. Seufert, K. *et al.* Cis-dicarbonyl binding at cobalt and iron porphyrins with saddle-shape conformation. *Nat. Chem.* **3**, 114–119 (2011).
44. Krull, C., Robles, R., Mugarza, A. & Gambardella, P. Site- and orbital-dependent charge donation and spin manipulation in electron-doped metal phthalocyanines. *Nat. Mater.* **12**, 337–343 (2013).
45. Liu, L. *et al.* Revealing the Atomic Site-Dependent g Factor within a Single Magnetic Molecule via the Extended Kondo Effect. *Phys. Rev. Lett.* **114**, (2015).
46. Jiang, Y. H. *et al.* Self-Assembly of Metal Phthalocyanines on Pb(111) and Au(111) Surfaces at Submonolayer Coverage. *J. Phys. Chem. C* **115**, 21750–21754 (2011).

47. Minamitani, E., Fu, Y.-S., Xue, Q.-K., Kim, Y. & Watanabe, S. Spatially extended underscreened Kondo state from collective molecular spin. *Phys. Rev. B* **92**, (2015).
48. Wäckerlin, C. *et al.* Strong antiferromagnetic exchange between manganese phthalocyanine and ferromagnetic europium oxide. *Chem Commun* **51**, 12958–12961 (2015).
49. Heinrich, B. W., Braun, L., Pascual, J. I. & Franke, K. J. Protection of excited spin states by a superconducting energy gap. *Nat. Phys.* **9**, 765–768 (2013).
50. Hatter, N., Heinrich, B. W., Ruby, M., Pascual, J. I. & Franke, K. J. Magnetic anisotropy in Shiba bound states across a quantum phase transition. *Nat. Commun.* **6**, 8988 (2015).
51. Girovsky, J. *et al.* Long-range ferrimagnetic order in a two-dimensional supramolecular Kondo lattice. *Nat. Commun.* **8**, 15388 (2017).
52. Tsukahara, N. *et al.* Evolution of Kondo Resonance from a Single Impurity Molecule to the Two-Dimensional Lattice. *Phys. Rev. Lett.* **106**, (2011).
53. Oura, K., Katayama, M., Lifshits, V. G., Saranin, A. A. & Zotov, A. V. *Surface Science An Introduction*. (Springer Berlin Heidelberg, 2003).
54. *Surface Analysis— The Principal Techniques*. (John Wiley & Sons, Ltd, 2009). doi:10.1002/9780470721582
55. Surface Science Lab and Vacuum suitcase. Available at: <https://www.psi.ch/lmn/surface-science-lab>.
56. *Synchrotron radiation*. (Springer, 2014).
57. Watts, J. F. & Wolstenholme, J. *An introduction to surface analysis by XPS and AES*. (J. Wiley, 2003).
58. Seah, M. P. & Dench, W. A. Quantitative electron spectroscopy of surfaces: A standard data base for electron inelastic mean free paths in solids. *Surf. Interface Anal.* **1**, 2–11 (1979).
59. van der Heide, P. *X-Ray Photoelectron Spectroscopy: An Introduction to Principles and Practices*. (John Wiley & Sons, Inc., 2011). doi:10.1002/9781118162897
60. Braun, S., Salaneck, W. R. & Fahlman, M. Energy-Level Alignment at Organic/Metal and Organic/Organic Interfaces. *Adv. Mater.* **21**, 1450–1472 (2009).
61. Ishii, H., Sugiyama, K., Ito, E. & Seki, K. Energy Level Alignment and Interfacial Electronic Structures at Organic/Metal and Organic/Organic Interfaces. *Adv. Mater.* **11**, 605–625 (1999).
62. *Strongly correlated systems: experimental techniques*. (Springer, 2015).
63. Jacob's group. XPS scheme. Available at: <https://jacobs.physik.uni-saarland.de/home/index.php?page=forschung/UHV-Lab-1>.
64. Kuznetsov, M. V., Ogorodnikov, I. I. & Vorokh, A. S. X-Ray photoelectron diffraction and photoelectron holography as methods for investigating the local atomic structure of the surface of solids. *Russ. Chem. Rev.* **83**, 13–37 (2014).
65. Muntwiler, M. *et al.* Determining adsorbate structures from substrate emission X-ray photoelectron diffraction. *Surf. Sci.* **472**, 125–132 (2001).
66. Winkelmann, A., Fadley, C. S. & Garcia de Abajo, F. J. High-energy photoelectron diffraction: model calculations and future possibilities. *New J. Phys.* **10**, 113002 (2008).
67. Groot, F. de. Multiplet effects in X-ray spectroscopy. *Coord. Chem. Rev.* **249**, 31–63 (2005).
68. Stöhr, J. *NEXAFS Spectroscopy*. (Springer Berlin Heidelberg, 1992).
69. Arenholz, E. Magnetism as seen with X-rays. (2016).
70. van der Laan, G. & Figueroa, A. I. X-ray magnetic circular dichroism—A versatile tool to study magnetism. *Coord. Chem. Rev.* **277–278**, 95–129 (2014).
71. Piamonteze, C., Miedema, P. & de Groot, F. M. F. Accuracy of the spin sum rule in XMCD for the transition-metal L edges from manganese to copper. *Phys. Rev. B* **80**, (2009).
72. Bernien, M. X-Ray absorption spectroscopy of Fe complexes on surfaces. (FREIE UNIVERSITÄT, 2009).

73. Chen, C. J. *Introduction to Scanning Tunneling Microscopy*. (Oxford University Press, 2007). doi:10.1093/acprof:oso/9780199211500.001.0001
74. Foster, A. & Hofer, W. *Scanning Probe Microscopy Atomic Scale Engineering by Forces and Currents*. (Springer Science+Business Media, LLC, 2006).
75. STM illustration. www.fhi-berlin.mpg.de/pc/PCres_methods.html and doi:10.1142/9789814390460_0002.
76. Kouwenhoven, L. & Glazman, L. Revival of the Kondo effect. *Phys. World* **14**, 33–38 (2001).
77. Pawlak, R. *et al.* Probing atomic structure and Majorana wavefunctions in mono-atomic Fe chains on superconducting Pb surface. *Npj Quantum Inf.* **2**, (2016).
78. Nowakowska, S. *et al.* Configuring Electronic States in an Atomically Precise Array of Quantum Boxes. *Small* **12**, 3757–3763 (2016).
79. Heinrich, A. J. Single-Atom Spin-Flip Spectroscopy. *Science* **306**, 466–469 (2004).
80. Bode, M. Spin-polarized scanning tunnelling microscopy. *Rep. Prog. Phys.* **66**, 523–582 (2003).
81. Wiesendanger, R. Spin mapping at the nanoscale and atomic scale. *Rev. Mod. Phys.* **81**, 1495–1550 (2009).
82. Franke, K. J., Schulze, G. & Pascual, J. I. Competition of Superconducting Phenomena and Kondo Screening at the Nanoscale. *Science* **332**, 940–944 (2011).
83. Natterer, F. D. *et al.* Reading and writing single-atom magnets. *Nature* **543**, 226–228 (2017).
84. Bochi, G. *et al.* Magnetic anisotropy in epitaxial Ni/Cu(001) thin films: Effects of misfit strain on perpendicular magnetic anisotropy (abstract). *J. Appl. Phys.* **75**, 6430–6430 (1994).
85. Vaz, C. A. F. & Bland, J. A. C. Dependence of the coercive field on the Cu overlayer thickness in thin Co/Cu(001) and Ni/Cu(001) fcc epitaxial films. *J. Appl. Phys.* **89**, 7374–7376 (2001).
86. Ballav, N., Wäckerlin, C., Siewert, D., Oppeneer, P. M. & Jung, T. A. Emergence of On-Surface Magnetochemistry. *J. Phys. Chem. Lett.* **4**, 2303–2311 (2013).
87. Conde, A., Cristóbal, A. B., Fuentes, G., Tate, T. & de Damborenea, J. Surface analysis of electrochemically stripped CrN coatings. *Surf. Coat. Technol.* **201**, 3588–3595 (2006).
88. Duan, X. F., Mi, W. B., Guo, Z. B. & Bai, H. L. A comparative study of transport properties in polycrystalline and epitaxial chromium nitride films. *J. Appl. Phys.* **113**, 023701 (2013).
89. *Solid surface physics*. (Springer, 1979).
90. Kastanas, G. N. & Koel, B. E. Interaction of Cl₂ with the Au(111) surface in the temperature range of 120 to 1000 K. *Appl. Surf. Sci.* **64**, 235–249 (1993).
91. Theil, C., van Elp, J. & Folkmann, F. Ligand field parameters obtained from and chemical shifts observed at the Cr L 2, 3 edges. *Phys. Rev. B* **59**, 7931–7936 (1999).
92. Baker, A. A. *et al.* Magnetic proximity-enhanced Curie temperature of Cr-doped Bi₂Se₃ thin films. *Phys. Rev. B* **92**, (2015).
93. Stepanow, S. *et al.* Spin Tuning of Electron-Doped Metal–Phthalocyanine Layers. *J. Am. Chem. Soc.* **136**, 5451–5459 (2014).
94. Carra, P., Thole, B. T., Altarelli, M. & Wang, X. X-ray circular dichroism and local magnetic fields. *Phys. Rev. Lett.* **70**, 694–697 (1993).
95. Thole, B. T., Carra, P., Sette, F. & van der Laan, G. X-ray circular dichroism as a probe of orbital magnetization. *Phys. Rev. Lett.* **68**, 1943–1946 (1992).
96. Goering, E. X-ray magnetic circular dichroism sum rule correction for the light transition metals. *Philos. Mag.* **85**, 2895–2911 (2005).
97. Lisi, S. *et al.* Graphene-Induced Magnetic Anisotropy of a Two-Dimensional Iron Phthalocyanine Network. *J. Phys. Chem. Lett.* **6**, 1690–1695 (2015).
98. Hu, J. & Wu, R. Control of the Magnetism and Magnetic Anisotropy of a Single-Molecule Magnet with an Electric Field. *Phys. Rev. Lett.* **110**, (2013).

99. Gambardella, P. Giant Magnetic Anisotropy of Single Cobalt Atoms and Nanoparticles. *Science* **300**, 1130–1133 (2003).
100. Bing, L. *et al.* Large Magnetic Anisotropy of an Iron-Porphyrin Complex on Metal Substrate. *arXiv.org* doi:arXiv:1707.05434 [cond-mat.mes-hall]
101. Klanke, J. *et al.* Beyond the Heisenberg Model: Anisotropic Exchange Interaction between a Cu-Tetraazaporphyrin Monolayer and Fe₃O₄ (100). *Phys. Rev. Lett.* **110**, (2013).
102. Pali, A. *et al.* Beyond the spin model: exchange coupling in molecular magnets with unquenched orbital angular momenta. *Chem. Soc. Rev.* **40**, 3130 (2011).
103. Lodi Rizzini, A. *et al.* Coupling Single Molecule Magnets to Ferromagnetic Substrates. *Phys. Rev. Lett.* **107**, (2011).
104. Hermanns, C. F. *et al.* Huge magnetically coupled orbital moments of Co porphyrin molecules and their control by CO adsorption. *Phys. Rev. B* **88**, (2013).
105. Tsukahara, N. *et al.* Adsorption-Induced Switching of Magnetic Anisotropy in a Single Iron(II) Phthalocyanine Molecule on an Oxidized Cu(110) Surface. *Phys. Rev. Lett.* **102**, (2009).
106. Bernien, M. *et al.* Tailoring the Nature of Magnetic Coupling of Fe-Porphyrin Molecules to Ferromagnetic Substrates. *Phys. Rev. Lett.* **102**, (2009).
107. Heinrich, B. W., Braun, L., Pascual, J. I. & Franke, K. J. Tuning the Magnetic Anisotropy of Single Molecules. *Nano Lett.* **15**, 4024–4028 (2015).
108. Matthias, B. T., Geballe, T. H. & Compton, V. B. Superconductivity. *Rev. Mod. Phys.* **35**, 1–22 (1963).
109. *Springer handbook of condensed matter and materials data: with 914 tables.* (Springer, 2005).
110. Teramura, Y., Tanaka, A., Thole, B. T. & Jo, T. Effect of Coulomb Interaction on the X-Ray Magnetic Circular Dichroism Spin Sum Rule in Rare Earths. *J. Phys. Soc. Jpn.* **65**, 3056–3059 (1996).
111. Ruby, M., Heinrich, B. W., Peng, Y., von Oppen, F. & Franke, K. J. Exploring a Proximity-Coupled Co Chain on Pb(110) as a Possible Majorana Platform. *Nano Lett.* **17**, 4473–4477 (2017).
112. Klinovaja, J., Stano, P., Yazdani, A. & Loss, D. Topological Superconductivity and Majorana Fermions in RKKY Systems. *Phys. Rev. Lett.* **111**, (2013).
113. Ménard, G. C. *et al.* Coherent long-range magnetic bound states in a superconductor. *Nat. Phys.* **11**, 1013–1016 (2015).
114. Bonifazi, D. *et al.* Supramolecular Patterned Surfaces Driven by Cooperative Assembly of C60 and Porphyrins on Metal Substrates. *Angew. Chem. Int. Ed.* **43**, 4759–4763 (2004).
115. Giovannetti, R. The Use of Spectrophotometry UV-Vis for the Study of Porphyrins. in *Macro To Nano Spectroscopy* (ed. Uddin, J.) (InTech, 2012). doi:10.5772/38797
116. Ryan, A. A. & Senge, M. O. Synthesis and Functionalization of Triply Fused Porphyrin Dimers: Triply Fused Porphyrin Dimers. *Eur. J. Org. Chem.* **2013**, 3700–3711 (2013).
117. Huheey, J. E., Keiter, E. A. & Keiter, R. L. *Inorganic chemistry: principles of structure and reactivity.* (HarperCollins College Publishers, 1993).
118. Grush, M. M. *et al.* Manganese L-Edge X-ray Absorption Spectroscopy of Manganese Catalase from *Lactobacillus plantarum* and Mixed Valence Manganese Complexes. *J. Am. Chem. Soc.* **118**, 65–69 (1996).
119. Nemrava, S. *et al.* Three Oxidation States of Manganese in the Barium Hexaferrite BaFe_{12-x}Mn_xO₁₉. *Inorg. Chem.* **56**, 3861–3866 (2017).
120. Diller, K. *et al.* Self-metalation of 2H-tetraphenylporphyrin on Cu(111): An x-ray spectroscopy study. *J. Chem. Phys.* **136**, 014705 (2012).
121. Chen, M. *et al.* Direct Synthesis of Nickel(II) Tetraphenylporphyrin and Its Interaction with a Au(111) Surface: A Comprehensive Study. *J. Phys. Chem. C* **114**, 9908–9916 (2010).

122. Mangione, G. *et al.* Electronic structure of CuTPP and CuTPP(F) complexes: a combined experimental and theoretical study II. *Phys Chem Chem Phys* **18**, 24890–24904 (2016).
123. Yamaguchi, Y. Theoretical study of two-dimensionally fused zinc porphyrins: DFT calculations. *Int. J. Quantum Chem.* **109**, 1584–1597 (2009).
124. Cho, H. S. *et al.* Photophysical Properties of Porphyrin Tapes. *J. Am. Chem. Soc.* **124**, 14642–14654 (2002).
125. Scheybal, A. *et al.* Induced magnetic ordering in a molecular monolayer. *Chem. Phys. Lett.* **411**, 214–220 (2005).
126. Wang, W. *et al.* Intramolecularly resolved Kondo resonance of high-spin Fe (II) -porphyrin adsorbed on Au (111). *Phys. Rev. B* **91**, (2015).
127. Fernández, J., Aligia, A. A. & Lobos, A. M. Valence fluctuations in a lattice of magnetic molecules: Application to iron(II) phthalocyanine molecules on Au(111). *EPL Europhys. Lett.* **109**, 37011 (2015).
128. Bartolomé, J., Monton, C. & Schuller, I. K. Magnetism of Metal Phthalocyanines. in *Molecular Magnets* (eds. Bartolomé, J., Luis, F. & Fernández, J. F.) 221–245 (Springer Berlin Heidelberg, 2014). doi:10.1007/978-3-642-40609-6_9
129. Henk, J., Hoesch, M., Osterwalder, J., Ernst, A. & Bruno, P. Spin–orbit coupling in the L-gap surface states of Au(111): spin-resolved photoemission experiments and first-principles calculations. *J. Phys. Condens. Matter* **16**, 7581–7597 (2004).
130. Ryu, H. *et al.* Photon energy dependent circular dichroism in angle-resolved photoemission from Au(111) surface states. *Phys. Rev. B* **95**, (2017).
131. Sachs, S. *et al.* Electronic structure at the perylene-tetracarboxylic acid dianhydride/Ag(111) interface studied with two-photon photoelectron spectroscopy. *J. Chem. Phys.* **131**, 144701 (2009).
132. Schwalb, C. H. *et al.* Electron Lifetime in a Shockley-Type Metal-Organic Interface State. *Phys. Rev. Lett.* **101**, (2008).
133. Ziroff, J., Gold, P., Bendounan, A., Forster, F. & Reinert, F. Adsorption energy and geometry of physisorbed organic molecules on Au(111) probed by surface-state photoemission. *Surf. Sci.* **603**, 354–358 (2009).
134. Nicoara, N., Román, E., Gómez-Rodríguez, J. M., Martín-Gago, J. A. & Méndez, J. Scanning tunneling and photoemission spectroscopies at the PTCDA/Au(111) interface. *Org. Electron.* **7**, 287–294 (2006).
135. Zaitsev, N. L., Nechaev, I. A., Echenique, P. M. & Chulkov, E. V. Transformation of the Ag(111) surface state due to molecule-surface interaction with ordered organic molecular monolayers. *Phys. Rev. B* **85**, (2012).
136. Tamai, A. *et al.* Electronic structure at the C 60 /metal interface: An angle-resolved photoemission and first-principles study. *Phys. Rev. B* **77**, (2008).
137. Caputo, M. *et al.* Manipulating the Topological Interface by Molecular Adsorbates: Adsorption of Co-Phthalocyanine on Bi₂Se₃. *Nano Lett.* **16**, 3409–3414 (2016).
138. Scheybal, A. *et al.* Modification of the Cu(110) Shockley surface state by an adsorbed pentacene monolayer. *Phys. Rev. B* **79**, (2009).
139. Bendounan, A. & Aït-Ouazzou, S. Role of the Shockley State in Doping of Organic Molecule Monolayer. *J. Phys. Chem. C* **120**, 11456–11464 (2016).
140. Lin, C.-F., Zhang, M., Liu, S.-W., Chiu, T.-L. & Lee, J.-H. High Photoelectric Conversion Efficiency of Metal Phthalocyanine/Fullerene Heterojunction Photovoltaic Device. *Int. J. Mol. Sci.* **12**, 476–505 (2011).
141. Varotto, A. *et al.* Phthalocyanine Blends Improve Bulk Heterojunction Solar Cells. *J. Am. Chem. Soc.* **132**, 2552–2554 (2010).

142. Imahori, H. & Fukuzumi, S. Porphyrin- and Fullerene-Based Molecular Photovoltaic Devices. *Adv. Funct. Mater.* **14**, 525–536 (2004).
143. Zysman-Colman, E. *et al.* Solution-Processable Silicon Phthalocyanines in Electroluminescent and Photovoltaic Devices. *ACS Appl. Mater. Interfaces* **8**, 9247–9253 (2016).
144. Jurow, M., Schuckman, A. E., Batteas, J. D. & Drain, C. M. Porphyrins as molecular electronic components of functional devices. *Coord. Chem. Rev.* **254**, 2297–2310 (2010).
145. Cinchetti, M., Dediu, V. A. & Hueso, L. E. Activating the molecular spininterface. *Nat. Mater.* **16**, 507–515 (2017).
146. Cho, W. J., Cho, Y., Min, S. K., Kim, W. Y. & Kim, K. S. Chromium Porphyrin Arrays As Spintronic Devices. *J. Am. Chem. Soc.* **133**, 9364–9369 (2011).
147. Majumdar, S. *et al.* COMPARATIVE STUDY OF SPIN INJECTION AND TRANSPORT IN Alq₃ AND Co–PHTHALOCYANINE-BASED ORGANIC SPIN VALVES. *SPIN* **04**, 1440009 (2014).
148. Barraud, C. *et al.* Phthalocyanine based molecular spintronic devices. *Dalton Trans* **45**, 16694–16699 (2016).
149. Gruber, M. *et al.* Exchange bias and room-temperature magnetic order in molecular layers. *Nat. Mater.* (2015). doi:10.1038/nmat4361
150. Beall, R. B. *et al.* Post-growth diffusion of Si in delta -doped GaAs grown by MBE. *Semicond. Sci. Technol.* **4**, 1171–1175 (1989).
151. Beall, R. B., Clegg, J. B. & Harris, J. J. Migration of Si in δ -doped GaAs. *Semicond. Sci. Technol.* **3**, 612–615 (1988).
152. Auwärter, W., Écija, D., Klappenberger, F. & Barth, J. V. Porphyrins at interfaces. *Nat. Chem.* **7**, 105–120 (2015).
153. de Wild, M. *et al.* A Novel Route To Molecular Self-Assembly: Self-Intermixed Monolayer Phases. *ChemPhysChem* **3**, 881–885 (2002).
154. Ozin, G. A. *et al.* Nanofabrication by self-assembly. *Mater. Today* **12**, 12–23 (2009).
155. Panighel, M. *et al.* Review of 2H-tetraphenylporphyrins metalation in ultra-high vacuum on metal surfaces. *J. Phys. Conf. Ser.* **470**, 012012 (2013).
156. Buchner, F. *et al.* Coordination of Iron Atoms by Tetraphenylporphyrin Monolayers and Multilayers on Ag(111) and Formation of Iron-Tetraphenylporphyrin. *J. Phys. Chem. C* **112**, 15458–15465 (2008).
157. Rochford, L. A., Ramadan, A. J., Woodruff, D. P., Heutz, S. & Jones, T. S. Ordered growth of vanadyl phthalocyanine (VOPc) on an iron phthalocyanine (FePc) monolayer. *Phys Chem Chem Phys* **17**, 29747–29752 (2015).
158. Thussing, S. & Jakob, P. Thermal Stability and Interlayer Exchange Processes in Heterolayers of CuPc and PTCDA on Ag(111). *J. Phys. Chem. C* **121**, 13680–13691 (2017).
159. Chen, M. *et al.* Coordination Reactions and Layer Exchange Processes at a Buried Metal–Organic Interface. *J. Phys. Chem. C* **118**, 8501–8507 (2014).
160. Wäckerlin, C. *et al.* Controlling spins in adsorbed molecules by a chemical switch. *Nat. Commun.* **1**, 1–7 (2010).
161. Wäckerlin, C. *et al.* Ammonia Coordination Introducing a Magnetic Moment in an On-Surface Low-Spin Porphyrin. *Angew. Chem. Int. Ed.* **52**, 4568–4571 (2013).
162. Zhong, J.-Q. *et al.* Reversible Tuning of Interfacial and Intramolecular Charge Transfer in Individual MnPc Molecules. *Nano Lett.* **15**, 8091–8098 (2015).
163. Kubas, G. J. Molecular hydrogen complexes: coordination of a σ bond to transition metals. *Acc. Chem. Res.* **21**, 120–128 (1988).
164. Maseras, F., Duran, M., Lledos, A. & Bertran, J. Molecular Hydrogen as a Ligand in Transition Metal Complexes. in *Theoretical and Computational Models for Organic Chemistry* (eds.

- Formosinho, S. J., Csizmadia, I. G. & Arnaut, L. G.) 375–396 (Springer Netherlands, 1991). doi:10.1007/978-94-011-3584-9_17
165. Wasserman, H. J., Kubas, G. J. & Ryan, R. R. Molecular hydrogen complexes of the transition metals. 2. Preparation, structure, and reactivity of $\text{W}(\text{CO})_3(\text{PCy}_3)_2$ and $\text{W}(\text{CO})_3(\text{P-iso-Pr}_3)_2$, $\eta^2\text{-H}_2$ complex precursors exhibiting metal...hydrogen-carbon interaction. *J. Am. Chem. Soc.* **108**, 2294–2301 (1986).
 166. Memmel, N. & Bertel, E. Role of Surface States for the Epitaxial Growth on Metal Surfaces. *Phys. Rev. Lett.* **75**, 485–488 (1995).
 167. Knorr, N. *et al.* Long-range adsorbate interactions mediated by a two-dimensional electron gas. *Phys. Rev. B* **65**, (2002).
 168. Nowakowski, J. *et al.* Porphyrin metalation providing an example of a redox reaction facilitated by a surface reconstruction. *Chem. Commun.* **49**, 2347 (2013).
 169. Nowakowski, J. *et al.* Probing the Reactivity of Functionalized Surfaces by Porphyrin Metalation. *ChemistrySelect* **1**, 891–895 (2016).
 170. Bernien, M. *et al.* Spin Crossover in a Vacuum-Deposited Submonolayer of a Molecular Iron(II) Complex. *J. Phys. Chem. Lett.* **3**, 3431–3434 (2012).
 171. Hong, S., Rahman, T. S., Ciftlikli, E. Z. & Hinch, B. J. Stress balance in nanopatterned N/Cu(001) surfaces. *Phys. Rev. B* **84**, (2011).
 172. Komori, F., Ohno, S. & Nakatsuji, K. Arrays of magnetic nanodots on nitrogen-modified Cu(001) surfaces. *J. Phys. Condens. Matter* **14**, 8177–8197 (2002).
 173. Getzlaff, M., Bode, M. & Wiesendanger, R. Surface Electronic Properties of Fe Nanoparticles on $c(2\times 2)\text{-N/Cu}(001)$. *Acta Phys. Pol. A* **104**, 327–335 (2003).
 174. Wang, L.-Q. *et al.* $c(2\times 2)\text{Cl/Cu}(001)$ adsorbate geometry and substrate-surface relaxation using low-temperature angle-resolved photoemission extended fine structure. *Phys. Rev. B* **44**, 1292–1305 (1991).
 175. Tolentino, H. C. N., De Santis, M., Gauthier, Y. & Langlais, V. Chlorine chemisorption on Cu(001) by surface X-ray diffraction: Geometry and substrate relaxation. *Surf. Sci.* **601**, 2962–2966 (2007).
 176. Jona, F., Westphal, D., Goldmann, A. & Marcus, P. M. A low-energy electron diffraction intensity analysis of $\text{Cu}(001)c(2\times 2)\text{-Cl}$. *J. Phys. C Solid State Phys.* **16**, 3001–3010 (1983).
 177. Fadley, C. S. Atomic-level characterization of materials with core- and valence-level photoemission: basic phenomena and future directions. *Surf. Interface Anal.* **40**, 1579–1605 (2008).
 178. Fasel, R. *et al.* Orientation of Adsorbed C₆₀ Molecules Determined via X-Ray Photoelectron Diffraction. *Phys. Rev. Lett.* **76**, 4733–4736 (1996).
 179. Treier, M. *et al.* Looking inside an endohedral fullerene: Inter- and intramolecular ordering of Dy₃N@C₈₀(I_h) on Cu(111). *Phys. Rev. B* **80**, (2009).
 180. Osterwalder, J. *et al.* Angle-scanned photoelectron diffraction. *Surf. Sci.* **331–333**, 1002–1014 (1995).
 181. García de Abajo, F. J., Van Hove, M. A. & Fadley, C. S. Multiple scattering of electrons in solids and molecules: A cluster-model approach. *Phys. Rev. B* **63**, (2001).
 182. Lima, F. A. *et al.* A high-repetition rate scheme for synchrotron-based picosecond laser pump/x-ray probe experiments on chemical and biological systems in solution. *Rev. Sci. Instrum.* **82**, 063111 (2011).
 183. Puzic, A. *et al.* Photon Counting System for Time-resolved Experiments in Multibunch Mode. *Synchrotron Radiat. News* **23**, 26–32 (2010).
 184. Rauschenbach, S. *et al.* Electrospray Ion Beam Deposition of Clusters and Biomolecules. *Small* **2**, 540–547 (2006).

-
185. Rinke, G. *et al.* Soft-landing electrospray ion beam deposition of sensitive oligoynes on surfaces in vacuum. *Int. J. Mass Spectrom.* **377**, 228–234 (2015).
 186. Tanaka, H. Scanning tunneling microscopy imaging and manipulation of DNA oligomer adsorbed on Cu(111) surfaces by a pulse injection method. *J. Vac. Sci. Technol. B Microelectron. Nanometer Struct.* **15**, 602 (1997).
 187. Kanno, T., Tanaka, H., Nakamura, T., Tabata, H. & Kawai, T. Real Space Observation of Double-Helix DNA Structure Using a Low Temperature Scanning Tunneling Microscopy. *Jpn. J. Appl. Phys.* **38**, L606–L607 (1999).
 188. Grill, L., Stass, I., Rieder, K.-H. & Moresco, F. Preparation of self-ordered molecular layers by pulse injection. *Surf. Sci.* **600**, L143–L147 (2006).
 189. Grill, L. Large molecules on surfaces: deposition and intramolecular STM manipulation by directional forces. *J. Phys. Condens. Matter* **22**, 084023 (2010).
 190. Guo, S. & Alex Kandel, S. Scanning tunneling microscopy studies of pulse deposition of dinuclear organometallic molecules on Au(111). *J. Chem. Phys.* **128**, 014702 (2008).
 191. Ghani, F., Kristen, J. & Riegler, H. Solubility Properties of Unsubstituted Metal Phthalocyanines in Different Types of Solvents. *J. Chem. Eng. Data* **57**, 439–449 (2012).

ACKNOWLEDGMENTS

Here, I would like to thank and acknowledge everyone who helped and supported me during my PhD studies. First, I want to thank my supervisor Thomas Jung for the ability to work in his group and for the support he gave me during this time. My involvement with investigation of molecules on surface started in 2012 when I did my internship under the supervision of Christian Wäckerlin, and I am very grateful to him for introducing me to the world of Surface Science. I am grateful to Nirmalya Ballav for deep and fruitful scientific discussions. I sincerely thank our outstanding technician Rolf Schelldorfer who was always very helpful in solving encountered problems.

A big part of the investigations reported in this thesis was acquired during beamtimes; this due to complexity of experiments, required involvement of several persons at the same time and coordination of preparation, transportation and measurements of the samples. I would like to sincerely thank all of them for help during this exhausting period. And not only for the help but also for their patience. In particular, I thank Olha Popova, Jan Nowakowski, Dorota Siewert, Harald Rossmann, Thomas Nijs, Jan Girovsky, Foteini Ravani, Fatemeh Mousavi, Mina Moradi, Elzbieta Gradauskaite, Mariah O'Doherty, Andrew Hunter, Iwasaki Masakazu and Joao Pedro Martins Godinho for their significant contributions. I would like to especially thank Jan Nowakowski for nights spent in the beamtimes together. At the same time, I would like to thank all beamline and SLS staff that was helping during this time: Jan Dreiser and Cinthia Piamonteze from the X-Treme beamline, Armin Kleibert from the SIM beamline, Matthias Muntwiler, Jun Zhang and De Lima Luis Henrique from the PEARL beamline, Ming Shi, Nicolas Plumb and Milan Radovic from the SIS beamline, Jörg Raabe and Simone Finizio from the PolLux beamline (special gratitude goes to them for also allowing me use their coffee machine, it had been very helpful during sleepless nights) and last Juraj Krempasky, Luka Debenjak and Alexandre Gobbo for debugging many hardware and software issues. Thank you for your support not only for the beamtimes but also for help during data analysis and interpreting the data.

A part of the STM experiments were performed at the Nanolab in Basel. I would like to thank Olha Popova again for the help and support during these measurements. Next, I would like to thank Vivian Müller from ETH Zurich for her help with the UV-VIS experiments.

I am also grateful to everyone at the Laboratory of Micro and Nanotechnology, as they were always ready to help. Special mention goes to the Edith Meisel who had to deal with all our administrative issues. The LMN meetings and SYN coffees were very interesting and good place for meeting people and discussing scientific cases and progress. Some of the suggestions obtained through these discussions are implemented in the thesis.

Our chemistry collaborators, Shi-Xia Liu and Silvio Decurtins are kindly acknowledged for providing various non-commercial spin-baring molecules that were used throughout this thesis. In addition, they have been very helpful in fruitful discussions and planning further steps in these investigations.

Last, I would like to thank my family and close friends that were always there to support me when I needed it. Their help was sometimes even more important than all of the scientific support one could get. You know who you are; special Thank you goes to you.

Thank you all again!

LIST OF PUBLICATIONS

1. **Two-dimensional calix[4]arene-based metal-organic coordination networks of tunable crystallinity**
Moradi M, Tulli L G., Nowakowski J, Baljovic M, Jung T A., Shahgaldian P
ANGEWANDTE CHEMIE INTERNATIONAL EDITION (online) DOI: 10.1002/anie.201703825
2. **Long-range ferrimagnetic order in a two-dimensional supramolecular Kondo lattice**
Girovsky J., Nowakowski J., Ali Md E., Baljovic M., Rossmann H. R., Nijs T., Aeby E. A., Nowakowska S., Siewert D., Srivastava G., Wäckerlin C., Dreiser J., Decurtins S., Liu S.-X., Oppeneer P. M., Jung T. A., Ballav N.
NATURE COMMUNICATIONS 8, 15388 (2017) DOI: [10.1038/ncomms15388](https://doi.org/10.1038/ncomms15388)
3. **Ink-Free Reversible Optical Writing in Monolayers by Polymerization of a Trifunctional Monomer: Toward Rewritable "Molecular Paper"**
Müller V., Hungerland T., Baljovic M., Jung T., Spencer N. D., Eghlidi H., Payamyar P., Schlüter A.D.
ADVANCED MATERIALS 1701220 (2017). DOI: [10.1002/adma.201701220](https://doi.org/10.1002/adma.201701220)
4. **Stabilization of alkali metal ions interaction with OH-functionalized graphene via clustering of OH groups - implications in charge storage applications**
Dobrota A. S., Gutic S., Kalijadis A., Baljovic M., Mentus S. V., Skorodumova N. V., Pasti I. A.
RSC ADVANCES 6, 57910 (2016). DOI: [10.1039/C6RA13509A](https://doi.org/10.1039/C6RA13509A)
5. **Surface Charge Storage Properties of Selected Graphene Samples in pH-neutral Aqueous Solutions of Alkali Metal Chlorides - Particularities and Universalities**
Gutic S, Dobrota A, Gavrilov N, Baljovic M., Pasti I, Mentus S,
INTERNATIONAL JOURNAL OF ELECTROCHEMICAL SCIENCE 11, 8662 (2016). DOI: [10.20964/2016.10.47](https://doi.org/10.20964/2016.10.47)
6. **Probing the Reactivity of Functionalized Surfaces by Porphyrin Metalation**
Nowakowski J., Nowakowska S., Srivastava G., Baljovic M., Girovsky J., Ballav N., Jung T. A.
CHEMISTRY SELECT 1, 891 (2016). DOI: [10.1002/slct.201600215](https://doi.org/10.1002/slct.201600215)
7. **Adsorption of nonmetallic elements on defect-free MgO(001) surface - DFT study**
Pasti I. A., Baljovic M., Skorodumova N. V.
SURFACE SCIENCE 632, 39 (2015). DOI: [10.1016/j.susc.2014.09.012](https://doi.org/10.1016/j.susc.2014.09.012)
8. **Bimetallic dimers adsorbed on a defect-free MgO(001) surface: bonding, structure and reactivity**
Pasti I. A, Baljovic M. R., Granda-Marulanda L. P, Skorodumova N. V
PHYSICAL CHEMISTRY CHEMICAL PHYSICS 17, 9666 (2015). DOI: [10.1039/c4cp05723f](https://doi.org/10.1039/c4cp05723f)
9. **Oxygen reduction reaction of Pt-In alloy: Combined theoretical and experimental investigations**
Pasti I. A, Gavrilov N. M, Baljovic M., Mitric M., Mentus S. V
ELECTROCHIMICA ACTA 114, 706 (2013). DOI: [10.1016/j.electacta.2013.10.114](https://doi.org/10.1016/j.electacta.2013.10.114)
10. **Magnetic exchange coupling of a synthetic Co(II)-complex to a ferromagnetic Ni substrate**
Waeckerlin C., Maldonado P., Arnold L., Shchyrba A., Girovsky J., Nowakowski J., Ali Md E., Haehlen T., Baljovic M., Siewert D., Kleibert A., Muellen K., Oppeneer P. M, Jung T. A, Ballav N.
CHEMICAL COMMUNICATIONS 49, 10736 (2013). DOI: [10.1039/c3cc45401k](https://doi.org/10.1039/c3cc45401k)

CURRICULUM VITAE

Milos Baljozovic

EDUCATION

Since Nov 2013 *Department of Physics, University of Basel, Basel, Switzerland*

Philosophy Doctor (PhD) candidate in Nanosciences

Title: Unraveling surface enabled phenomena in low-dimensional molecular systems

Supervisor: Prof. Dr Thomas A. Jung

Oct 2012 – Jul 2013 *University of Belgrade, Faculty of Physical Chemistry, Belgrade, Serbia*

Master of Science (M.Sc.) in Physical Chemistry

Title: Theoretical investigation of dimers M_1M_2 ($M_i = \text{Ru, Rh, Pd, Ir and Pt}$) interaction with MgO(001) surface

Supervisor: Prof. Dr Igor Pasti

Oct 2008 – Jul 2012 *University of Belgrade, Faculty of Physical Chemistry, Belgrade, Serbia*

Bachelor of Science (B.Sc.) in Physical Chemistry

Title: DFT study of stability, electronic structure and reactivity of Indium-modified Platinum surface

Supervisor: Prof. Dr Igor Pasti

RESEARCH EXPERIENCE

Since Nov 2013 *Molecular Nanoscience, Paul Scherrer Institute, Villigen, Switzerland*

PhD Student – Laboratory and Synchrotron based investigation of magnetic properties of various surface supported molecular systems under UHV conditions:

- Used state-of-the-art techniques for investigation of low-dimensional (magnetic) systems – UPS/XPS, LEED, STM/S, ARPES, XPD, XAS/XMCD
- Handled the measurements under extreme conditions – temperature down to 2K and magnetic field up to 7T
- Implemented technique for large molecule deposition in UHV directly from solution
- Independently run experiments at 4 Swiss Light Source synchrotron beamlines – SIM, SIS, PEARL and X-Treme
- Developed/Adapted detector for fast, time-resolved XAS at SIM beamline of the SLS
- Processed and analyzed large amount of data acquired during several Beamtime sessions at SLS
- Wrote and coauthored several beamtime and funding proposals
- Provided service XPS measurements for collaborators or users from NFFA.EU project

Apr 2013 – Oct 2013 University of Belgrade, Faculty of Physical Chemistry, Belgrade, Serbia

Teaching/Research Assistant – Performing individual research and helping supervisor with the experiments

- Used DFT for systematic investigation of metallic dimers interaction with MgO(001) surface
- Performed or helped in several experiments in electrochemistry (cyclic voltammetry, coulometry) and Molecular spectrochemistry (IR, UV-VIS, Raman spectroscopy)

Aug 2012 – Oct 2012 Molecular Nanoscience, Paul Scherrer Institute, Villigen, Switzerland

Intern – Summer internship in the field of surface science under supervision of Christian Wäckerlin:

- Learned about handling UHV systems, sample cleaning and molecular/metal deposition by CVD/PVD and E-Beam
- Developed novel surface superstructure with Nitrogen ad-layer for studying of molecular magnetism
- Helped with sample preparation during beamtime session

Jul 2011 – Oct 2011 University of Belgrade, Faculty of Physical Chemistry, Belgrade, Serbia

Intern – Summer internship in the field of electrochemistry under supervision of Igor Pasti:

- Learned basics of DFT calculations and data processing
- Performed DFT calculations to screen potentially interesting systems for experimental work
- Confirmed DFT results by performing several electrochemical experiments

Jul 2008 – Aug 2008 XLAB – Experimental Laboratory for Young People, Göttingen, Germany

Attendee – International summer camp with several topics covered, from genetics to forest ecology with combined theoretical and experimental work

Dec 2005 - Jul 2008 Department of Chemistry, Petnica Science Centre, Valjevo, Serbia

Attendee – Several theoretical and experimental sessions in the field of chemistry, with also supervised realization of independent projects – I had realized and presented 2 independent research projects on electrochemical reaction of hydrogen evolution

TEACHING EXPERIENCE

Since Nov 2013 Department of Physics, University of Basel, Basel, Switzerland

Teaching Assistant – Teaching duties at the UniBasel are complementary to research:

- Performed theoretical exercises/problem solving on different topics of Surface Science module
- Performed experimental exercises (Blockcourses) at Surface Science Laboratory at PSI
- Helped in preparing, performing and checking the Surface Science module exam

Apr 2013 – Oct 2013 University of Belgrade, Faculty of Physical Chemistry, Belgrade, Serbia

Teaching/Research Assistant - Teaching duties at the University of Belgrade are complementary to research:

- Performed theoretical and experimental work with students in electrochemistry and Molecular spectrochemistry modules
- Helped in organization/performance of seminars for high-school teachers

Apr 2006 - Jul 2012 Department of Chemistry, Petnica Science Centre, Valjevo, Serbia

Student Associate – Lecturing at several theoretical seminars and supervising individual projects in the field of chemistry

ADMINISTRATION AND MANAGEMENT EXPERIENCE

Since Aug 2015

Molecular Nanoscience, Paul Scherrer Institute, Villigen, Switzerland

Group webpage administrator – Administration of Molecular Nanoscience group webpage, updating the current/former members, research highlights, publications, research focus

Jan 2014 – Dec 2014

SPINMOL conference, Monte Verità, Ascona, Switzerland

Organizing Assistant – Coordination and management of all organizational issues including planning of the conference, setting up the program, accommodation for participants, budget, abstract booklet, payments from participants and refunds for invited speakers, gifts for all participants

Jan 2011 - Jul 2012

Center for Scientific Research of Students (CNIRS) of Faculty of Physical Chemistry

Co-Founder and President – One of the co-founders and first president of the Center for Scientific Research of Students with goal to involve students from earlier stages into research that is conducted at the Faculty of Physical Chemistry. During this period, several seminars about methodology of writing scientific papers, processing of experimental data, skills of paper presenting and more than 20 internships were organized/arranged.

PROFESSIONAL MEMBERSHIPS

- Member of Mensa (www.mensa.org, www.mensa.rs)
- Member of The International Association for the Exchange of Students for Technical Experience - IAESTE (<http://www.iaeste.ac.rs/site/>),
- Member of Serbian Chemical Society (<http://www.shd.org.rs/index.php>),
- Member of American Physical Society (<https://www.aps.org/>)

SKILLS

Research topics/techniques	Physical Chemistry, Surface Chemistry, Self-Assembled Monolayers (SAMs), Catalysis, Density Functional Theory (DFT) Calculations, Molecular Magnetism, Thin Film Magnetism, Laboratory and Synchrotron based X-ray Photoelectron Spectroscopy (XPS) and Analysis, X-Ray Absorption Spectroscopy (XAS), Near Edge X-ray Absorption Fine Structure (NEXAFS), X-ray Magnetic Circular Dichroism (XMCD), Angle Resolved Photoelectron Spectroscopy (ARPES), X-ray Photoelectron Diffraction (XPD), Scanning Tunnelling Microscopy/Spectroscopy (STM/S)
Languages	English (C1), German (B1), Italian (A2), Serbian (native)
Social skills	Pleasant, communicative, used to international environment and socially responsible person
Computational skills	General knowledge in MS Windows, Linux and Apple iOS environment and internet, advanced knowledge in MS Office, Python, Delphi, Origin, IgorPro, MatLab, Mathematica and QuantumEspresso
Proposal writing skills	Main proposer in 7 and co-proposer in another 6 beamtime proposals. Helped in writing of several funding proposals as well

AWARD AND HONORS

2011 - 2017	Stipend from the “Dositeja” Fund for young talents of Republic of Serbia
2013 - 2017	Annual award from the Municipality of Leskovac Fund for young talents
2014	“Pavle Savic” award of the Serbian Physico-chemical Society for the best students from the Faculty of Physical Chemistry
2013	Best student of the generation award for the bachelor studies
2013	“Sisters Bulajic” Foundation award for the best B.Sc. thesis at the Faculty of Physical Chemistry
2013	Serbian Chemical Society annual award for best bachelor student at the Faculty of Physical Chemistry
2013	Hemofarm Foundation award for excellent students at the University of Belgrade
2011 - 2013	Studenica Endowment stipend for extraordinary students at the University of Belgrade
2008	October award of the Municipality of Leskovac for scientific and social achievements

DISSEMINATION

PRESENTATIONS

13 oral and 8 poster presentations at international conferences (complete list as appendix), together with two Scientific Seminars held at *National Institute of Standards and Technology* (organized by NIST Fellow Joseph Strosio) and *Stanford University* (organized by prof. Tony F. Heinz)

PUBLICATION RECORD

10 accepted and 1 article under revision in international peer-reviewed journals among which one publication in *Nature Communications* (2017), *Advanced Materials* (2017) and *Chemical Communications* (2013).

SELECTED PUBLICATIONS (complete list as an appendix):

Long-range ferrimagnetic order in a two-dimensional supramolecular Kondo lattice

Girovsky J., Nowakowski J., Ali Md E., Baljozovic M., Rossmann H. R., Nijs T., Aeby E. A., Nowakowska S., Siewert D., Srivastava G., Wäckerlin C., Dreiser J., Decurtins S., Liu S.-X., Oppeneer P. M., Jung T. A., Ballav N.

NATURE COMMUNICATIONS 8, 15388 (2017) DOI: [10.1038/ncomms15388](https://doi.org/10.1038/ncomms15388)

Ink-Free Reversible Optical Writing in Monolayers by Polymerization of a Trifunctional Monomer: Toward Rewritable “Molecular Paper”

Müller V., Hungerland T., Baljozovic M., Jung T., Spencer N. D., Eghlidi H., Payamyar P., Schlüter A.D.

ADVANCED MATERIALS 1701220 (2017). DOI: [10.1002/adma.201701220](https://doi.org/10.1002/adma.201701220)

Bimetallic dimers adsorbed on a defect-free MgO(001) surface: bonding, structure and reactivity

Pasti I. A., Baljozovic M. R., Granda-Marulanda L. P., Skorodumova N. V

PHYSICAL CHEMISTRY CHEMICAL PHYSICS 17, 9666 (2015). DOI: [10.1039/c4cp05723f](https://doi.org/10.1039/c4cp05723f)

Magnetic exchange coupling of a synthetic Co(II)-complex to a ferromagnetic Ni substrate

Waeckerlin C., Maldonado P., Arnold L., Shchyrba A., Girovsky J., Nowakowski J., Ali Md E.,

Haehlen T., Baljozovic M., Siewert D., Kleibert A., Muellen K., Oppeneer P. M, Jung T. A, Ballav N.

CHEMICAL COMMUNICATIONS 49, 10736 (2013). DOI: [10.1039/c3cc45401k](https://doi.org/10.1039/c3cc45401k)